Analysis of mechanically induced noise on flexible pipe connectors for parabolic trough solar collectors

Master's Thesis

Maxim Klenin
2193203

Tongji University

Reviewer: Prof. Dr. WEIMIN Zhang
Supervisors: Dr. GARCÍA Alejandro
                Dipl. Ing. SALIOU Guillaume

09.11.2022

Declaration of Academic Honesty

I hereby declare to have written the present master's thesis on my own, having used no other resources and tools than the listed. All contents cited from published or nonpublished documents are indicated as such.

Place, Date

Abstract

Concentrating Solar Power (CSP) technologies are a promising alternative to fossil fuel, in which direct solar radiation is focused via mirrors on a receiver to heat up a Heat Transfer Fluid (HTF) that is used to generate electrical or thermal energy. Parabolic Trough Collectors (PTC) are a type of these technologies and incorporate Rotation and Expansion Performing Assemblies (REPAs), which connect the rotating receiver tubes with the piping of the power plant. REPAs are among the most stressed and critical components of PTCs, as they have to withstand around 10,000 sun tracking cycles during their lifetime, which is equivalent to 30 years of operation. All tests were done on the REPA test facility at Plataforma Solar de Almería (PSA), erected in a collaboration between the German Aerospace Center (DLR) and the Spanish Center for Energy, Environmental and Technological Research (CIEMAT).

For PTC power plants, a reactive maintenance strategy is applied and the REPAs are replaced after a malfunction is detected. This thesis focuses on a different strategy, consisting in the condition monitoring of the swivel joint as part of flexible pipe connectors, which are a type of REPA. In condition monitoring based maintenance parameters of a component are continuously measured to determine its state, so that the component can be exchanged before a failure occurs. However, condition monitoring presents a challenge because the swivel joints do not show explicit wear signs. Vibration measurements, which are widely used in the industry for being reliable, affordable and non-intrusive, are deployed for promising results in terms of REPA monitoring.

Cycles with different HTF pressures are performed to study the effect of pressure on the vibration behavior of the swivel joint. Short Time Fourier Transform (STFT), one of the most popular frequency analysis methods in signal processing, is used to generate spectrograms to investigate the frequencies included in the vibration signal. Clear differences are seen in the vibration behavior at different HTF pressures.

An accelerated aging test of 10,000 cycles is performed simultaneously on two REPAs at the REPA test rig. REPAs' swivel joints' vibrations are recorded, compared and analyzed using spectrograms. A machine learning model, including principal component analysis (PCA) and support vector machine (SVM), is proposed to classify the vibration at different stages of the aging process. The proposed machine learning model achieves high classification accuracy when applied to the measured data.

The results show that vibration is a suitable parameter to determine the swivel joint's status.

Contents

List of Figures

List of Tables

List of Abbreviations

ANN	Artifical Neural Network
BJA	Ball Joint Assembly
CIEMAT	Center for Energy, Environmental and Technological Research
CNN	Convolutional Neural Network
CPV	Cumulative Percent Variance
CSP	Concentrating Solar Power
DAQ	Data Acquisition
DFT	Discrete Fourier Transform
DLR	German Aerospace Center
DNI	Direct Normal Irradiation
FFT	Fast Fourier Transform
GUI	Graphical User Interface
HTF	Heat Transfer Fluid
IEPE	Integrated Electronics Piezo-Electric
KU	Kinematics Unit
LDA	Linear Discriminant Analysis
MEMS	Micro Electro Mechanical System
OPC	Open Platform Communications
PC	Principal Component
PCA	Principal Component Analysis
PLC	Programmable Logic Controller
PSA	Plataforma Solar de Almería
PSD	Power Spectral Density
PTC	Parabolic Trough Collector
REPA	Rotation and Expansion Performing Assembly
RFHA	Rotary Flex Hose Asssembly
RMS	Root Mean Square
SCADA	Supervisory Control and Data Acquisition
STFT	Short Time Fourier Transform
SVM	Support Vector Machine

1. Introduction and Motivation

Energy consumption is increasing at a fast rate in our present-day society. This is due to a lot of factors such as industrialization, higher living standard and a growing population. Nowadays, and despite world awareness and climate change policies, fossil fuels still remain the main energy source around the world. As a result, the amount of CO_2 and other greenhouse gases emitted into the atmosphere keeps increasing. [8] Besides greenhouse gases, there are also other pollutants that have a negative impact on the environment and human health. In fact, air pollution is the cause of many diseases that greatly affect the respiratory system and other systems of the body. [39]

To tackle these issues, it is important to further improve and use more renewable energy technologies. One of them is Concentrating Solar Power (CSP), in which the direct solar radiation is used to heat up a Heat Transfer Fluid (HTF). The heat is used for thermal energy that can be used afterwards, e.g. to supply industrial processing heat, and to generate electricity in conventional power plants. This technology presents the advantage of energy storage and 24h electrical production. The most widely deployed CSP technology is the Parabolic Trough Collector (PTC). [39]

This thesis focuses on the condition monitoring of a highly stressed key component for PTC power plants, which is called Rotation and Expansion Performing Assembly (REPA). Affordable technologies are available for condition monitoring and predictive maintenance. In contrast with the traditional preventive and reactive maintenance strategies, sensors are implemented to find out if parts are about to fail for example. To characterize a part, many parameters can be measured, such as temperature, humidity, vibration, image, noise, etc. [12]

A test rig for REPAs was built at the Plataforma Solar de Almería (PSA). It is owned by the Spanish Center for Energy, Environmental and Technological Research (CIEMAT), which is located in the Tabernas Desert in South Eastern Spain. The test rig is a joint collaboration between the German Aerospace Center (DLR) and CIEMAT, and it is used for accelerated aging of REPAs as well as testing REPAs' behavior under different operation conditions, e.g. different temperatures and pressures. [32] The REPAs are monitored with a variety of sensors such as force, torque, pressure, temperature and vibration.

The objective of the thesis is to set up a monitoring system to measure the vibrations produced by the REPA's swivel joint. The recorded signals are then analyzed and interpreted to obtain a correlation between the available data and the state of the swivel joint. A machine learning model is built that tries to define the condition of the swivel joint.

2. State of the Art

In this chapter, a general overview of different CSP technologies is given. The PTC technology is looked at in detail, since it is the one that contains the REPA. Finally, different maintenance strategies are explained and also vibration analysis for fault and wear detection is addressed.

2.1. Concentrating Solar Power

The sun is the biggest source of energy, taking into account that all forms of available energy directly or indirectly derive from it. One way of producing electricity is converting the solar energy into heat and then using that heat in conventional power plants (e.g. Rankin cycle), which is feasible using CSP technologies. [39] However, only direct normal irradiation (DNI) can be used for this purpose. DNI is the irradiance that arrives directly from the sun without being diffused. [23] In figure 2.1 the average worldwide DNI is shown. Locations with higher DNI are more suitable for CSP power plants.
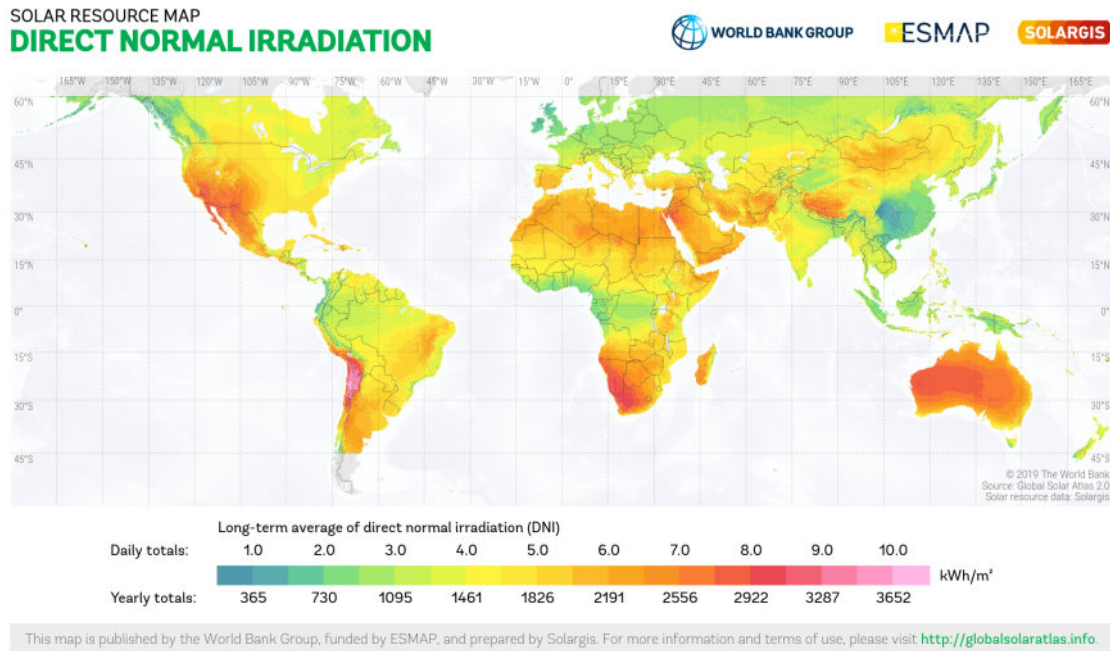
Figure 2.1.: Long-term average of DNI worldwide [40]

In general terms, a CSP technology system basically comprises a concentrator and a receiver. The concentrator focuses the direct solar radiation on the receiver. For this, optical systems (reflectors) are used and the sun is tracked, so that the concentrator can be placed accordingly. The receiver absorbs the direct solar radiation, resulting in high temperatures and thus an increase in thermal energy. This thermal energy is delivered to a heat transfer fluid (HTF), which can further be used for electricity generation or simply for the storage of thermal energy. CSP technologies can be divided into two groups: point-focusing and line-focusing systems. Point-focusing systems include Central Tower Receivers, also

known as Solar Towers, and Solar Dishes. Line-focusing include Linear Fresnel Collectors and Parabolic Trough Collectors. [39] The latter is explained in detail in the next subsection. 2.2

2.2. Parabolic Trough Collector (PTC)

PTC systems are the most deployed and mature CSP technology. PTCs consist of parabolic-shaped concentrators containing reflectors made of silvered-glass mirrors or aluminum. A schematic of PTCs is shown in figure 2.2. Single-axis tracking is used to follow the sun throughout the day. The collectors can be oriented in a north-south direction or an east-west direction. Overall, north-south oriented collectors dispatch slightly more energy throughout the year, whereas east-west oriented PTCs collect more energy during the winter, hence the orientation depends on the application. [28]
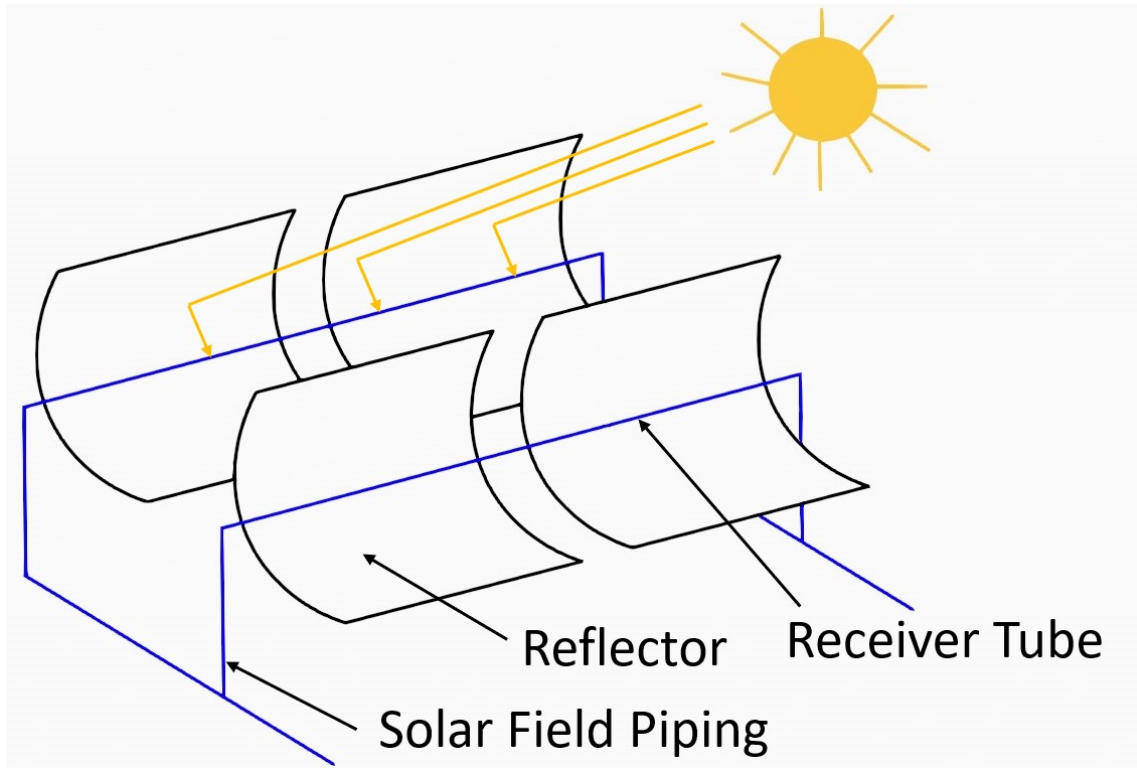
Figure 2.2.: Schematic of a Parabolic Trough Collector (PTC) [39]

The receiver is a tube located in the focal axis of the concentrators parabola that absorbs the reflected direct solar radiation. The receiver is encapsulated in an evacuated glass cover to reduce heat losses. Furthermore, the glass envelope features non-reflective coating to reduce reflection of the radiation and to realize a very high transmissivity. Both the receiver tube and the glass cover are connected by metallic bellows to achieve the vacuum-tight enclosure and to compensate for the thermal expansion differences of both components. A schematic of such a receiver tube can be seen in figure 2.3. [39]

The concentrated radiation is thereby absorbed by the Heat Transfer Fluid (HTF) that is being pumped through the receiver tube. An HTF is typically a synthetic oil, but molten
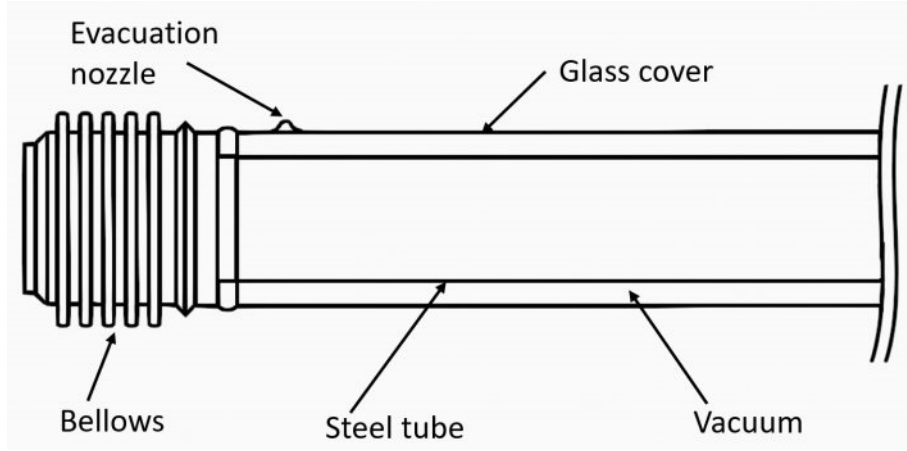
Figure 2.3.: Schematic of a receiver tube of a Parabolic Trough Collector (PTC) [33]

salts or steam can also be used. The maximum temperature that can be achieved during operation depends on the HTF. For synthetic oil it goes up to 400 °C, while for molten salts it can go up to 540 °C. [28] Finally, the acquired heat can be used in conventional power plants to generate electricity e.g. Rankine, Brayton, or combined cycle. [39]

2.3. Rotation and Expansion Performing Assemblies (REPAs)

During a sunny day, the collectors of PTC plants rotate from where the sun rises (ϕ_{start}) to where it sets (ϕ_{stop}), tracking the sun according to the one-axis tracking system. At the end of the day they move back to the stow position (ϕ_{stow}), which is the position in which the PTC is situated when the collector is not operating, e.g. during the night, a cloudy day or maintenance campaign. The tracking system uses either algorithms to approximate the solar position or measurement technologies to set an angle value of the collector. If the current collector angle differs from the set value, the position of the PTC is adjusted. This procedure happens every 20-40 seconds, meaning that the PTC does not perform a continuous rotation. [32] The rotation movement is visualized in figure 2.4.

Rotation and **E**xpansion **P**erforming **A**ssemblies (REPA) are the part of a PTC plant that ensure the transition between the static rotation axis and the moving focal line of the collectors. At both ends of the PTC, a fixed pipe is connected to the receiver tube by a REPA to enable the rotation of the receiver tube. In addition, as the receiver tube is heated or cooled, its length changes due to thermal expansion or contraction, respectively. [38] REPAs are among the most stressed components that are prone to failure. They have to withstand temperatures up to 393 °C, pressures up to 35 bar and torques and forces that come from both the rotation and thermal expansion/contraction. [32] The average service lifetime of a PTC plant is 25-30 years [4] in which the REPAs perform around 10,000 sun tracking cycles.

There are two types of REPA: Ball Joint Assemblies (BJA) and Rotary Flex Hose Asssemblies (RFHA).
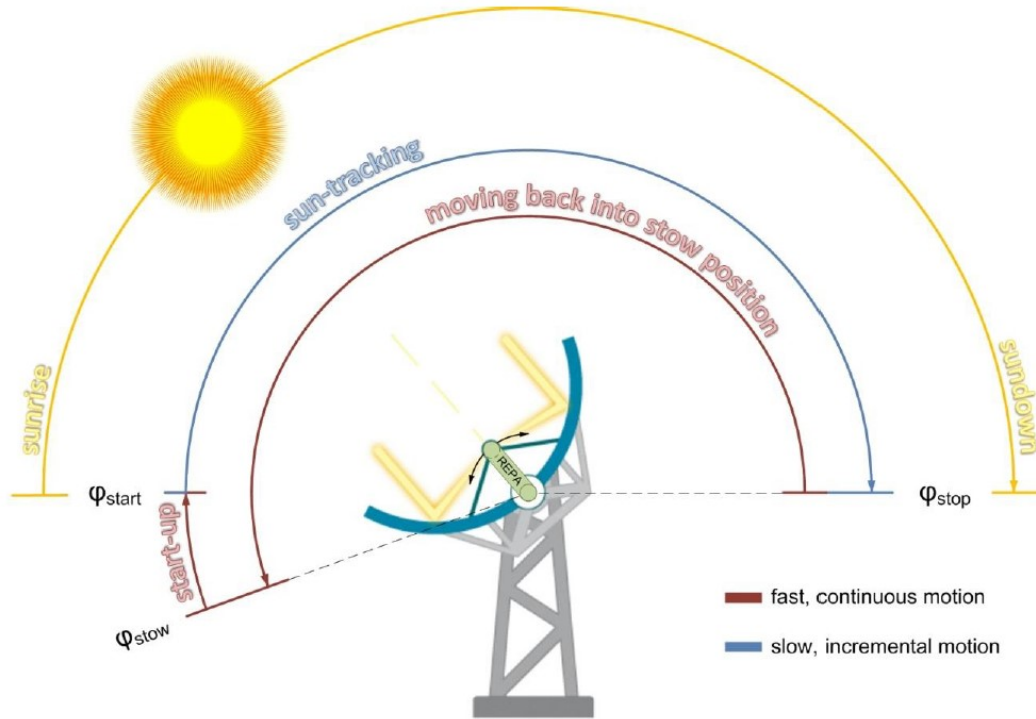
Figure 2.4.: Typical rotation cycle of a PTC during a day [37]

As seen in figure 2.5, the BJA consists of three ball joints that are connected by tubes, thereby compensating for the rotational and translational movements. Reinforced graphite is used as a sealant in the ball joints to reduce friction and prevent leakage. Since the reinforced graphite may wear off, it needs to be refilled regularly. This can be done under PTC operation because it does not normally require a shutdown. [32]

On the other hand, RFHAs consist of a corrugated metal hose, a swivel joint and an interface for transmitting torque from the collector, which is often called *torque sword*, given that it is usually a flat steel beam. The part of the swivel joint that is connected to the fixed pipe stays stationary during operation, while the other part that is connected to the corrugated metal hose is moved by the torque sword, which in turn is driven by the drive unit of the PTC. Consequently, the swivel joint compensates for the rotational movement, while the hose compensates for the translational movement. [37] A RFHA can be seen in figure 2.6.

As mentioned above, failures of the REPA lead to HTF leakages which, in addition to environmental hazard, can provoke a shut down and part replacement, thus increasing the operation and maintenance costs. [5]

2.4. Maintenance strategies

There exist four main maintenance strategies, listed as follows from the easiest to the most complex to be implemented. When correctly applied, the downtime and spare part management can be drastically improved [10]:
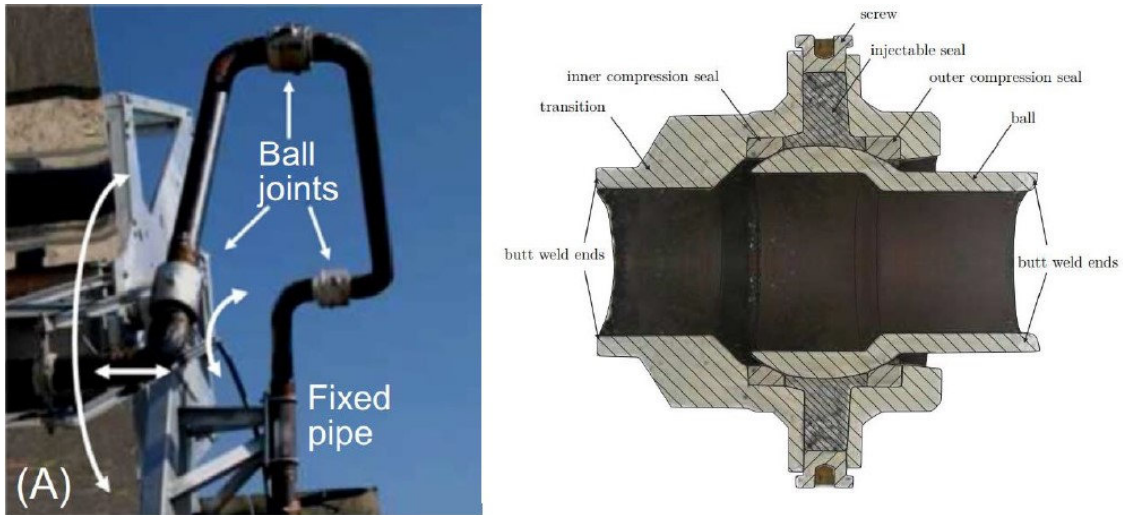
Figure 2.5.: Uninsulated ball joint assembly (left) and schematic of a ball joint [37]
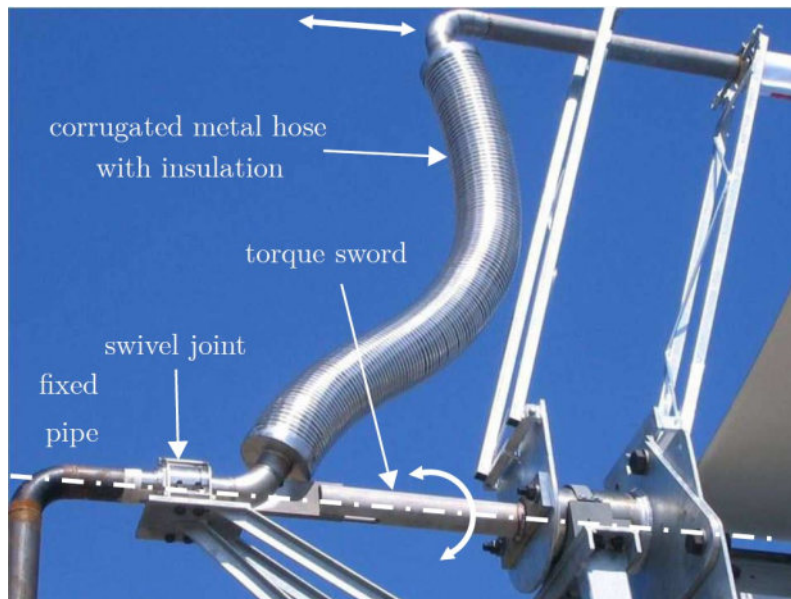
Figure 2.6.: Rotary flex hose assembly (RFHA) [32]

- Reactive Maintenance

- Preventive Maintenance

- Condition-based Maintenance

- Predictive Maintenance

When reactive maintenance is implemented, maintenance work (e.g. a part is replaced) is only done when a malfunction occurs. Here the wear reserve is used to its full extent, however this leads to significant time losses and thus the cost also rises. A reactive maintenance strategy should only be used in specific situations, for example if a part can quickly and easily be changed because there are plenty of parts for replacement or it is not technically feasible to implement the other strategies. [10]

The other three strategies are proactive, which implies that maintenance work is done before a failure occurs. This can be advantageous if the replacements are planned, so that all the needed resources can be prepared before the replacement, which leads to shorter downtimes and anticipation of unplanned events. [10]

When preventive maintenance is implemented, maintenance work is done at set intervals. For instance, maintenance work can be done after a certain time period or after a certain number of products was manufactured. The downside to this strategy (and proactive maintenance in general) is that parts are not used to their full potential and may be replaced even if they still could be used. Therefore, more parts are needed, which means that the costs also rise. [10]

Condition-based maintenance addresses this issue. In this strategy, the state of a part is considered using condition monitoring. Sensors are implemented to monitor some parameters, such as temperature, humidity, vibration, image, noise, etc. [12] However, surveying a part and measuring all the needed parameters can also lead to costs. Condition-based maintenance should only be done if measuring and collecting the necessary data is affordable and technically feasible. [10]

If the system is too complex predictive maintenance is used. This strategy implements either statistical analysis methods or simulation methods. Statistical analysis methods are used to recognize specific patterns in the measured parameters to predict an error or a failure before it actually occurs [49], whereas simulation methods are used to compare the measured parameters with simulated results to achieve the same goal. [2]

2.5. Vibration analysis for fault and wear detection

Vibration analysis is a common strategy for predictive maintenance in different fields and systems. These systems can include shafts, gears, bearings, electrical machines such as motors and generators or bladed machines, e.g. rotating fans, HTF pumps, compressors and turbines. [34] Vibration analysis is also used in systems without rotating parts, including railway point devices [24] and curved beams in planes [30]. Simple statistical features

(e.g. root mean square (RMS)), frequency analysis and machine learning models can be used in vibration analysis to detect possible faults, wear and anomalies. [43]

Among all the existing frequency analysis methods in vibration analysis, the most used ones are the Fourier Transfrom (FT), Short Time Fourier Transform (STFT) [24][50], Wavelet Transform [1] [29] [44] and Hilbert-Huang-Transform (HHT) [13], the latter combining the Empirical Mode Decomposition [51] and Hilbert Transform [47]. [43] These methods represent the frequencies and their amplitudes in the processed signal. In recent years, higher order statistical methods are being developed for vibration analysis, such as the bi-spectrum analysis, which shows how the frequencies in the processed signal are coupled. [48] FT and STFT are explained in detail in section 4.1.

In a subsequent step of the vibration analysis, features that are extracted from the measured vibrations are used to make statements about the condition of the system studied. These features can be calculated using statistics or frequency analysis. To that end, simple rules can be applied, e.g. if a calculated value is above or under a certain threshold the system is considered defect, at risk, should be repaired or replaced [50]. Nevertheless, more complex methods can be used for this purpose, such as machine learning methods. These include principal component analysis (PCA) [24], support vector machines (SVM) [21][44], artifical neural networks (ANN) [21][44], deep neural networks (DNN) and convolutional neural networks (CNN). [43] PCA and SVM are explained in more detail in sections 4.2 and 4.3.2, since they have been implemented in this work.

3. Experimental Setup

3.1. REPA Test Rig

The REPA test rig has been designed for temperatures up to 450 °C and pressures up to 40 bar. For a representative operational reason, the tests carried out in this thesis were done with the HTF Therminol®VP-1, at 393 °C and 35 bar.
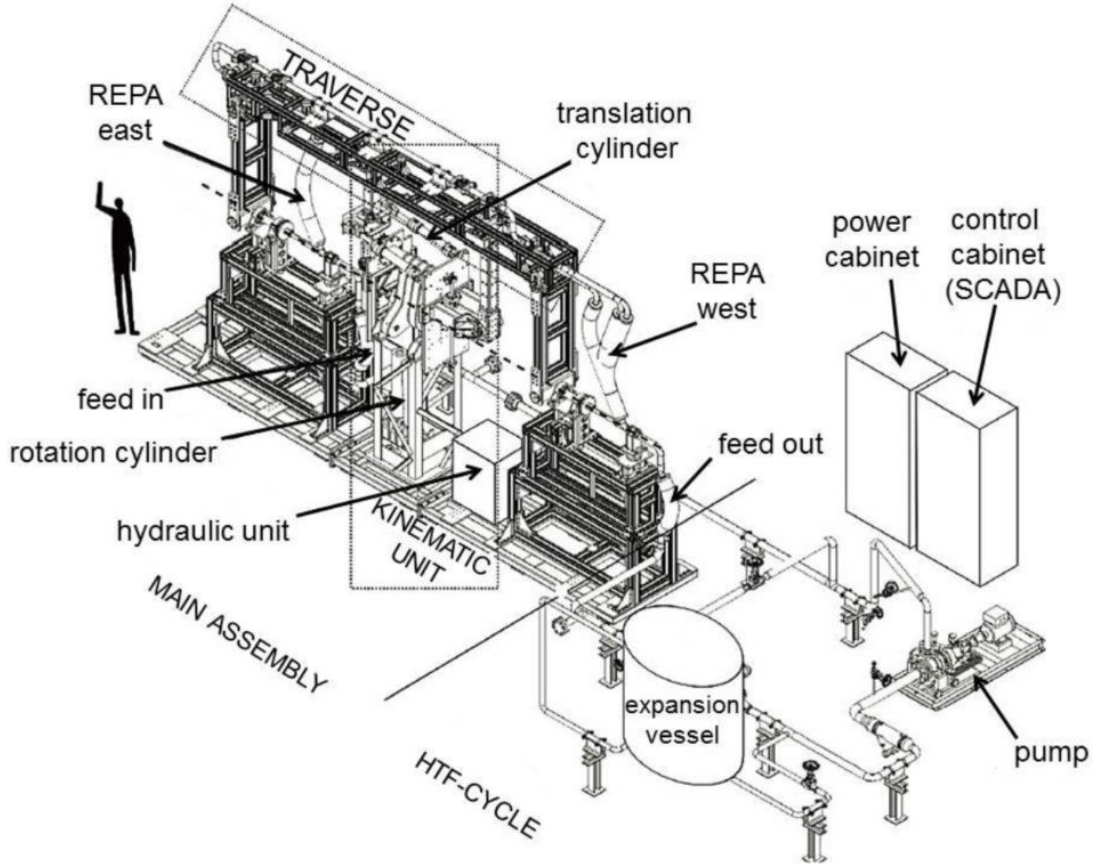
Figure 3.1.: Isometric view of the REPA test rig at PSA [37]

A view of the test rig can be seen in figure 3.1. It can be divided into the HTF cycle and the main assembly. The HTF cycle includes a magnetic coupled pump that can reach flows up to 40 m^3/h and nine electric band heaters of 3500 W of power each. An expansion vessel absorbs the HTF's thermal expansion and is filled with nitrogen to reach the desired pressure. [37]

The main assembly, shown in figure 3.2, consists of a traverse with the HTF piping and a kinematics unit (KU) . While the HTF flows through the assembly the KU moves the traverse and the two flexible hoses of the REPAs. The rotation of the traverse is done by two hydraulic cylinders that are positioned in the drive pylon. The traverse is connected to the KU via two steel arms. Between the two steel arms are two other hydraulic cylinders that perform translation movement of the traverse to simulate the collectors receivers
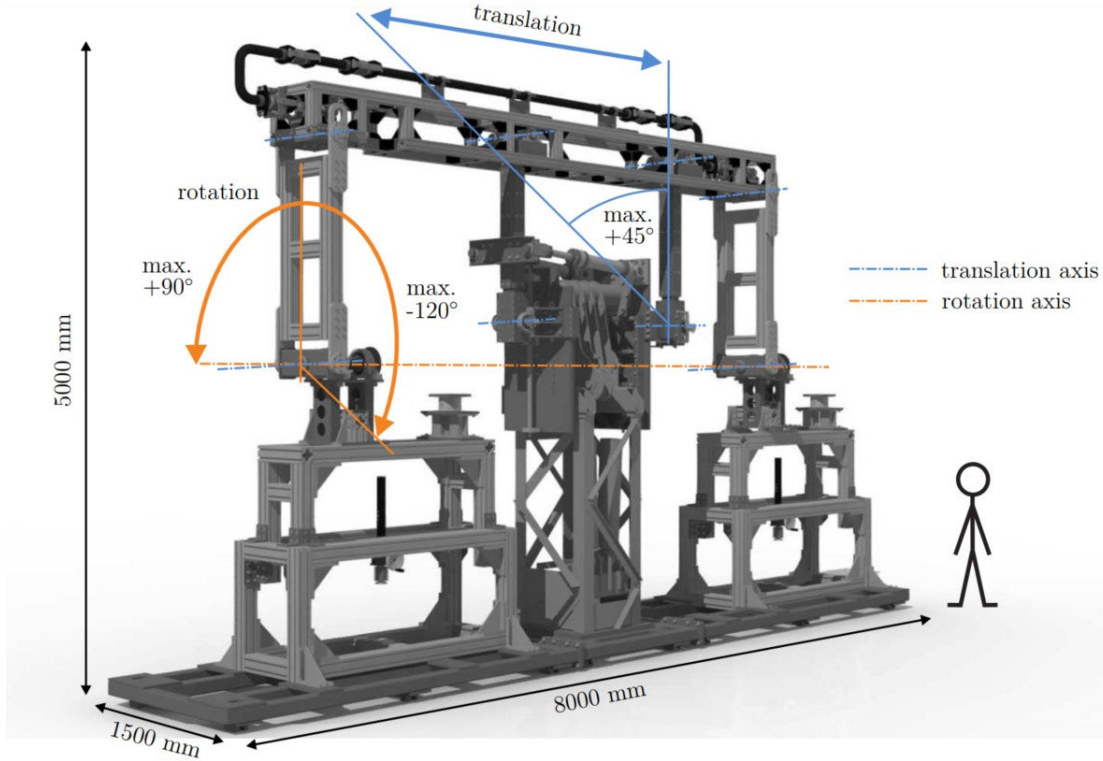
Figure 3.2.: CAD model of the Kinematics Unit (no REPAs included; configuration for testing RFHA) [32]

thermal expansion on the REPAs. The distance between the traverse and the KU's axis of rotation is equivalent to the distance between the receiver and the axis of rotation at a PTC's collector. This distance can change from a collector design to another, for that reason the arm length can be modified from 1.5 to 2.3 m. [37]

The KU and the HTF unit of the test rig are controlled using a Supervisory Control and Data Acquisition (SCADA) system. An overview can be seen in figure 3.4. It includes a SIMATIC S7-300, which is a Programmable Logic Controller (PLC) that controls the HTF pump speed, heat band resistances, gathers measurement data, sends orders and inputs to the servo controller, which controls the speed of the motors of the hydraulic system. An Open Platform Communications server (OPC server) is used to read and write the variables in the PLC. The OPC server is connected to a graphical user interface (GUI) that is programmed in LabVIEW and is used to operate the REPA test rig. [11]

A servo drive system actuates the rotation and an inverter drive system actuates the translation as can be seen in figure 3.5. 4/3 directional control valves regulate if a cylinder piston is pushing or pulling. This way the direction of the traverse movement can be set. In table 3.1 the cylinder configuration for the cylinder pistons that rotate the traverse is shown during a cycle. [37] During cylinder piston switch points at around 35° and 133°, when a cylinder piston changes from pushing to pulling or vice versa, the movement of the traverse slows down.

Figure 3.3.: REPA test rig at PSA
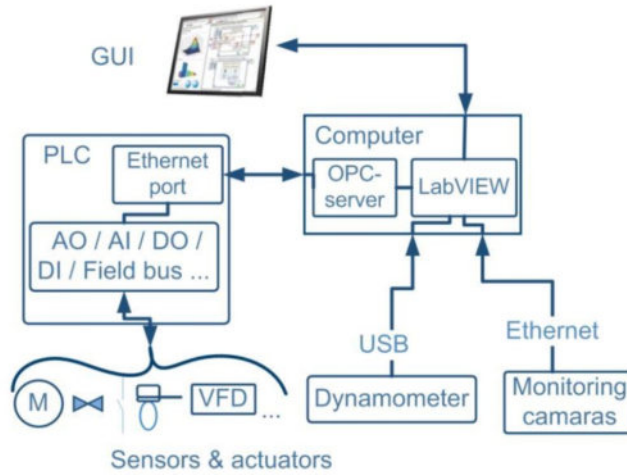
Figure 3.4.: Overview of the SCADA system [11]

Table 3.1.: Cylinder piston configuration for movement from the starting position to the end position and from the end position to the starting position

Rotation section	West cylinder	East cylinder
starting position (e.g -20°) to 35°	pull/push	pull/push
35° to 133°	pull/push	push/pull
133° to end position (e.g 180°)	push/pull	push/pull

11
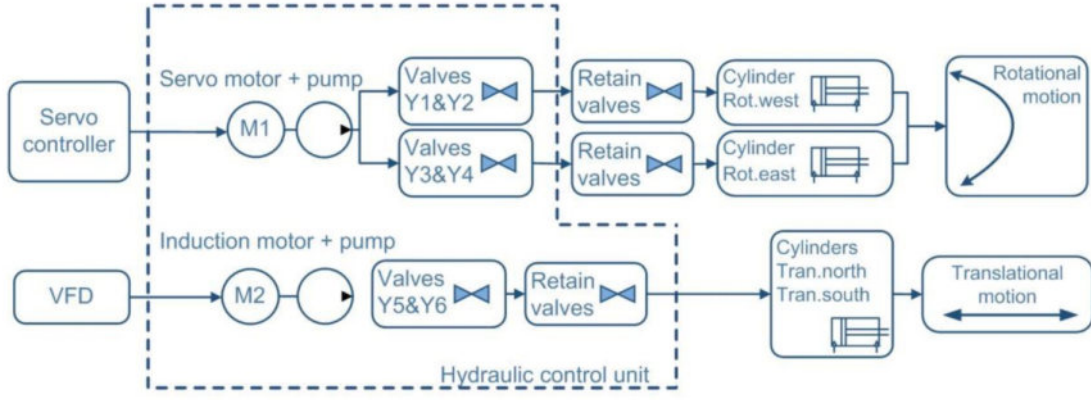
Figure 3.5.: Overview of the hydraulic control unit [11]

3.2. Vibration sensors

Piezoelectric accelerometers with a voltage output, also called IEPE Sensors (Integrated Electronics Piezo-Electric Sensors), are used to measure the vibrations. There are other types of accelerometers, such as piezoelectric ones with a charge output (also known as "charge mode accelerometers"), and micro electro mechanical system accelerometers (MEMS accelerometers). Using the IEPE sensors leads to lower costs but they can not be used for monitoring vibrations of low frequencies. Another restriction is that they have a temperature limit of 163 °C. Conversely, charge mode sensors have a higher temperature range in which they can be used, whereas MEMS accelerometers can measure acceleration at low frequencies and have a lower temperature limit. [19]

3.2.1. Piezoelectric accelerometers

In this type of accelerometers, the acceleration is measured using the piezoelectric effect. When a force is vertically applied to the surface of a piezoelectric material, a charge displacement happens inside, which can be measured as a voltage. This voltage is proportional to the applied force. As seen in figure 3.6, an accelerometer includes a seismic mass that is connected to a piezoceramic disc. When the seismic mass is accelerated by vibrations, it exerts a force upon the piezoceramic disc due to inertia. Given that the seismic mass has a known fixed value, the acceleration can be simply calculated according to Newton's law (Eq. 3.1), and thus the voltage is also proportional to the acceleration. [46]

$$F = ma \tag{3.1}$$

The proportionality factor between the voltage and the acceleration is called voltage sensitivity.

$$Bua = \frac{u}{a} \tag{3.2}$$
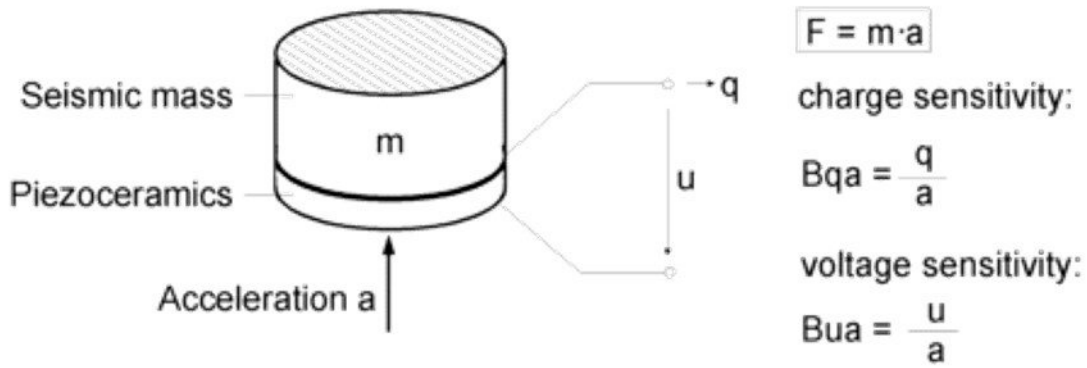
Figure 3.6.: Basic operating principle of a piezoelectric accelerometer [46]

The most important parameters that need to be considered when choosing piezoelectric sensors are introduced below. These parameters include the frequency response, the measurement range, the temperature range and the temperature influence on the measurement precision.

Frequency Response

The whole sensor, including the piezoceramic disc, seismic mass and other flexible parts, builds a spring-mass-system that has a resonant frequency. Because of that, there is a limit to the highest frequency that the measured vibration can have. There is also a limit to the lowest measurable frequency, depending on the electronics that are used to process the signal from the sensor. [46]

Figure 3.7 shows a typical frequency response of piezoelectric accelerometers, although it may vary depending on the specific accelerometer. The measured deviation can be read from the frequency response. For example, in figure 3.7 at around 1/5 of the resonance frequency, the measured deviation is at 5%. [46] In the data sheets of piezoelectric accelerometers, the frequency range, in which the measured deviation is under 5%, is often given.

Transverse Sensitivity

An accelerometer is only supposed to react to accelerations in one direction. However, they have a sensitivity to acceleration in other directions. This means that an accelerometer will have a voltage output even if acceleration is only applied perpendicular to the main axis. The transverse sensitivity is the ratio of the sensitivity in the perpendicular direction of the main axis and the sensitivity in the direction of the main axis. [46]

Measurement Range

Accelerometers can only be used in a certain measurement range. As a result, maximum acceleration in both positive and negative directions are normally given. A short exposure
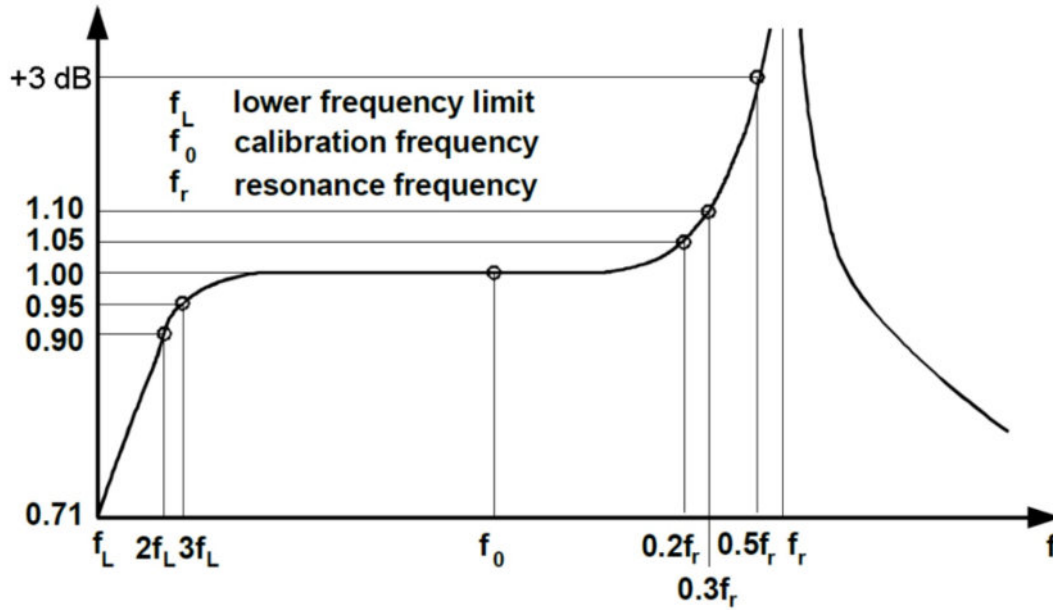
Figure 3.7.: Typical frequency response of a piezoelectric accelerometer [46]

to an acceleration outside of the measurement range will not break the sensors. Often a destruction limit is also given at which the sensor will break irreversibly. [46]

Temperature Influence

Accelerometers can only be used within a certain temperature range. IEPE Sensors can be used up to 163 °C, while there are some charge mode sensors that can even be used up to 649 °C. The reason for this is that IEPE Sensors include electronics that are prone to break at higher temperatures, while the charge mode sensors are connected to these electronics with a cable, so that they avoid being at the measured spot. The temperature also influences the measurement. Figure 3.8 shows an example of measurement deviation depending on the temperature. The precision sensitivity to temperature is also dependent on the sensor type.

Given the importance of the temperature influence on accelerometers, a temperature verification test was done at another facility of the PSA called PROMETEO owned by CIEMAT. The aim was to check the real temperatures that can be obtained at the locations where the sensors will be installed, and also corroborate if IEPE sensors can be used for the purpose of predictive maintenance using vibration analysis at PTC facilities. To that end, three type K thermocouples were used as shown in figures 3.9 and 3.10. The locations were selected as far away from the swivel joint as possible, in order to reduce exposure to high temperatures. The thermocouples were connected to an ALMEMO® 2890-9 data logger shown in figure 3.11. The table 3.2 shows the results of the temperature verification test, as well as other parameters that may affect the temperature, such as HTF temperature, air temperature and wind velocity. The highest temperature measured was 101.8 °C, which is significantly lower than the maximum temperature of 163°C that IEPE
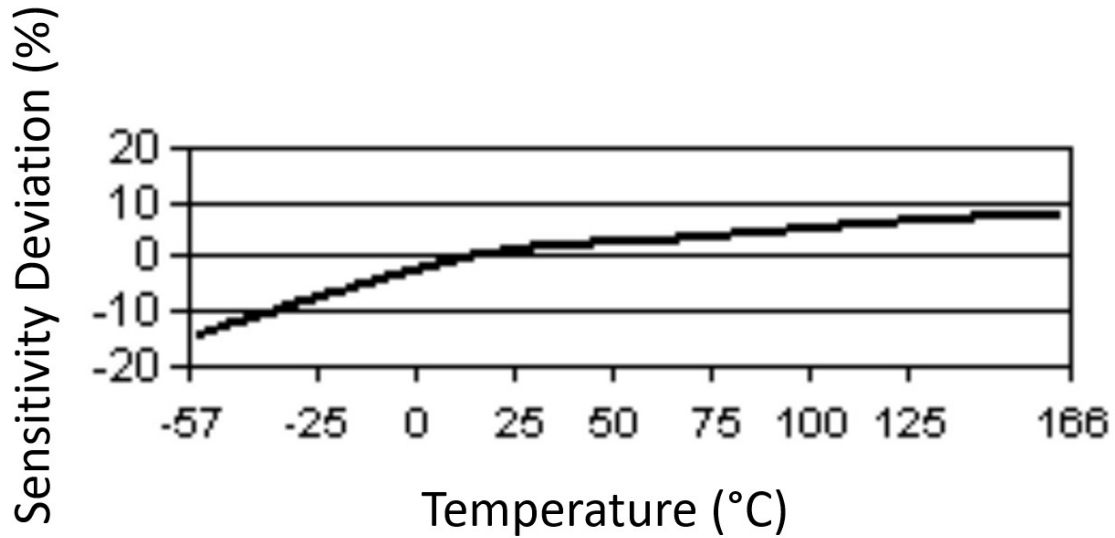
Figure 3.8.: Example of sensitivity deviation over temperature of an IEPE sensor [14]

sensors can withstand. This means that IEPE sensors can be viable sensors for measuring vibrations of the swivel joint at other PTC facilities for predictive maintenance purposes.

Figure 3.9.: Location of the type K thermocouples on the swivel joint at the PROMETEO facility owned by CIEMAT

3.3. Experimental Setup

For the vibration measurements at the REPA testrig, two types of IEPE sensors were used, namely KS95B.100 from IDS Innomic Schwingungsmesstechnik GmbH and 320C52 from PCB Synotech GmbH. The setups for both sensor types are presented in the following subsections.

3.3.1. Setup with the sensors KS95B.100

The initial setup included three sensors of the type KS95B.100. One major disadvantage of this type of sensors is a high sensitivity deviation at temperatures over 80°C, which

Figure 3.10.: Closeup of the type K thermocouples on the swivel joint at the PROMETEO facility owned by CIEMAT

Figure 3.11.: ALMEMO® 2890-9 data logger

Table 3.2.: Results of the temperature measurements of the swivel joint at PROMETEO owned by CIEMAT

Day	Time	T(HTF) [°C]	T(air) [°C]	Wind velocity [m/s]	T(#1) [°C]	T(#2) [°C]	T(#3) [°C]
07.04	13:20 - 13:25	420	-	-	90.0	71.8	19.9
07.04	14:57 - 14:59	431	-	-	95.3	76.5	25.2
08.04	14:14 - 14:16	434	21	0.9 - 2.12	101.8	88.8	25.2

was the case at the sensors position on the swivel joint. The sensitivity deviation over temperature for the sensor KS95B.100 is given in figure 3.12.
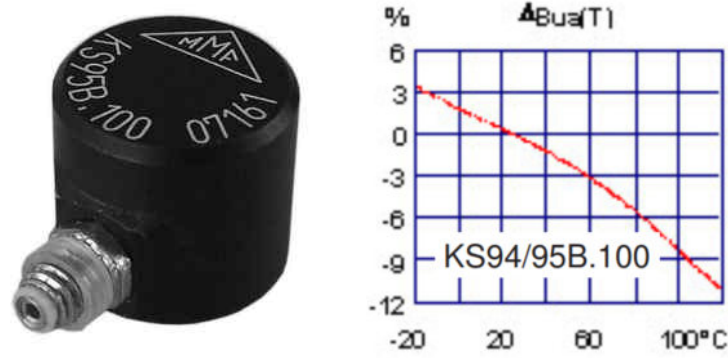
Figure 3.12.: KS95B.100 sensor (left) and its sensitivity deviation over temperature (right) [27]

As seen in figure 3.13, one sensor KS95B.100 was screwed to the swivel joint located on the east side of the test bench, and two sensors were screwed to the swivel joint on the west side of the facility. The sensors were connected to an InnoBeamer L2, which is a data acquisition (DAQ) device shown in figure 3.15. Then, the InnoBeamer L2 is connected to a laptop that records and saves the vibration data.
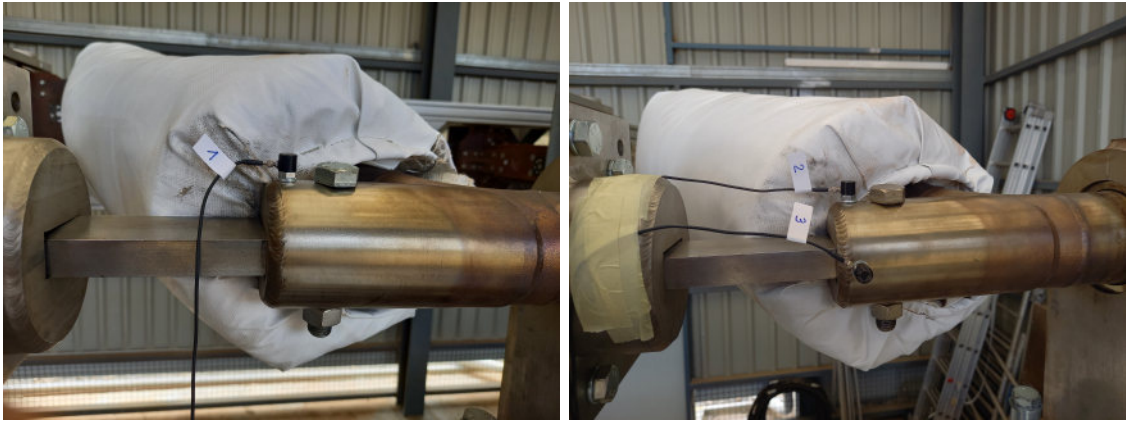
Figure 3.13.: One accelerometer KS95B.100 screwed to the east swivel joint (left) and two accelerometers KS95B.100 screwed to the west swivel joint (right)

3.3.2. Setup with the sensors 320C52

Because of the aforementioned disadvantage of sensors type KS95B.100, the initial setup was replaced by a new one, that includes four sensors type 320C52. The biggest advantage using the sensors 320C52 is their stable and low sensitivity deviation over temperature, as can be seen in figure 3.16. As shown in figure 3.17, two sensors were screwed to the east swivel joint and two sensors were installed at the west swivel joint.

Figure 3.14.: Closeup of accelerometer KS95B.100 screwed to the swivel joint

Figure 3.15.: Data acquisition device InnoBeamer L2[16]
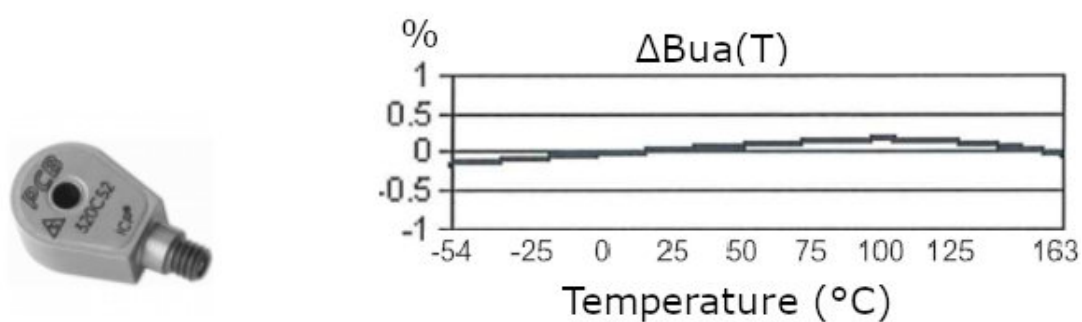
Figure 3.16.: 320C52 sensor (left) and its sensitivity deviation over temperature (right)
[15]
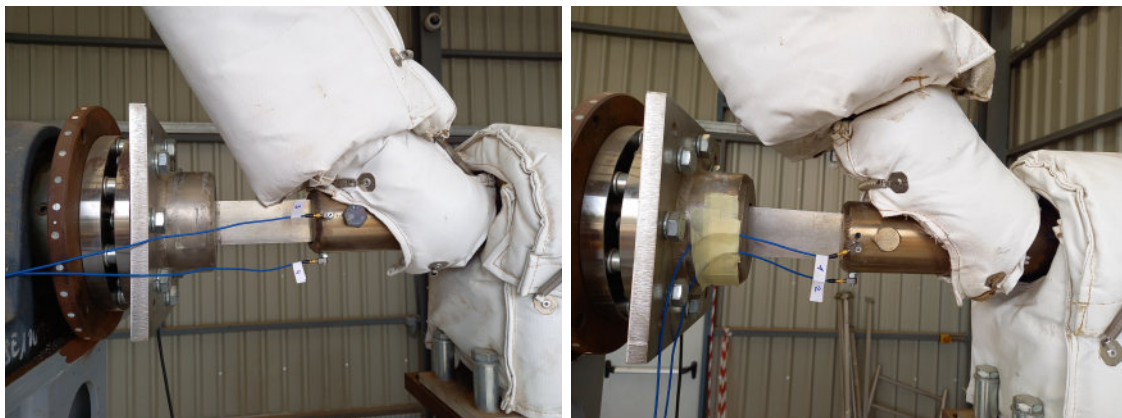
Figure 3.17.: Two accelerometers 320C52 screwed to the east swivel joint (left) and two accelerometers 320C52 screwed to the west swivel joint (right)
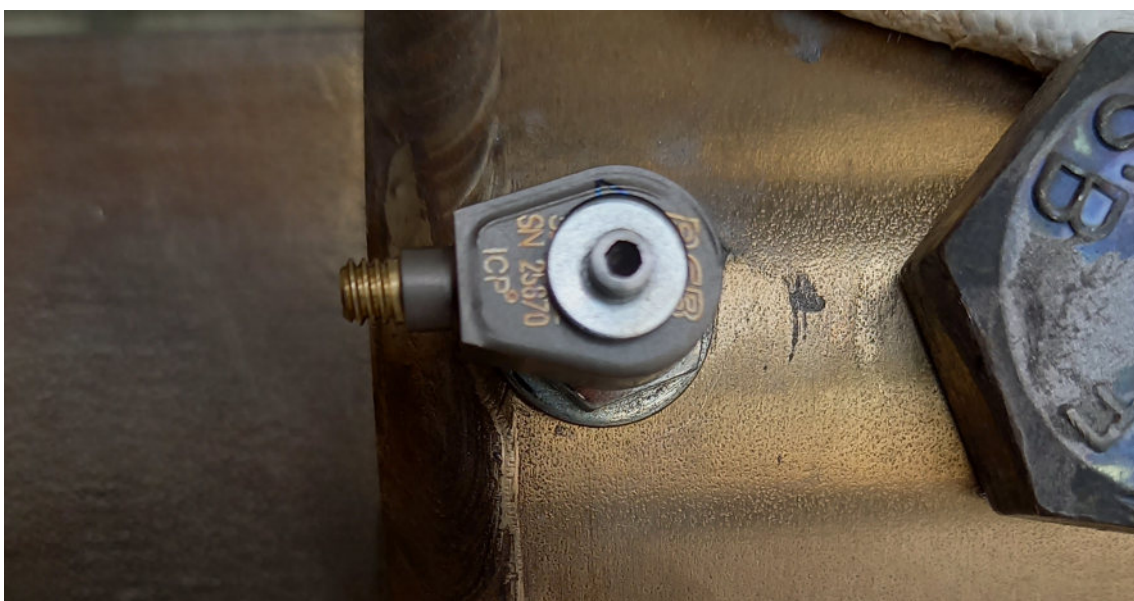
Figure 3.18.: Closeup of accelerometer 320C52 screwed to the swivel joint

3.3.3. Calibration test

Due to the significant uncertainty of the measurements at high temperatures with KS95B.100 sensors, a calibration test was designed and performed. For this purpose, KS95B.100 sensors were screwed on a piece of metal plate, as shown in figure 3.19. Two 320C52 sensors, which had been already calibrated by the manufacturer, were also screwed on the metal plate, next to the KS95B.100 sensor that is being tested. The 320C52 sensor closest to the KS95B.100 is chosen as the reference sensor. A drilling machine is used to drill into a point that is equally distant from the reference sensor and the KS95B.100 sensor, while the produced vibrations are logged. The same procedure is followed for all three KS95B.100 sensors.
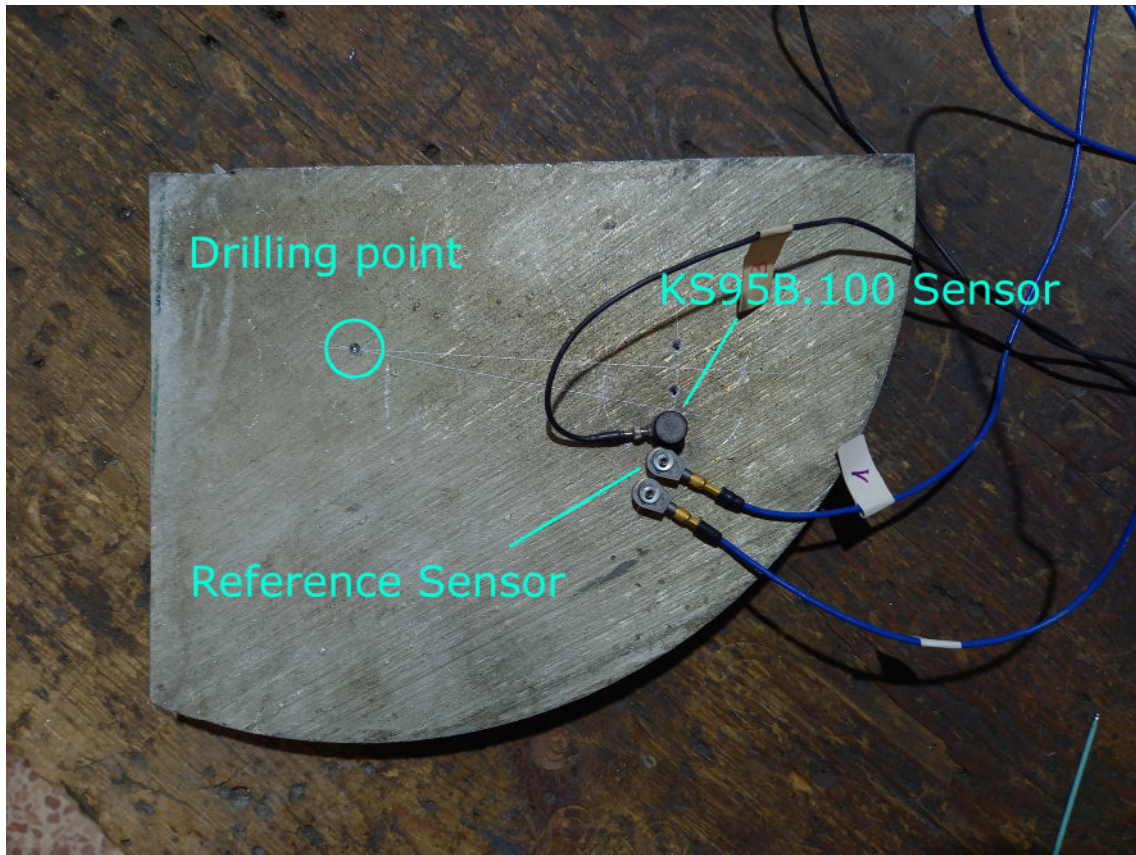
Figure 3.19.: Calibration setup

In addition, Fourier Transform is performed on the measured signal after the calibration. The resulted spectra are shown in figures 3.20, 3.21 and 3.22. A spectrum shows which frequencies are present in a signal and their amplitudes. It can be seen that all three KS95B.100 sensors measured the same frequencies as the reference sensor. However, for some frequencies the amplitudes are slightly lower which can be due to the fact that the sensors are not at the same position and therefore slight differences in the vibrations are expected. All things considered, the calibration test was successful and the measurements of KS95B.100 sensors could be validated for the tests that were performed at ambient temperature.
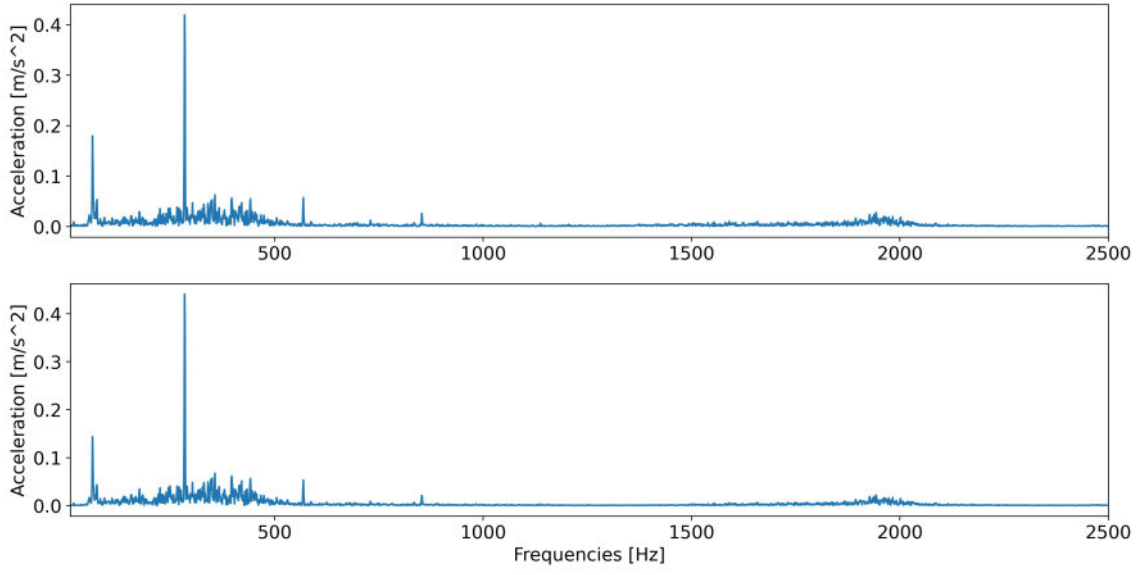
Figure 3.20.: Spectrum of signal measured by 320C52 reference sensor (top) and spectrum of signal measured by first KS95B.100 sensor (bottom)
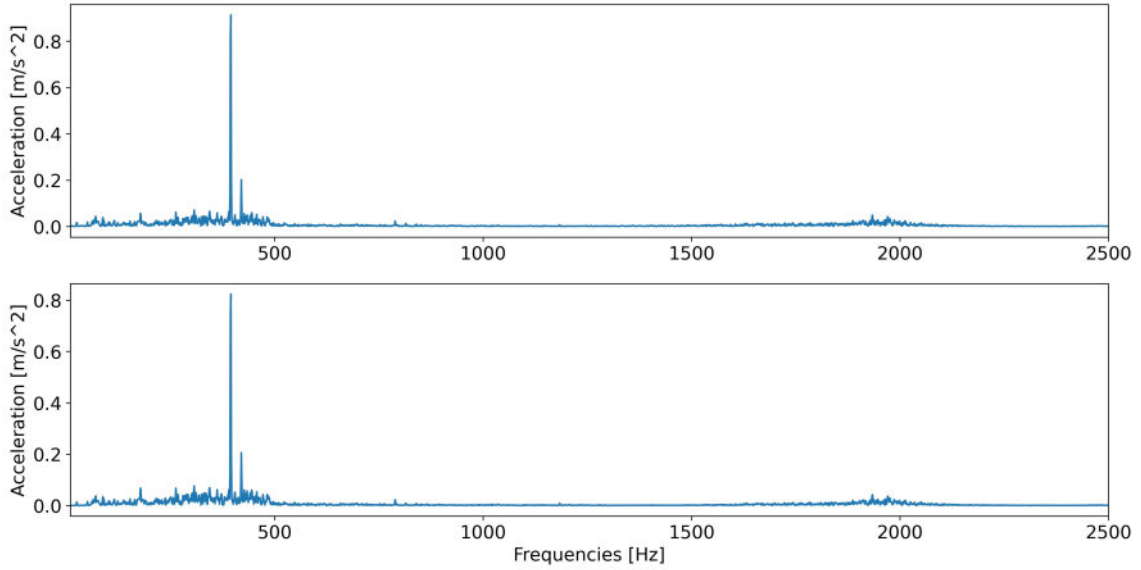
Figure 3.21.: Spectrum of signal measured by 320C52 reference sensor (top) and spectrum of signal measured by second KS95B.100 sensor (bottom)
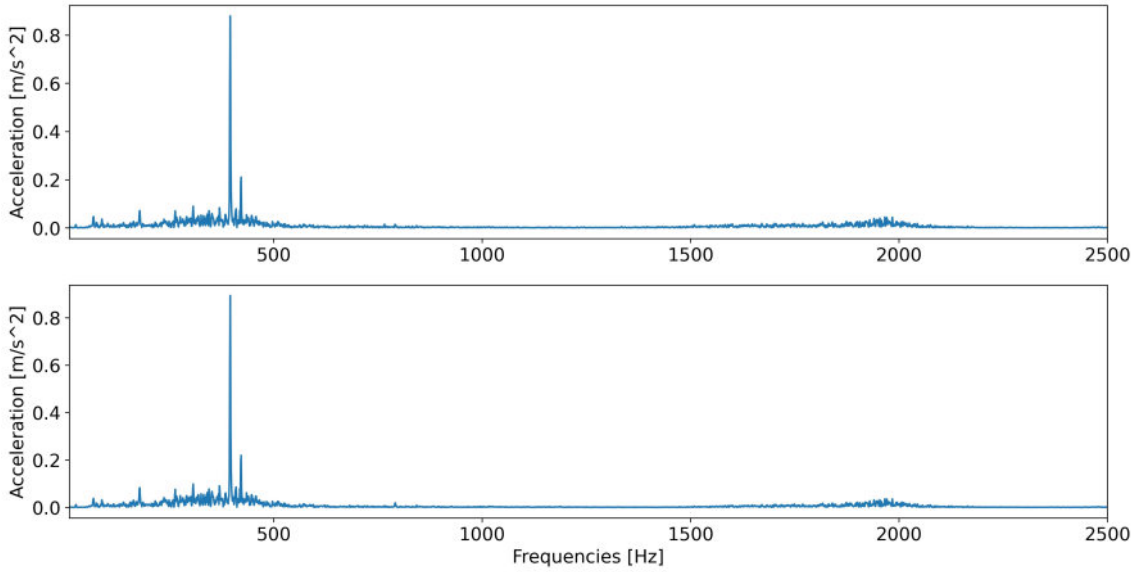
Figure 3.22.: Spectrum of signal measured by 320C52 reference sensor (top) and spectrum of signal measured by third KS95B.100 sensor (bottom)

3.3.4. Temperature verification test at the REPA test rig

After the successful calibration of the KS95B.100 sensors a temperature verification test was done at the REPA test rig at operation with an HTF temperature of 393 °C. The goal was to check the real temperatures during the test cycles that can be obtained at the locations where the sensors were installed. The thermocouples were connected close to the sensors that were screwed on perpendicular to the REPAs, as these are the sensors closest to the swivel joint. Figure 3.23 shows the position of the thermocouple on the east swivel joint.

The highest measured temperature on the east swivel joint was 164.8 °C and on the west swivel joint it was 157.5 °C, which is significantly higher than the maximum temperature of 120 °C the KS95B.100 sensors are supposed to withstand. For this reason all measurements that were done with the KS95B.100 sensors during operation at an HTF temperature of 393 °C were discarded.
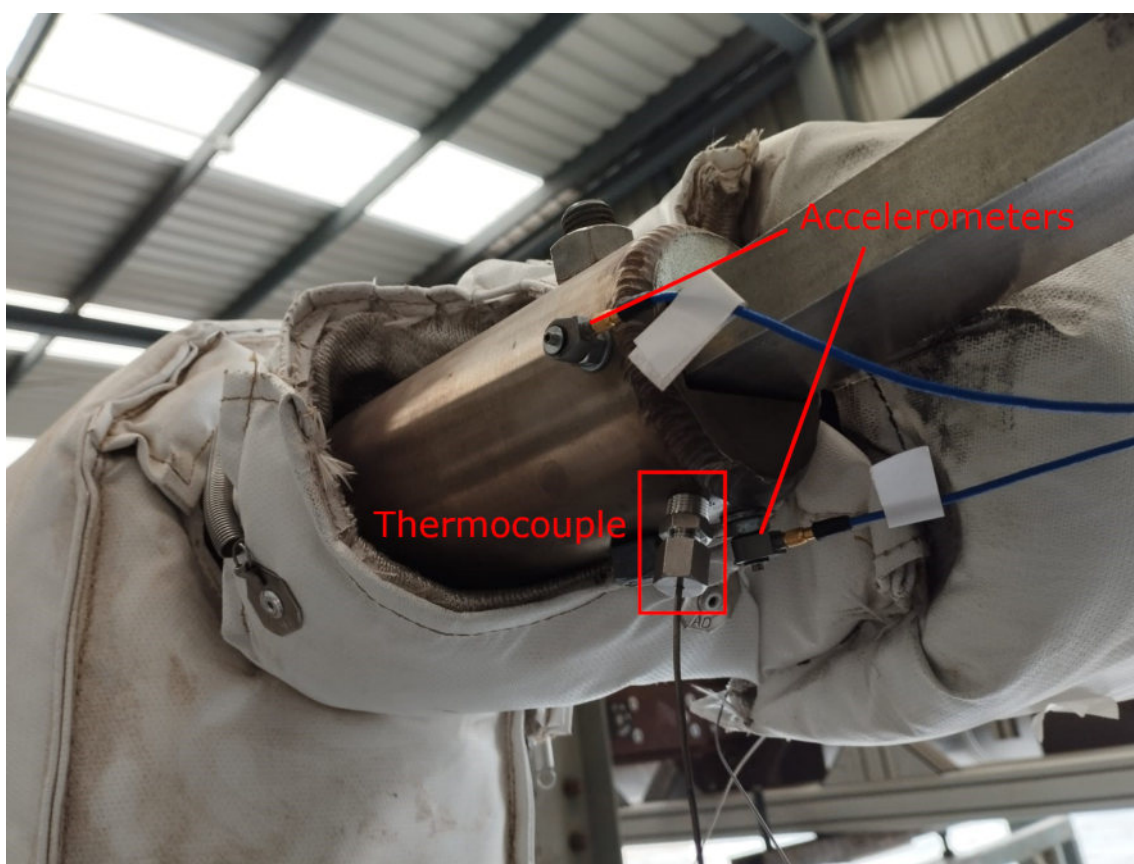
Figure 3.23.: Thermocouple on the east swivel joint close to the accelerometer screwed on
perpendicular to the REPA

4. Vibration Analysis

Generally, when vibrations are analyzed or used in condition monitoring the following steps are at least partially included. [43]
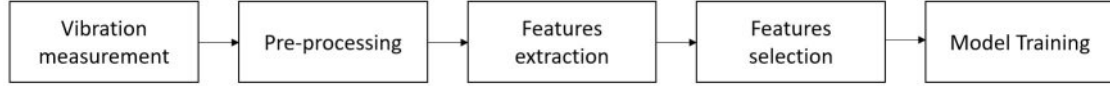
Figure 4.1.: Typical steps included in condition monitoring using vibrations [44]

The result of this process is a trained classifier that can be used to make predicitons. [44] Pre-processing can be done during the vibration measurement e.g. the use of filters to avoid aliasing, explained in section 4.1.1, [34] or after the vibration measurement e.g. denoising [6]. The steps feature extraction and selection, classification and model comparison are explained in the following. Features are parameters that describe the samples that are measured. So, in the given case a sample is a fragment of the measured vibrations and a feature could be e.g. the mean of the sample.

4.1. Feature Extraction

Features are extracted to describe the signal. These features include information about the frequency domain or statistical parameters. In the following section Short Time Fourier Transform (STFT), one of the most used methods of time-frequency analysis, is introduced as well as statistical parameters that characterize a signal. Another feature introduced is the spectral energy which is calculated using the Power Spectral Density (PSD).

4.1.1. Short Time Fourier Transform (STFT)

The STFT uses the Fourier Transform to calculate which frequencies are present in the signal over time. Firstly, the Fourier Transform is explained to be able to understand the calculations that are made in the STFT.

Fourier Transform

The Fourier Transform (Eq. 4.1) transforms a function from the time domain into the frequency domain. The Fourier Transform calculates which frequencies are present in a given signal. [34]

$$G(f) = \int_{-\infty}^{\infty} g(t)e^{-j2\pi ft}dt \tag{4.1}$$

When dealing with real signals, the measurements are not continuous and the recordings are not finite either. The Discrete Fourier Transform (DFT) is used for this purpose (Eq. 4.2). In this case, the frequencies for which results are calculated are also discretized. [34]

$$G[k] = (1/N) \sum_{n=0}^{N-1} g[n] e^{\frac{-j2\pi kn}{N}} \tag{4.2}$$

where k are the discretized frequencies and N is the length of the signal.

In numerical calculations the Fast Fourier Transform (FFT) is used. The FFT is an algorithm that efficiently calculates the DFT of a signal. [34]

The following simple examples are given to explain a few concepts concerning the Fourier Transform. Figure 4.2 shows an example of a signal (Eq. 4.3) that consists of a sum of three sinus functions with frequencies 10 Hz, 30 Hz and 100 Hz with the amplitudes 2, 5 and 3 respectively. The signal is generated with a sampling frequency of $f_s = 1000$ Hz and a duration of 2 seconds.

$$y(t) = 2\sin(2\pi * 10t) + 5\sin(2\pi * 30t) + 3\sin(2\pi * 100t) \tag{4.3}$$
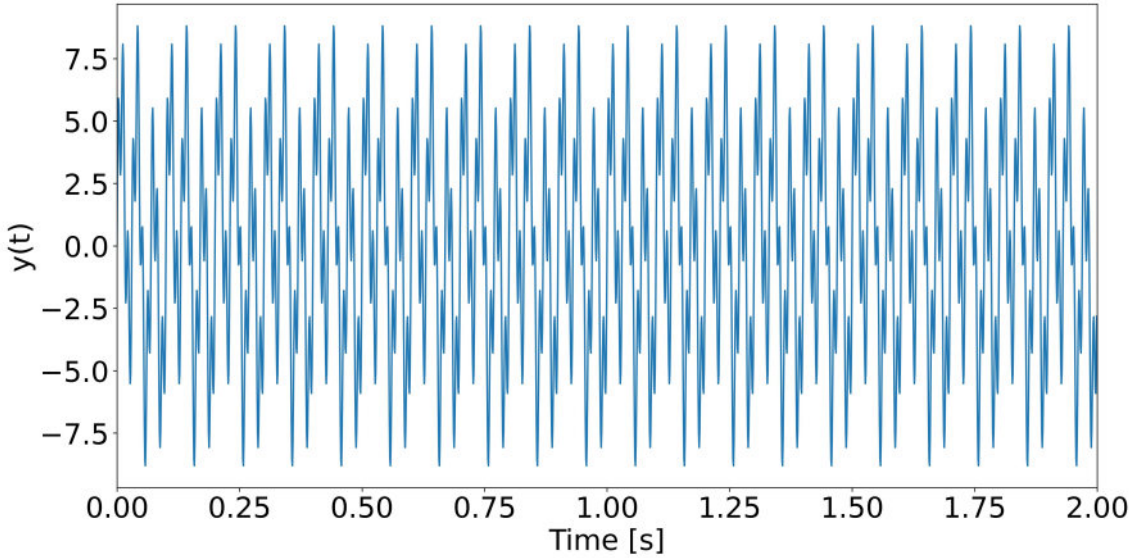
Figure 4.2.: Example of a signal (Eq. 4.3) that consists of a sum of three sinus functions

It would be very difficult to understand the signal only from the information given by figure 4.2. In figure 4.3 the frequency spectrum of the given example is shown. A frequency spectrum shows which frequencies are present in a signal and also their amplitudes. The results for the spectrum were calculated using the FFT. By looking at the spectrum in figure 4.3, it can be seen that the signal consists of three sinus functions with frequencies 10 Hz, 30 Hz and 100 Hz with the amplitudes 2, 5, and 3 respectively.

Nevertheless, there are some issues when using the FFT that lead to false results. These include aliasing and spectral leakage, which are introduced in the following.

When digitizing a signal, the discrete sequence is free of distortion (also known as aliasing) when the highest frequency present in the signal is lower than the Nyquist frequency, f_N,
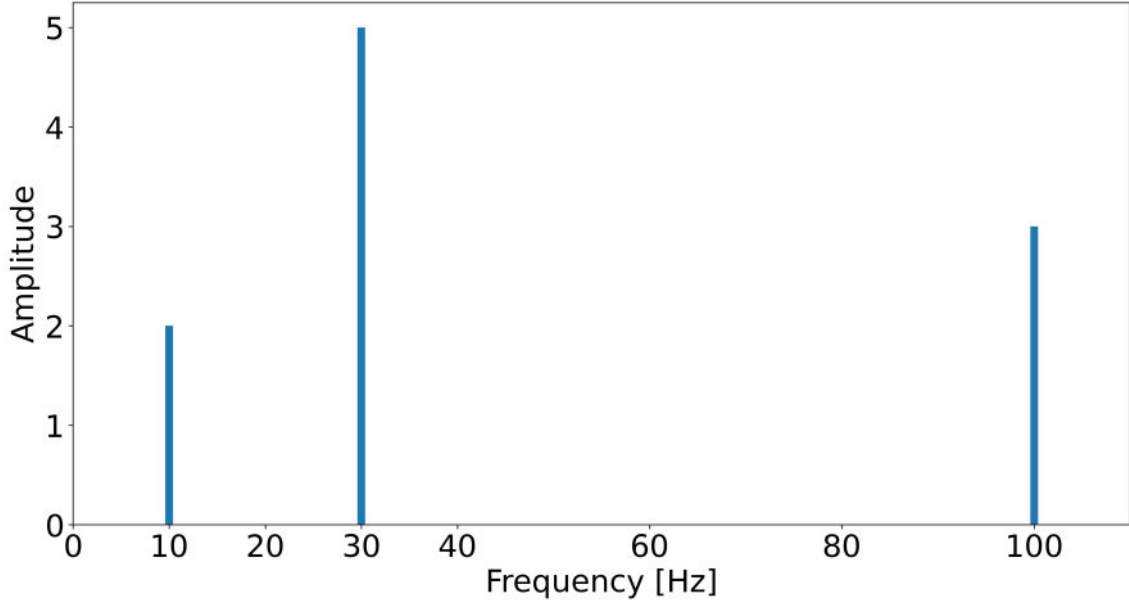
Figure 4.3.: Spectrum of the given signal (Eq. 4.3)

which is equal to half of the sampling rate. If aliasing occurs during the digitizing of a signal, higher frequencies will appear as lower frequencies when processing the digitized signal. [26]

In figure 4.4 there is an example given for a signal (Eq. 4.4) that consists of a sinus function with a frequency of $f_1 = 700$ Hz and an amplitude of 1. The signal is generated with a sampling frequency of $f_s = 1000$ Hz and a duration of 2 seconds. In this case aliasing will occur as the highest frequency in the signal is higher than the Nyquist frequency $f_1 >= f_N = f_s/2$.

$$y(t) = \sin(2\pi * 700t) \tag{4.4}$$

Even though the signal only includes a sinus function with a frequency of $f = 700$ Hz, the spectrum calculated with the FFT, shown in figure 4.5, also shows us that the signal includes a sinus function with a frequency of $f = 350$ Hz, which is not correct.

For this reason, when measuring data, anti-aliasing filters are used before the signal is digitized. An anti-aliasing filter would ideally only let frequencies lower than the Nyquist frequency pass. But a practical anti-aliasing filter either permits some aliasing to occur or it lets the frequencies right under the Nyquist frequency get distorted. [26]

Spectral leakage depends on the length of the signal on which the Fourier Transform is performed. If the signal contains an integer number of periods of a sinusoid, spectral leakage will not occur. When this is not the case, energy from a single frequency will spread or "leak" to the neighbouring frequencies. [34]

In the following, an example is given for a signal that consists of two sinus functions (Eq. 4.5) and is constructed with a sample rate of $f_s = 1000$ Hz.
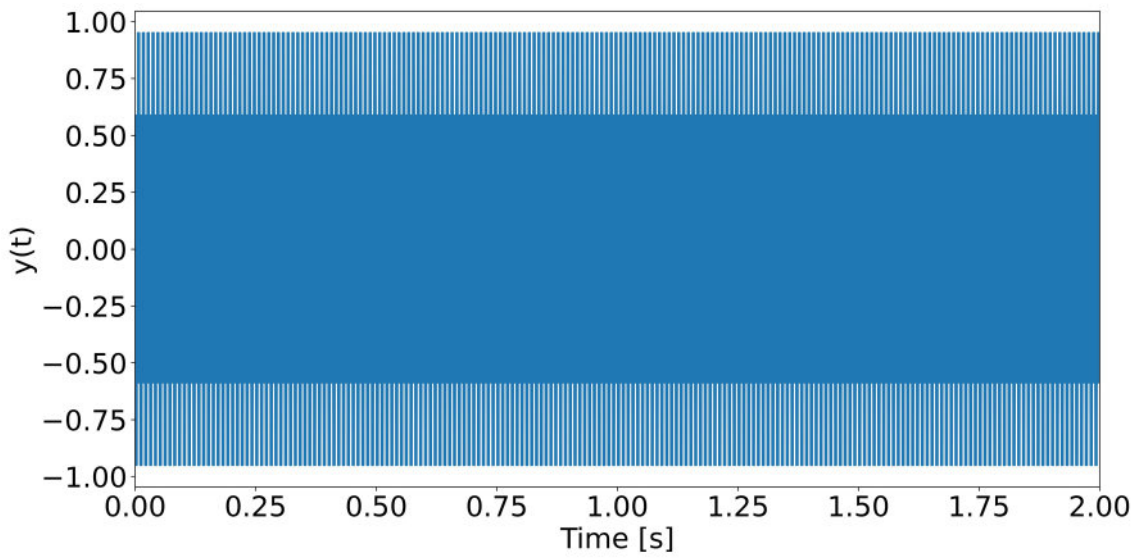
Figure 4.4.: Example of a signal (Eq. 4.4) that consits of one sinus function with a frequency of $f_1 = 700$ Hz. The signal is generated with a sampling frequency of $f_s = 1000$ Hz. Aliasing is occuring as f_1 is higher than the Nyquist frequency $f_N = f_s/2$.
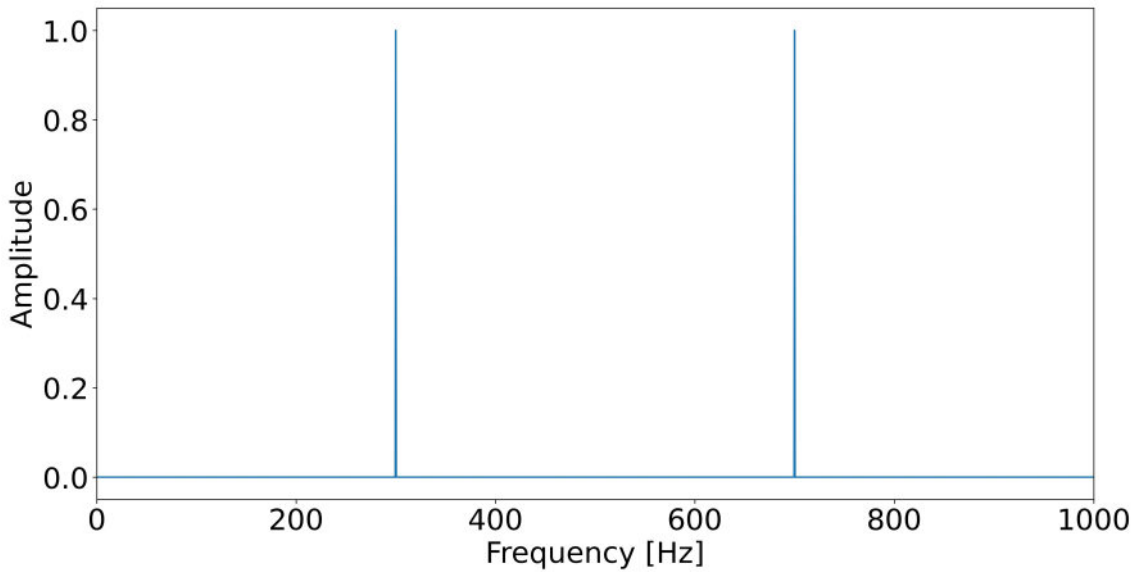
Figure 4.5.: Spectrum of the given signal (Eq. 4.4), which only consits of a sinus function with the frequency of $f_1 = 700$ Hz. The signal is generated with a sampling frequency of $f_s = 1000$ Hz. Aliasing occurs as the frequency of the signal is higher than the Nyquist frequency.

$$y(t) = \sin(2\pi * 7t) + \sin(2\pi * 13t) \tag{4.5}$$

In figure 4.6, the previous signal is shown for a duration of 2 seconds (left side) and its Fourier Transform is depicted (right side). In this case, spectral leakage is not present since the signal contains an integer number of periods of the sinusoids.
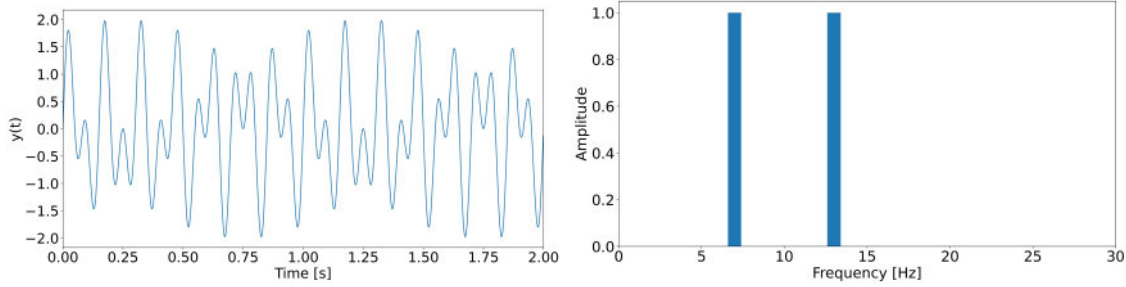
Figure 4.6.: Signal ($y(t) = \sin(2\pi * 7t) + \sin(2\pi * 13t)$) that lasts 2 seconds (left), Fourier Transform of that signal: spectral leakage is not present (right)

In figure 4.7, the same signal (left side) and its Fourier Transform (right side) are given but now the duration of the signal is 1.5 seconds. In this case, spectral leakage occurs because the signal does not contain an integer number of periods of the sinusoids.
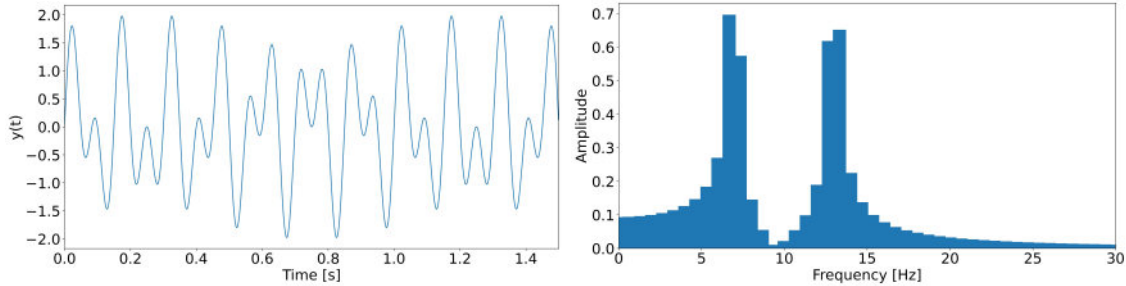
Figure 4.7.: Signal ($y(t) = \sin(2\pi * 7t) + \sin(2\pi * 13t)$) that lasts 1.5 seconds (left), Fourier Transform of that signal: spectral leakage is present (right)

One approach to reduce spectral leakage is to multiply window functions with the signal. Window functions reduce the effect of discontinuity and make the signal periodic. In figure 4.8 a Hanning window is shown, which is known as a good window for general purpose. Moreover, other windows such as Kaiser-Bessel window, Hamming window and Flat-Top window are also used, having all of them their corresponding advantages and disadvantages. [34]

Figure 4.9 shows the Fourier Transform of the same signal (Eq. 4.5) for 1.5 seconds but this time it is multiplied with a Hanning window. Compared to the result in figure 4.7, in which the window function was not used, there is a reduction of the noise around the peaks. The peaks decreased but the relative magnitude stayed the same. In conclusion, although window functions do not completely solve the problem of spectral leakage, they do reduce it.
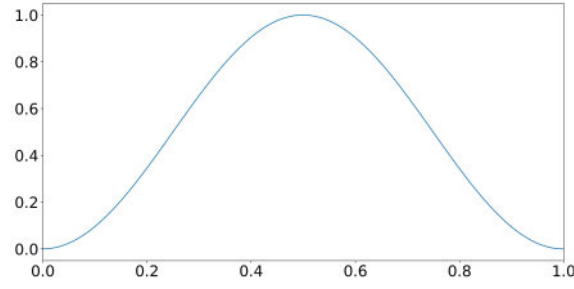
Figure 4.8.: Hanning window
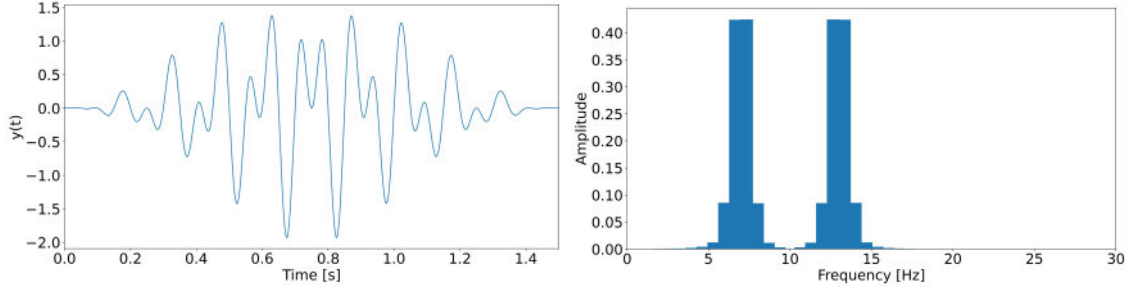
Figure 4.9.: Signal $(y(t) = \sin(2\pi * 7t) + \sin(2\pi * 13t))$ that lasts 1.5 seconds multiplied with a Hanning window (left), Fourier Transform of the signal multiplied with a Hanning window (right)

Short Time Fourier Transform (STFT)

In the frequency spectra, calculated with the Fourier Transform, the frequencies that are present in the signal are given but not the time when these frequencies appear. Here is an example to illustrate this.

The following signal (Eq. 4.6) is given. In the first second it includes two sinus functions with the frequencies 7 Hz and 13 Hz with amplitudes of 1, while in the following second it includes two sinus functions with the frequencies 5 Hz and 15 Hz with amplitudes of 2.

$$y(t) = \begin{cases} \sin(2\pi * 7t) + \sin(2\pi * 13t), 0 \le x \le 1 \\ 2\sin(2\pi * 5t) + 2\sin(2\pi * 15t), 1 < x \le 2 \end{cases} \tag{4.6}$$

In figure 4.10 the signal and its frequency spectrum are given. In the frequency spectrum it can only be seen that there are peaks at 5, 7, 13 and 15 Hz and that the peaks at 5 and 15 Hz are twice as high. However, it can not be deduced when these frequencies are present in the signal.

To get time information, the STFT (shown in Eq. 4.7) moves a short time window along the signal and calculates the frequency spectrum for each window using the Fourier Transform. [34]

$$S(f, \tau) = \int_{-\infty}^{\infty} x(t)w(t - \tau)e^{-j2\pi ft}dt \tag{4.7}$$
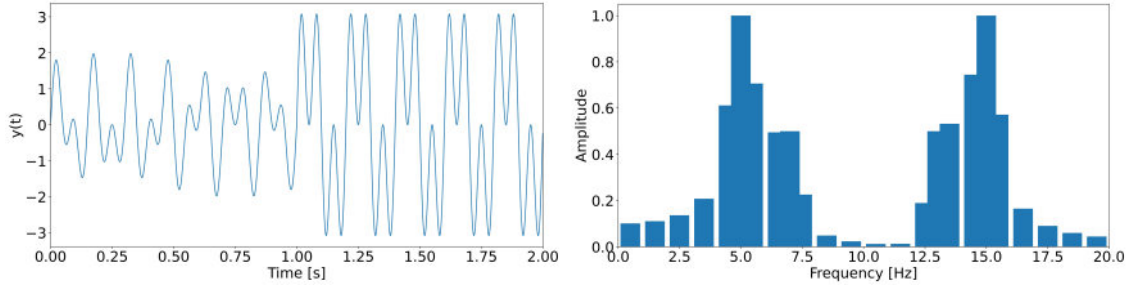
Figure 4.10.: Example of a signal that changes over time 4.6 (left), frequency spectrum of that signal (right)

where $w(t)$ is a window function that is moved along the signal. The window function can for example be a Hanning window.

For real signals the discrete STFT is used [36], as shown in Eq. 4.8:

$$S[k, m] = \sum_{n=0}^{N-1} g[n]w[n]e^{-j2\pi kn} \tag{4.8}$$

The following graphs show how the STFT is calculated. In figure 4.11, a window with the length of 1 second is moved along the signal. There is no overlap between the windows (top graphs). The corresponding frequency spectra are below the signals. Here it can be seen that in the first second only frequencies of 7 and 13 Hz are present while in the next second only frequencies of 5 and 15 Hz are present (bottom graphs). This way, not only the frequencies of the signal are given, but also the times when they occur.
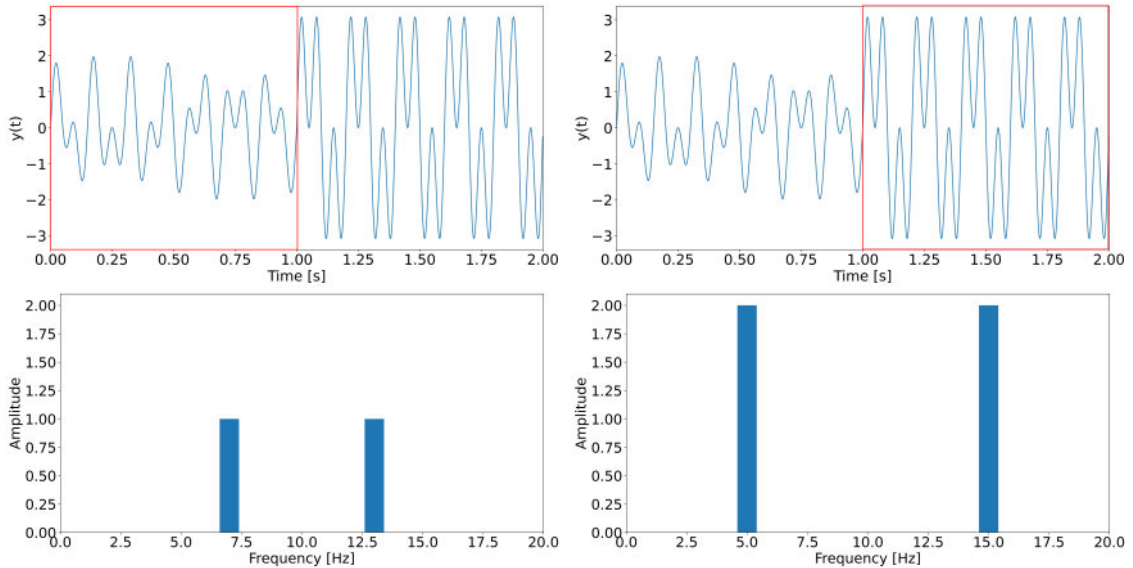
Figure 4.11.: Example of how windows are used: window selection along the signal (top), frequency spectrum of the signal that is inside the window (bottom).

Spectrograms are used to visualize the results of the STFT. In figure 4.12, a spectrogram of signal 4.6 is shown. Along the x-axis the time is given, along the y-axis the frequencies

are given and the colormap describes the amplitudes of the given frequencies. [44] In the given case, in the first second there are frequencies present with 7 and 13 Hz and in the subsequent second there are frequencies present with 5 and 15 Hz.
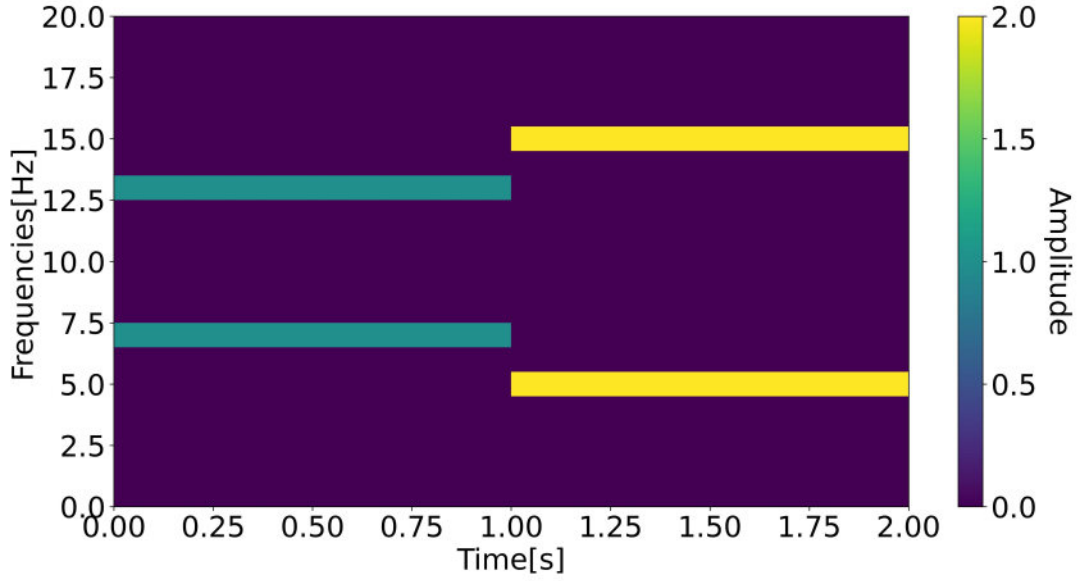
Figure 4.12.: Spectrogram of the signal given in equation 4.6

According to the uncertainty principle, the time resolution is reciprocal to the frequency resolution. This means that the smaller the length of the window is, the higher the time resolution gets, but at the same time frequency resolution gets lost. [34]

Often the Power Spectral Density (PSD) is given. The PSD is calculated using the square of the Fourier Transform. A PSD for the signal given in equation 4.6 is shown in figure 4.13.
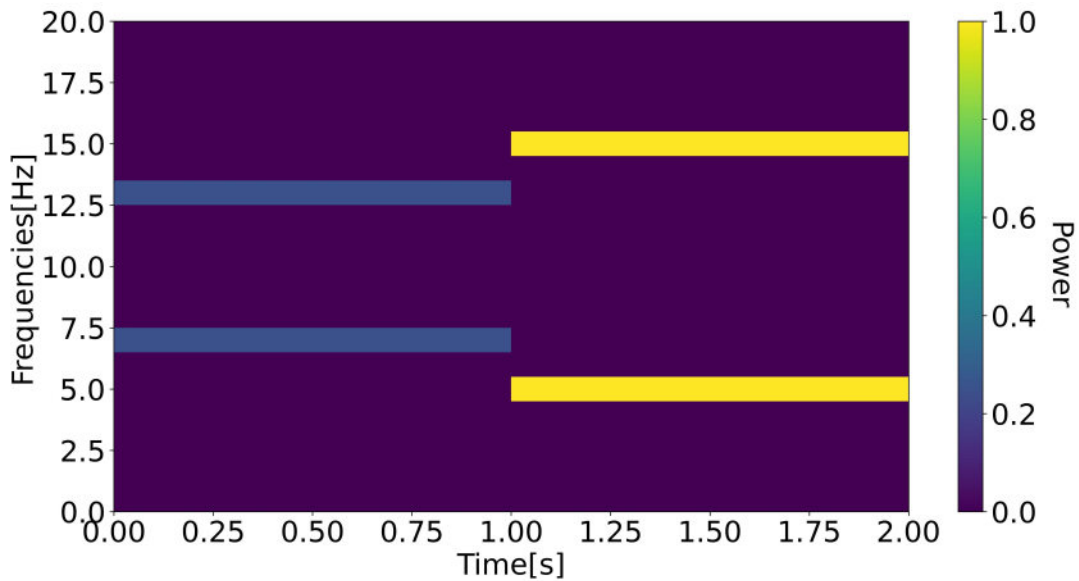
Figure 4.13.: Power Spectral Density of the signal given in equation 4.6

4.1.2. Spectral Energy

A feature that can be extracted using frequency analysis is the spectral energy. [22] For this, the PSD is used. The PSD is the square of the STFT. An example of PSD is given in figure 4.14, which shows the power over frequency and time. Power in this case is acceleration squared divided by the sample rate with the unit of $(m/s^2)^2/Hz$. Spectral energy is the power integrated over time and has the unit $s \cdot (m/s^2)^2/Hz$. [34]
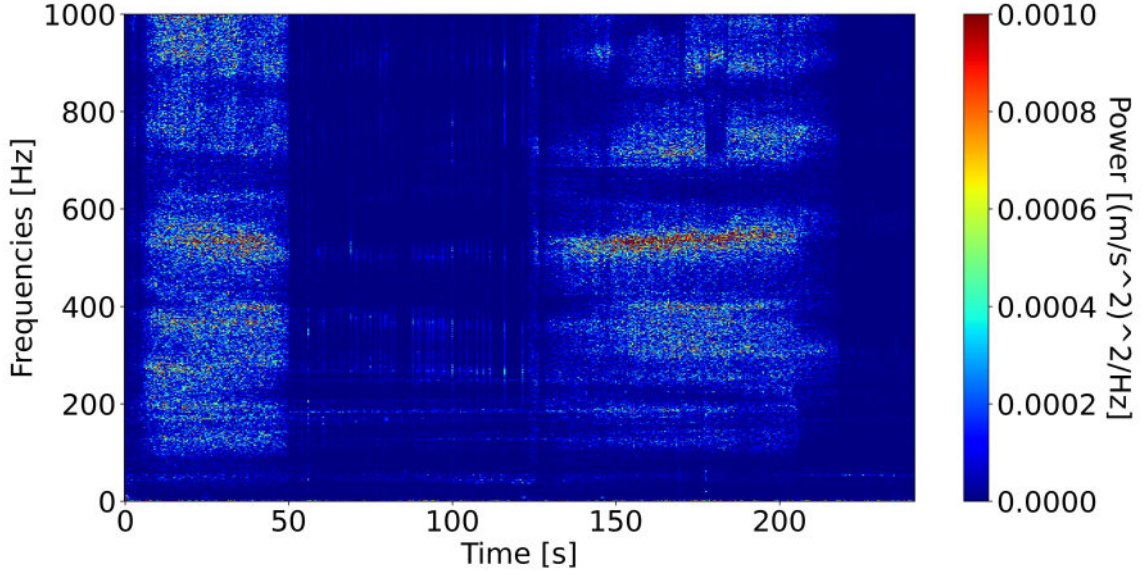
Figure 4.14.: Example of a Power Spectral Density

Spectral energy can be integrated over all frequencies or over a specific frequency bin. As the PSD shows discrete values, the integration becomes a summation of the values over time and over frequencies.
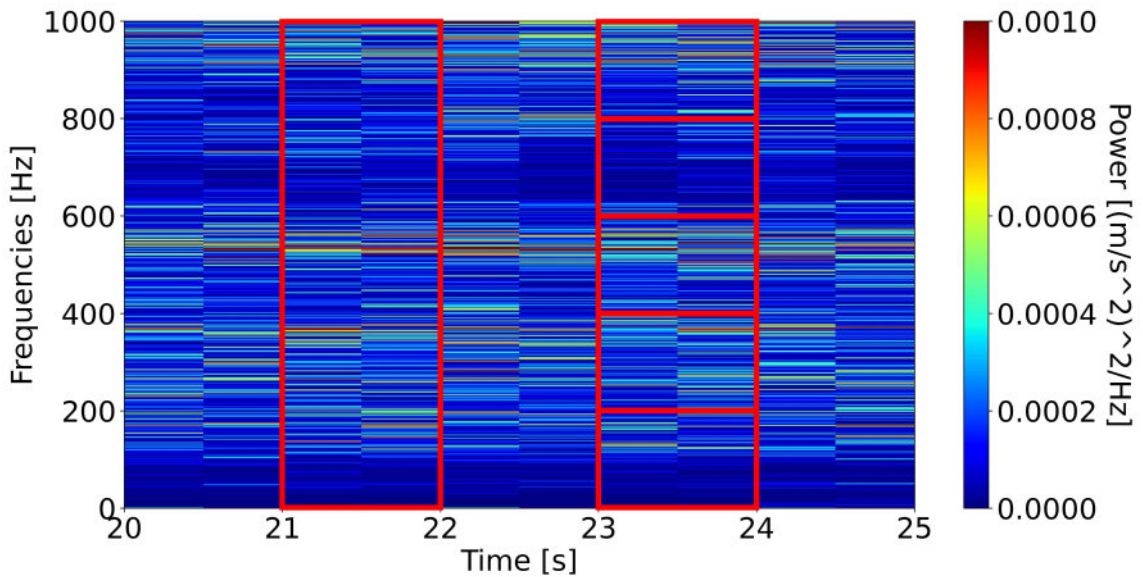
Figure 4.15.: Power Spectral Density with marked frequency bins

Figure 4.15 shows the same PSD as in figure 4.14 but only for a few seconds. From 21 to 22 seconds all the frequencies are marked. From 23 to 24 seconds the frequencies are divided into five equally wide frequency bins. To calculate the energy of all frequencies for one second for example, all the values of the PSD during this second have to be added up as shown in the PSD from 21 to 22 seconds. To calculate the energy of a frequency bin for one second for example, all the values of the PSD during this second and within this frequency bin have to be added up as shown in the PSD from 23 to 24 seconds.

The spectral energy of all the frequencies for the PSD in figure 4.14 is shown in figure 4.16. The spectral energy was calculated by integrating the power for each second. The spectral energy for the frequency bin from 600 to 800 Hz is shown in figure 4.17.
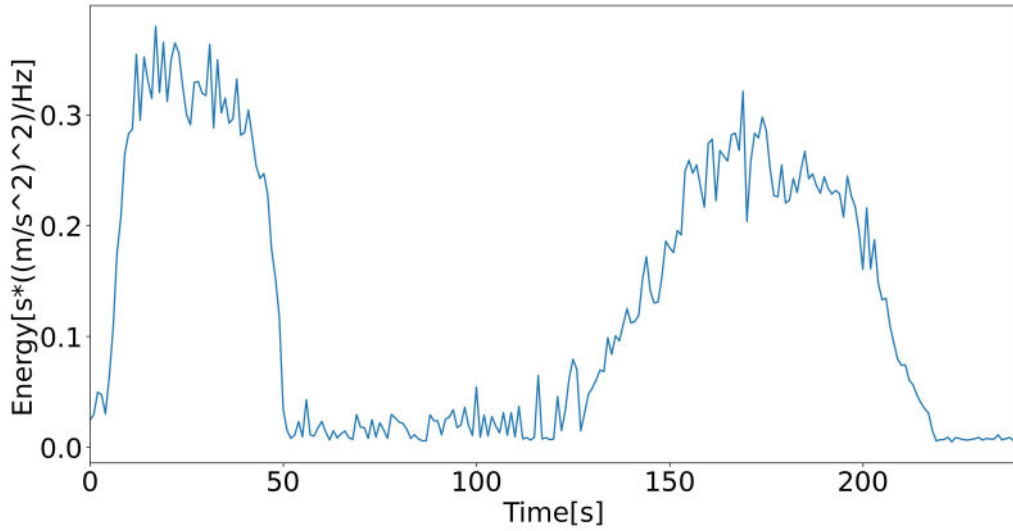
Figure 4.16.: Spectral energy for each second of the given example from figure 4.14
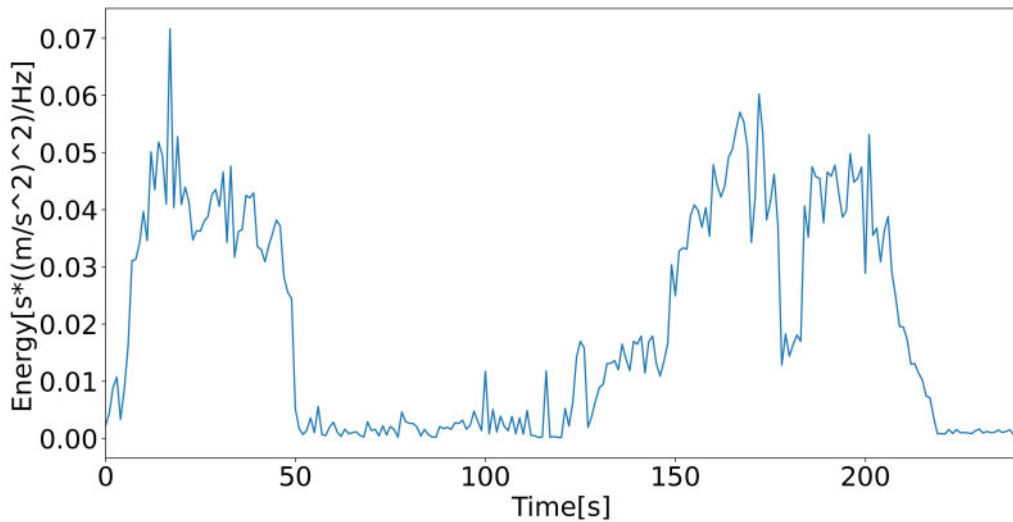
Figure 4.17.: Spectral energy for each second in the frequency bin from 600 Hz to 800 Hz of the given example from figure 4.14

4.1.3. Statistical Features

A signal can also be characterized by the distribution of the instantaneous values. These include signal range, mean value, standard deviation, variance, skewness, kurtosis, crest factor, among others.

The formulas for the most used statistical features are given in the following [22].

- **Range**: Range is the difference between the maximum and minimum values of a signal.

- **Mean value:** Mean value μ is the average value of a signal.

$$\mu = \frac{1}{N} \sum_{i=1}^{N} x_i \tag{4.9}$$

- **Standard deviation**: Standard deviation σ is a measure of variance in a sequence of values. The lower the standard deviation is, the closer the values tend to be to the mean.

$$\sigma = \sqrt{\left(\frac{1}{N-1}\right) \sum_{i=1}^{N} (x_i - \mu)^2} \tag{4.10}$$

- **Variance**: Variance σ^2 is the square of the standard deviation.

$$\sigma^2 = \left(\frac{1}{N-1}\right) \sum_{i=1}^{N} (x_i - \mu)^2 \tag{4.11}$$

- **Skewness**: Skewness S is a measure of asymmetry of a probability distribution.

$$S = \frac{1}{N} \sum_{i=1}^{N} (x_i - \mu)^3 \tag{4.12}$$

- **Kurtosis**: Kurtosis K is a measure of "tailedness" of a probability distribution.

$$K = \frac{\frac{1}{N} \sum_{i=1}^{N} (x_i - \mu)^4}{\sigma^2} \tag{4.13}$$

- **Root Mean Square**: Root Mean Square is the square root of the mean of the square values.

$$x_{rms} = \sqrt{\frac{1}{N} \sum_{i=1}^{N} x_i^2} \tag{4.14}$$

- **Crest Factor**: The crest factor is the ratio between the peak value and the root mean square of a sequence.

$$x_{CF} = \frac{x_{peak}}{x_{rms}} \tag{4.15}$$

4.2. Feature Reduction

If too many features are extracted, it can negatively influence the accuracy of the classification that is done in the next step. For this reason, the most important features are selected or the number of features is reduced before implementing classification methods. [41] In addition, by reducing the number of features, samples can be plotted and viewed, thus making it possible to visually analyze the given samples. [35] The most prominent method in machine learning for reducing dimensionality in a data set is Principal Component Analysis (PCA). This algorithm is explained in detail in the next subsection, however there are also other methods such as Linear Discriminant Analysis (LDA), which will not be covered in this thesis. [25]

4.2.1. Principal Component Analysis (PCA)

The PCA is used to reduce the number of dimensions in the data set while maintaining most of the variation. To achieve this, the PCA finds directions along which the variation in the data is maximal. These directions are called Principal Components (PCs), which are linear combinations of the features given in the data set. [35]

$$\boldsymbol{z} = \boldsymbol{a}^T \boldsymbol{x} = \sum_{i=1}^{N} \boldsymbol{a}_i \boldsymbol{x}_i \qquad (4.16)$$

where z are the PCs, x_i are the features that are included in the given samples, a_i are the constants that describe the principal components and N is the number of features. [41]

There are multiple algorithms to calculate the PCA. One of the most implemented algorithms uses Singular Value Decomposition [3] of the data matrix. [45]

The first step in the algorithm is to standardize the data matrix, so that all samples have a mean of zero [45] and variance of one [18]. This is done to overcome the effects that happen because of features having different units or some features having a higher variance. Variables with a higher variance would influence the results of the calculated principal components more, which is often not what is wanted. [18]

The output of the PCA are the principal components in order from highest variance to lowest variance that is accounted for by the principal component.

In figure 4.18 an example of samples is given. PC1 is the first principal component, which has the maximum variance when the samples are projected onto it. This way, the number of dimensions can be reduced, e.g. in the given case to one dimension. This can also be helpful if the samples have more than 3 dimensions. In such cases, there is no way to visualize the data unless the number of dimensions is reduced to 3 or less.

As a result, it has to be chosen how many PCs should be calculated. If too few PCs are calculated, the necessary information will get lost, resulting in a poor model. If too many PCs are calculated, there will be too many parameters in the classification step. There are multiple ways to choose an adequate number. One of them is by looking at
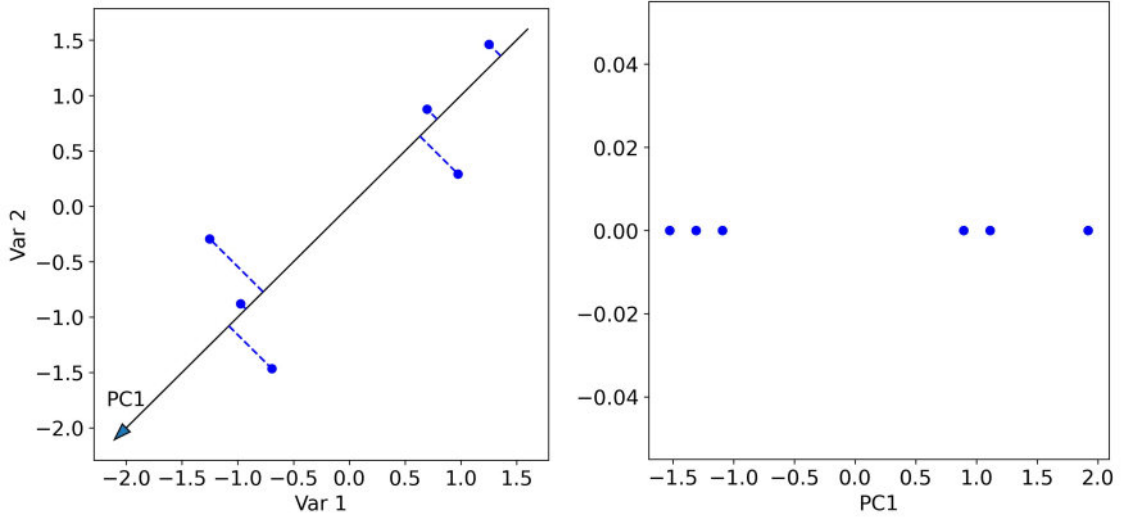
Figure 4.18.: Samples and their projections on the first principal component (left), same samples on the first principal component, number of dimensions is reduced to one (right)

the cumulative percent variance (CPV) shown in equation 4.17. A number of PCs is then chosen so that the CPV is higher than a set value (e.g. 90 %). The optimal value depends on the implemented case. [45]

$$CPV = \frac{\sum_{i=1}^{r} \lambda_i}{\sum_{i=1}^{n} \lambda_i} \tag{4.17}$$

where λ_i is the ratio of the variance of the i-th principal component PC_i to the sum of variances of all principal components.

4.3. Classification

In this section some basic concepts in classification problems are explained. Afterwards, Support Vector Machines (SVM) are explained as an algorithm used in classification. Although there are other algorithms such as Artifical Neural Networks (ANN) and Convolutional Neural Networks (CNN) [43], only SVM was used in the scope of this thesis.

4.3.1. Classification problems

In classification problems samples are available that can be divided into categories or classes. The goal of classification problems is to assign a label to unlabeled samples. For this a classification model is trained and validated. The data set is divided into a training and testing data set. The model is trained using the training data set and then validated using the testing data set. The ratio for the training and testing data sets can for example be 75:25. To validate a model the accuracy (Eq. 4.18) [42] can be calculated. [20]

$$\text{accuracy} = \frac{\text{correct predictions}}{\text{all predictions}} \tag{4.18}$$

Another validation method is the n-fold cross-validation. Here the data are divided into n subsets with equal sizes. A model is then trained n times and every time another subset is used for validation. For every model a classification accuracy is calculated and the average is considered to be the final accuracy. [20] Figure 4.19 shows an example of 4-fold cross validation.
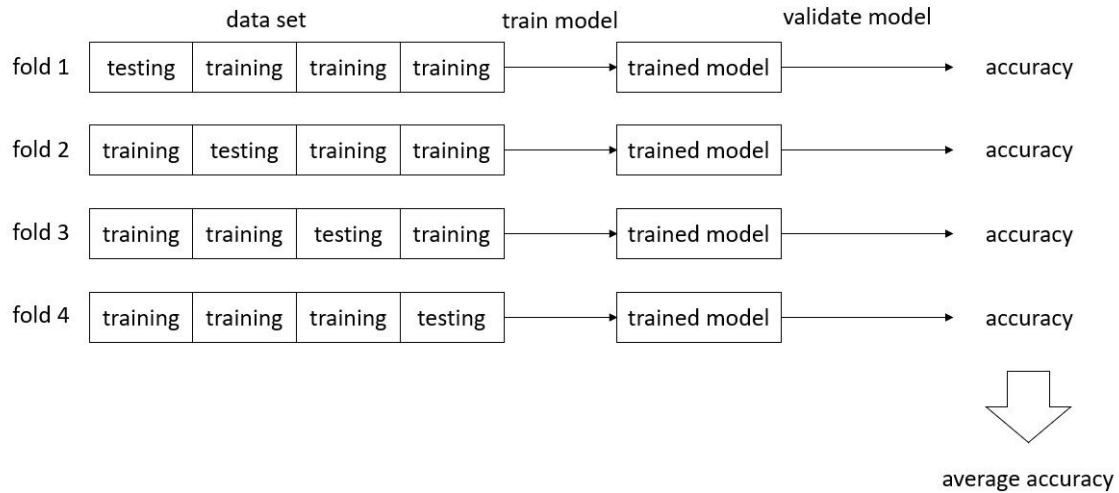
Figure 4.19.: Example of 4-fold cross validation: The data set is divided into four equally sized subsets. The model is trained four times while every time another subset is used as the testing data set for the validation. [20]

A problem that occurs while training a classification model is overfitting. Overfitting happens when a found model classifies the training data with little error but classifies the testing data with a much higher error. In this case the model is very well fitted for the training data but does not find a rule that generally can classify the data overall. Overfitting can occur for example if the model is too complex. [20] Therefore reducing the number of features by using e.g. PCA can lead to better models as overfitting is avoided.

4.3.2. Support Vector Machine

Support Vector Machine (SVM) is a training algorithm for classification and regression. [17]

In the following the four concepts that are incorporated in SVM will be explained: the separating hyperplane, the maximal margin hyperplane, the soft margin and the kernel function.

A hyperplane is a line that separates two groups of samples. The hyperplane has one dimension less than the feature space. For a feature space with two features the hyperplane is a line, for a feature space with three features the hyperplane is a two-dimensional plane and so forth. Usually a lot of hyperplanes exist that meet this condition. The SVM finds

the maximal margin hyperplane. From all the existing hyperplanes the maximal margin hyperplane has the maximal distance from any of the given samples. The samples that are the closest to the hyperplane are called support vectors. [31]

The hyperplane can be described like this [17]:

$$\boldsymbol{w}^T\boldsymbol{x} + b = 0 \tag{4.19}$$

where $\boldsymbol{w}$ is the weight vector and $\boldsymbol{b}$ the bias and the following applies.

$$\boldsymbol{w}^T\boldsymbol{x}_i + b \geq 1, \text{ for all } \boldsymbol{x}_i \in P \tag{4.20}$$

$$\boldsymbol{w}^T\boldsymbol{x}_i + b \leq -1, \text{ for all } \boldsymbol{x}_i \in N \tag{4.21}$$

where $\boldsymbol{x}_i$ are the samples and P and N are the two groups into which the samples can be divided. An example of a one-dimensional hyperplane is shown in figure 4.20.
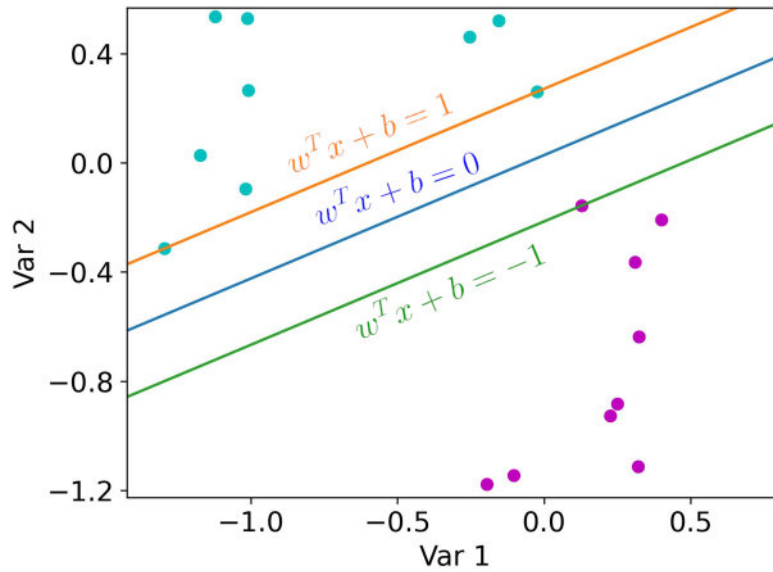
Figure 4.20.: Maximal margin hyperplane (blue) that divides the two groups of samples. The samples that lie on the other two lines are called support vectors. [17]

Until now it was assumed that the two groups of samples can be linearly separated. Very often this is not the case. To deal with this, a soft margin can be used that allows some samples to end up on the side of the other group. The soft margin is controlled by a parameter C. The higher C is set, the smaller the soft margin is and the better the found hyperplane fits the given data set, meaning less samples ending up on the wrong side of the hyperplane. [7] However, high values for C may lead to overfitting and the computational cost is higher. [9]

Another approach to deal with this would be to use a kernel function. The kernel function adds new dimensions to the feature space and projects the samples into a space of higher

dimension. The two groups of samples might be separable in the higher dimensional space, however for this the right kernel function has to be chosen. For any given data set it is possible to find a kernel function that projects the samples in to such a dimension space in which the samples can be linearly separated. However, this leads to overfitting if too many dimensions are added. [31] Using the kernel function is also called the "Kernel Trick". [17]

In figure 4.21 an example of the kernel trick is given. At first there are two groups of samples with only one dimension. The two groups are not linearly separable. After using the kernel function and adding a new dimension the two groups become linearly separable. In this case the kernel function is just the square of the first dimension.
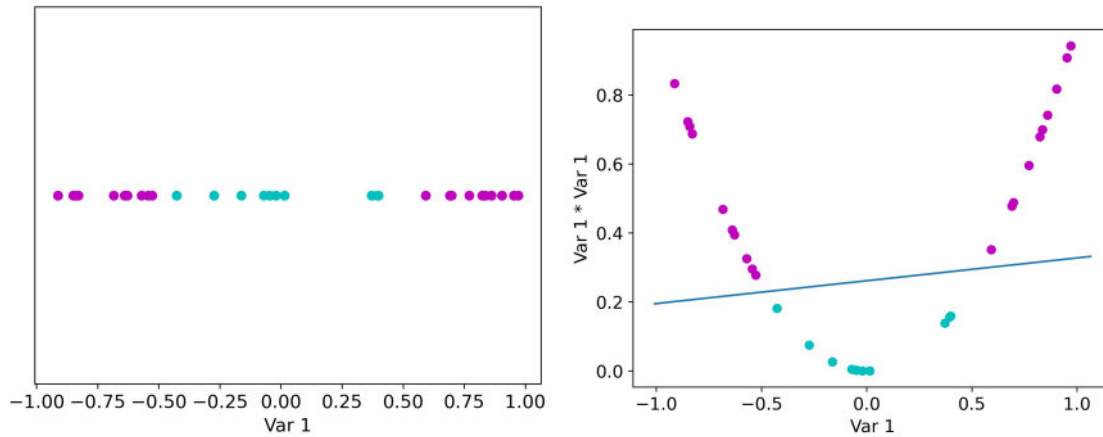
Figure 4.21.: Two groups of samples that are not linearly separable (left), the two groups of samples can be linearly separated after adding a new dimension using the kernel function (right) [31]

39

5. Methodology

5.1. Characteristics of a traverse cycle

In this section traverse cycle's most important characteristics and parameters are explained. Figure 5.1 shows the traverse angle over time while performing a complete cycle, starting from -23.5°, reaching 187° and ending back at -23.5°. These angles are marked with horizontal dotted lines. At the angles 35° and 133° one of the piston changes its movement from pulling to pushing and vice versa. To avoid oscillations the rotation of the traverse is slowed down around these angles, marked with red circles.
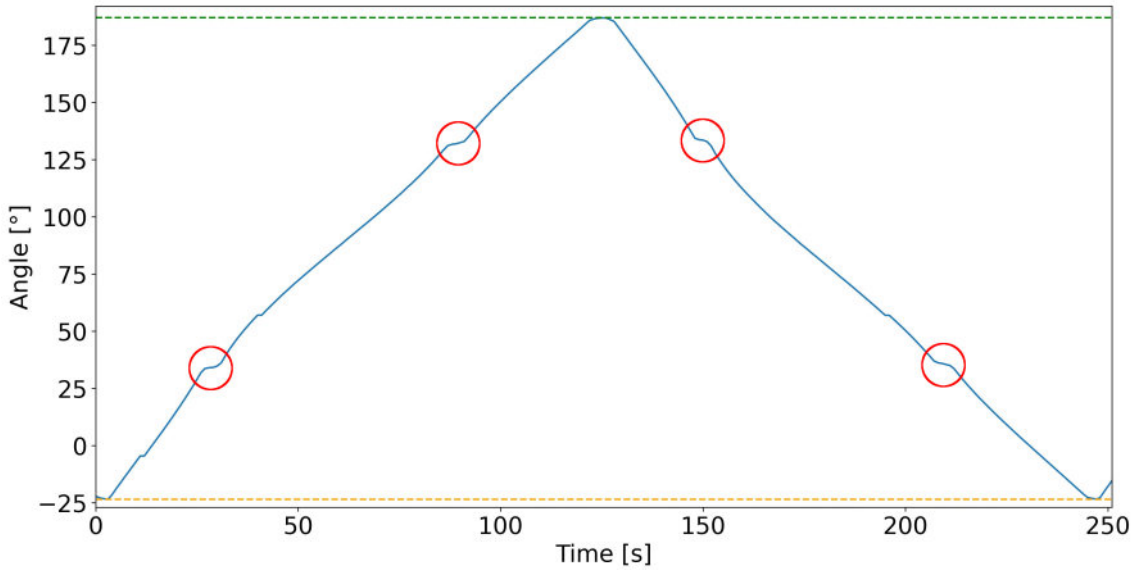
Figure 5.1.: Traverse rotation angle of a cycle

The translation angle of the traverse can also be changed. This is done to simulate the thermal expansion of the receiver tube. However, the consequences of this movement were not studied in this thesis.

To study the vibration behavior of the swivels, spectrograms were calculated with the help of STFT. An example of the spectrogram of a traverse cycle is shown in figure 5.2. As the sample rate of the accelerometers is 10,000 Hz, only the amplitudes of frequencies up to the Nyquist frequency of 5000 Hz can be calculated. In figure 5.2, one can see that almost no vibrations are recorded from 2000 to 5000 Hz, consequently a range of 0 to 2000 Hz has been selected as a reference for the following spectrogram analysis.

One of the features calculated to characterize the vibration is the spectral energy for different frequency bins as shown in section 4.1.2. Note that frequencies under 5 Hz were discarded as the accelerometers are not designed for this bandwidth. The frequency bins for which the spectral energy is calculated can be chosen arbitrarily e.g. divide the frequencies into equally wide frequency bins. However, pertinent frequency bins can be defined after
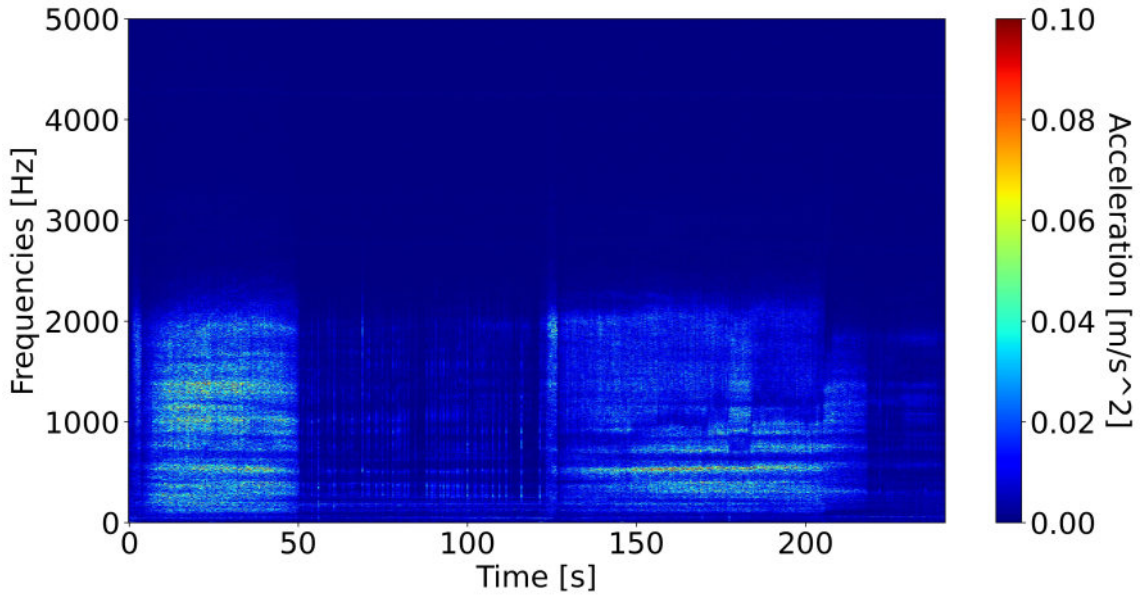
Figure 5.2.: Spectrogram of a cycle

looking at spectrograms and seeing how the vibrations evolve depending on the condition that is analyzed.

To make this point clearer the energy of the vibration from 172 seconds to 190 seconds for the cycle in figure 5.2 is calculated for the frequency bin from 680 to 1180 Hz. The result is shown in figure 5.3. For this frequency bin the energy remains somewhat constant.
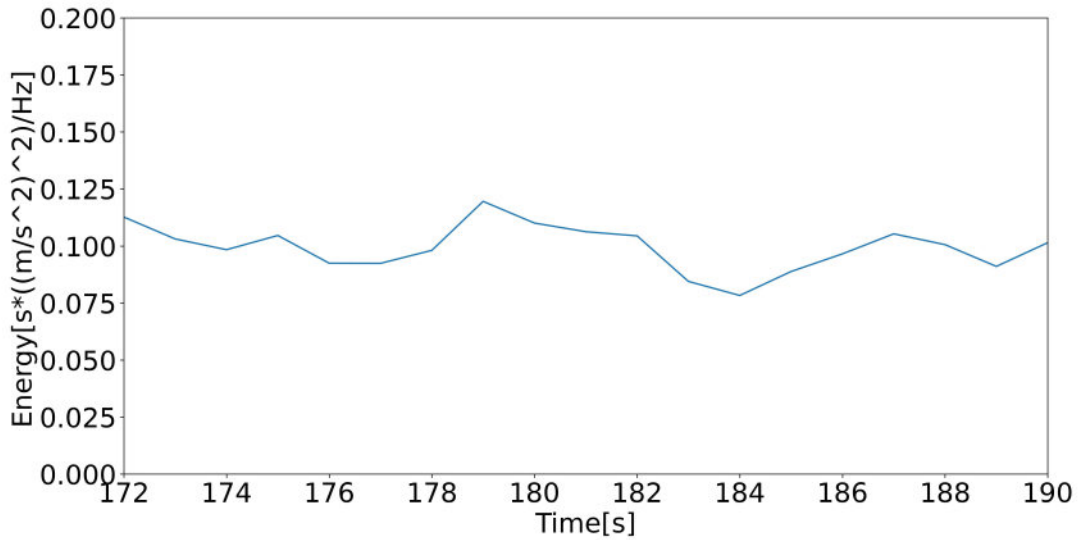
Figure 5.3.: Spectral energy per second from 172 seconds to 190 seconds for the cycle shown in figure 5.2 of the frequency bin from 680 to 1180 Hz

However, if this frequency bin is divided into two frequency bins, one from 680 Hz to 930 Hz and the other one from 930 Hz to 1180 Hz, additional information can be extracted. Figure 5.4 shows the energy for the frequency bin from 680 Hz to 930 Hz and figure 5.5 shows the energy for the frequency bin from 930 Hz to 1180 Hz. An energy shift can be

observed from the first frequency bin to the second one from 177 seconds till 184 seconds. This behavior can not be seen in figure 5.3.
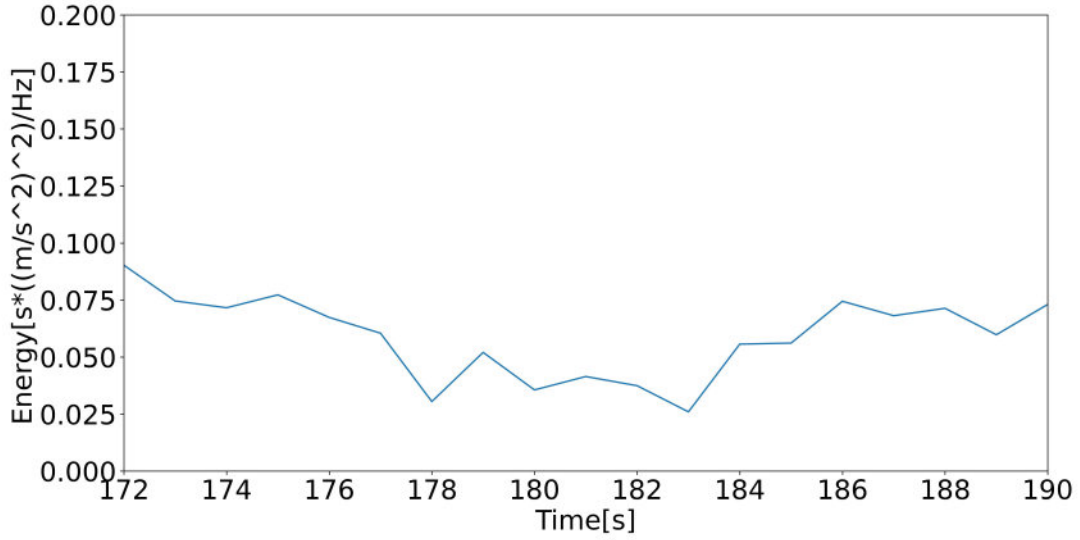
Figure 5.4.: Spectral energy per second from 172 seconds to 190 seconds for the cycle shown in figure 5.2 of the frequency bin from 680 to 930 Hz
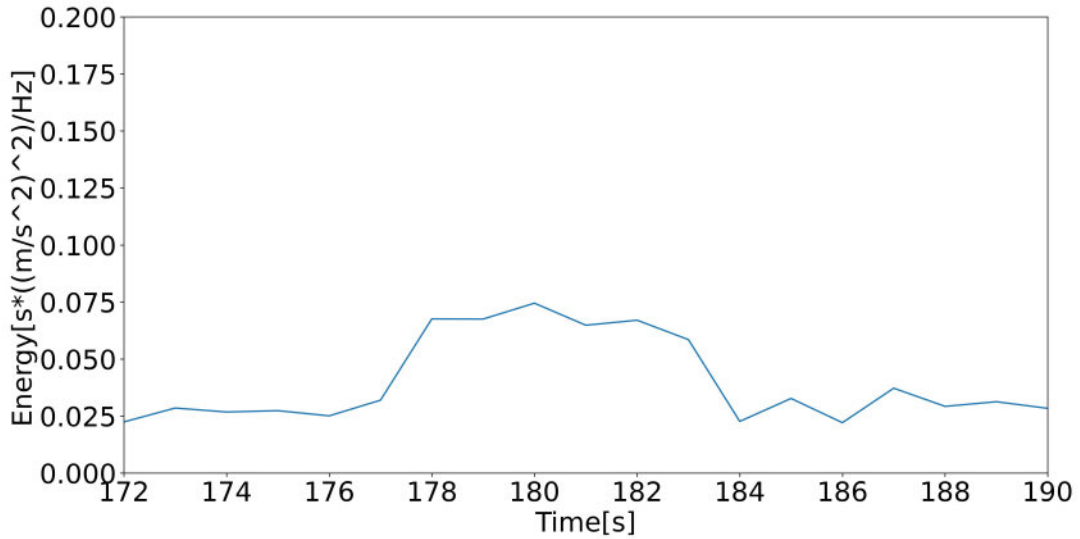
Figure 5.5.: Spectral energy per second from 172 seconds to 190 seconds for the cycle shown in figure 5.2 of the frequency bin from 930 to 1180 Hz

This is an example of how a classification model can be improved by choosing more suitable features.

Another aspect to take into account is that the vibration behavior differs depending on the traverse angle. To compare vibrations of the swivel joint for different conditions (e.g. different pressures or during aging of the swivel joint) and not to compare vibrations for different angles, short angle ranges showing similar vibration behavior must be defined. The angle ranges can be chosen arbitrarily but this would lead to a weaker accuracy

performance later on when the machine learning model is trained.

5.2. Procedure

In this section the code that was used for the calculations in the next chapter is explained. All code was written on python.

At first the code is explained, which calculates the STFT of the vibrations and plots the results in spectrograms. The spectrograms are used to compare the vibration behavior of different cycles. After this a machine learning model is presented to classify the vibrations of cycles at different conditions.

5.2.1. Spectrograms

Figure 5.6 shows the steps to plot the spectrograms of the cycles.
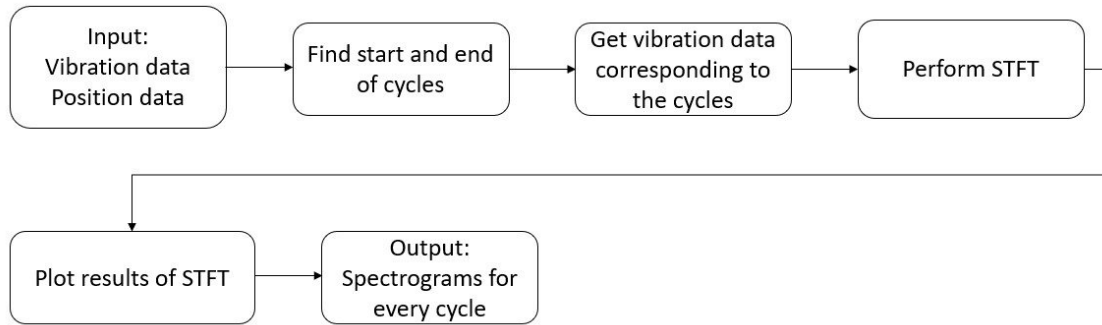
Figure 5.6.: Steps to plot spectrograms of cycles

The input includes the vibration data from the accelerometers described in the section 3.3.1 or 3.3.2 and the data from the SCADA. It contains the traverse angle over time. Figure 5.7 shows a plot of the position and vibration data. Using the traverse angle, the start and end positions of the cycles are found. This way the vibration during these cycles is extracted.

For the extracted vibration data the STFT is performed, which calculates the frequencies and their amplitudes over time. This information is then plotted in spectrograms. An example for a spectrogram is given in figure 5.8.

5.2.2. Spectrograms over traverse angle

The previous spectrograms show the frequencies over the cycling time and do not give any information about the traverse position, which is the main independent variable for this work. To allow a better comparison of spectrograms for different cycles, code to plot spectrograms over the traverse angle is necessary. The steps to do so are described in figure 5.9.

The first steps are similar to the previous ones. Vibration and position data are used to differentiate forth and back movements of the cycles before the STFT is performed. Movement forth means the traverse movement from the starting position to the end position,
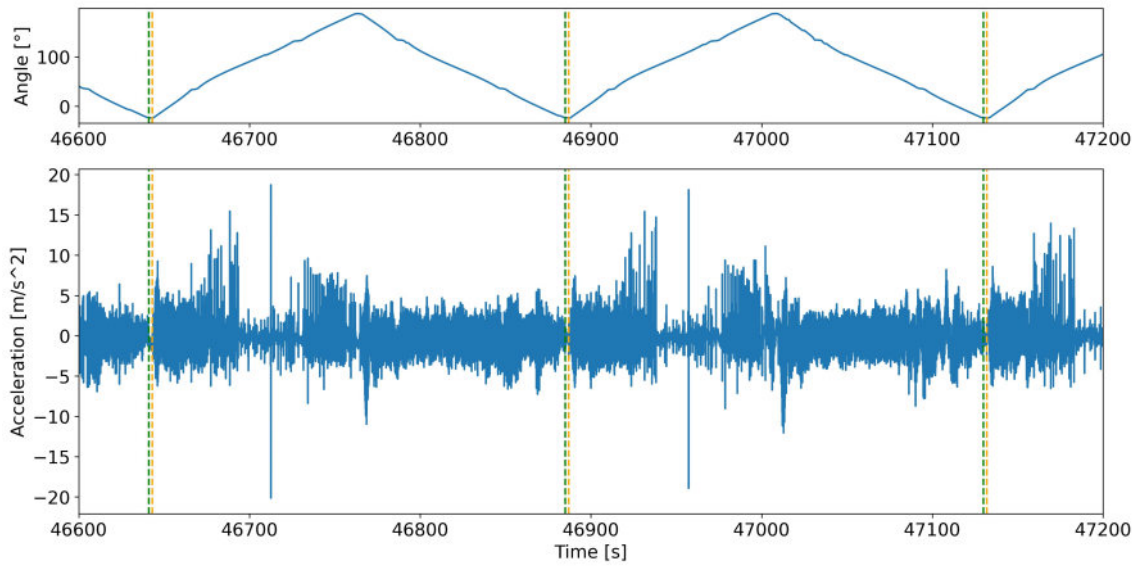
Figure 5.7.: Traverse angle (top) and vibration data (bottom) for a traverse cycle over time. Orange dashed lines show when a cycle starts and green dashed lines show when a cycle ends.
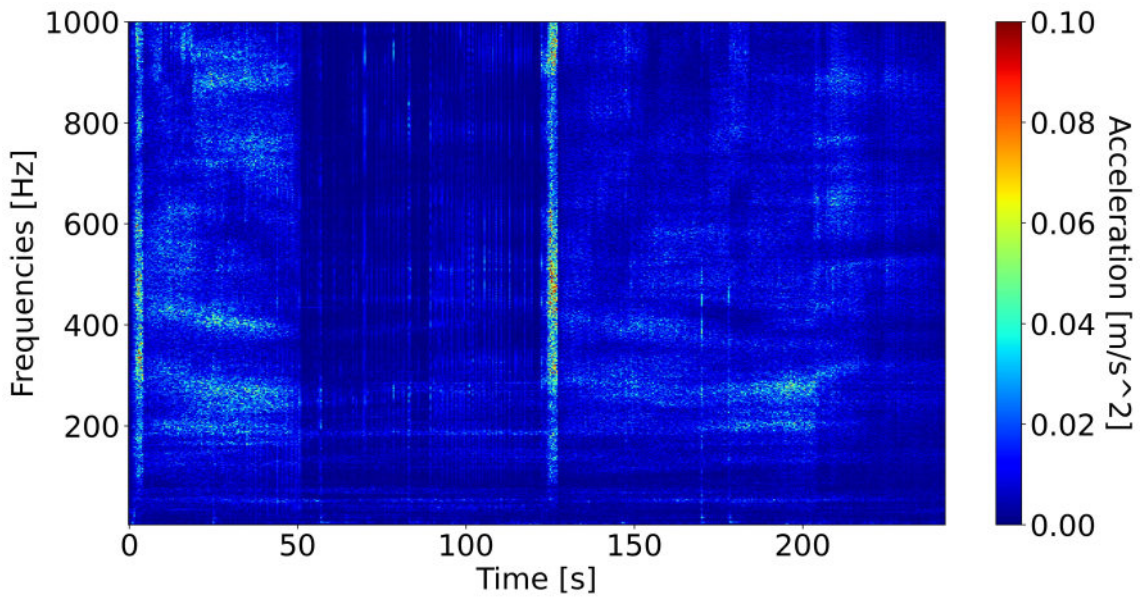
Figure 5.8.: Example of spectrogram showing the frequencies and amplitudes over time of a cycle
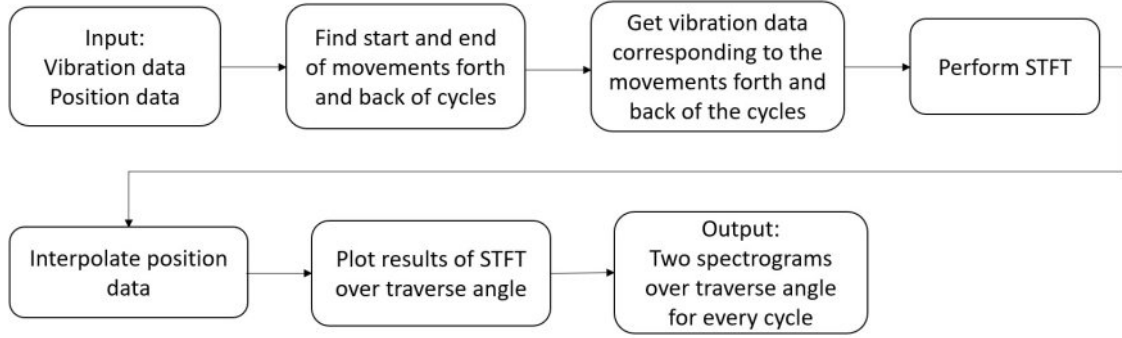
Figure 5.9.: Steps to plot spectrograms of cycles showing frequencies and their amplitudes over traverse angle

while movement back means the traverse movement from the end position towards the starting position. Figure 5.10 shows a plot of the position and vibration data, in which the start and end of the movement forth and back are marked.
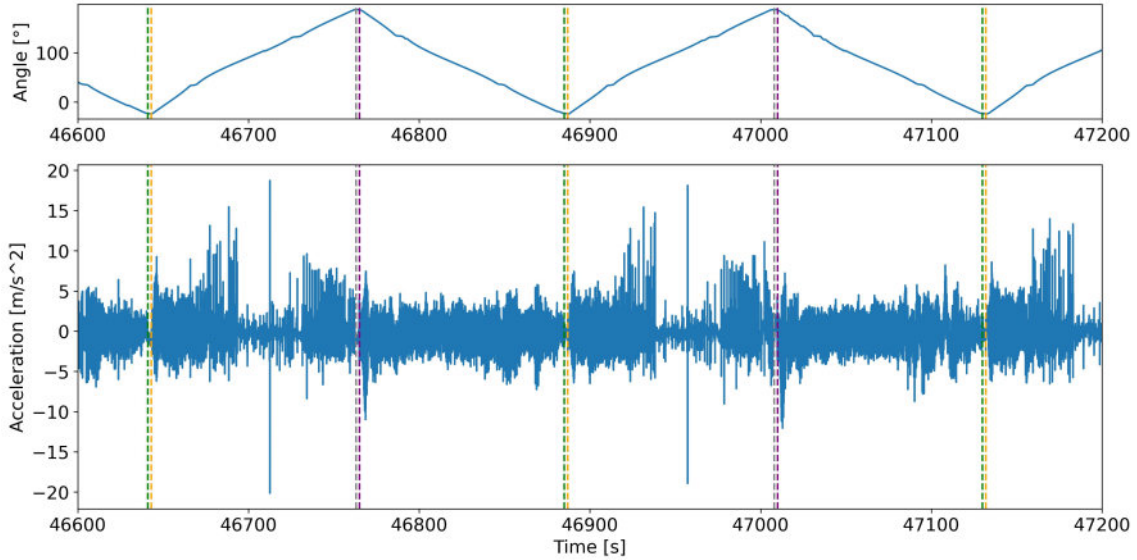
Figure 5.10.: Traverse angle (top) and vibration data (bottom) aligned. Orange dashed lines show when the traverse starts moving away from the starting position, grey dashed lines show when the traverse stops moving to the end position, purple dashed lines show when the traverse starts moving from the end position and green dashed lines show when the traverse stops moving to the starting position.

STFT is performed on these two fragments per cycle. To plot the results in spectrograms over the traverse angle, the traverse angle data has to be interpolated, so that it includes as many values as there are windows that were calculated with the STFT. For instance, if the sample rate of the traverse angle data is one second and the STFT calculates two Fourier Transforms per second, there are double as many windows as there are traverse angle values. To assign a traverse angle to every window, the traverse angle data has to be interpolated to add more traverse angle values matching the windows.

Afterwards the two spectrograms are plotted for the movements forth and back. Figure 5.11 shows an example of such spectrograms. Here the same cycle is represented as in figure 5.8 but now the angle information is clearly given.
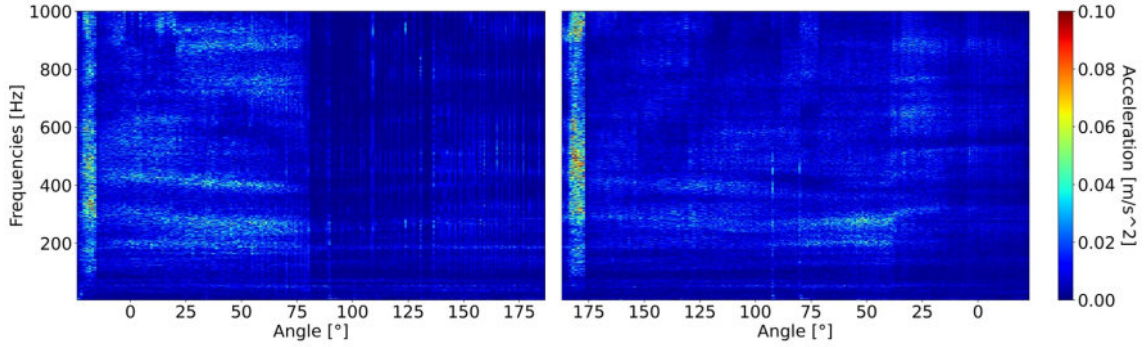
Figure 5.11.: Spectrograms over traverse angle for the movement from the starting position to the end position (left) and for the movement from the end position to the starting position (right)

5.2.3. Machine Learning Model

Spectrograms are useful to visualize vibration during traverse cycling and with enough know-how, conclusions can be drawn about the swivel joint's condition (e.g. HTF pressure or traverse cycling) by comparing them under different conditions. However, another approach to classify the swivel joint's condition is implemented using machine learning methods PCA and SVM, described in sections 4.2.1 and 4.3.2. This way a vibration measurement can be done and the machine learning model will draw out conclusions about the swivel joint without needing know-how on the user's part.

Figure 5.12 shows the structure of the model that classifies the vibration for different conditions. The model is divided into four steps: At first samples and their features are extracted from the vibration data. Then these samples are divided into angle ranges and subsets. The first division is done to compare vibrations in certain angle ranges. The latter division is done to do the n-fold cross validation. Then PCA is used to reduce the number of features to avoid overfitting in SVM.
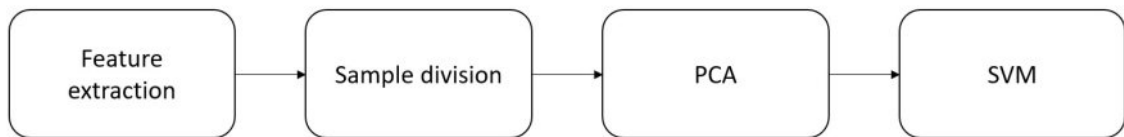
Figure 5.12.: Structure of the model using machine learning methods

Feature extraction

Figure 5.13 shows the steps used in feature extraction. The vibration data during cycling is divided into samples of a set length. They will be used in the further process of the machine

learning model. The length of the samples is arbitrary and an optimal length needs to be found. The longer a sample is, the more information it includes but the less samples there are to be used for the machine learning methods. If the samples are shorter, the more samples there are for the machine learning methods, which could improve the classification accuracy. However, if the samples are shorter they include less information, so multiple lengths have to be tried out. Then the features of the samples are calculated and saved to be used in later steps. Table 5.1 shows how the result of the feature extraction looks like. Statistical features as well as features calculated using frequency analysis presented in section 4.1 can be used here.
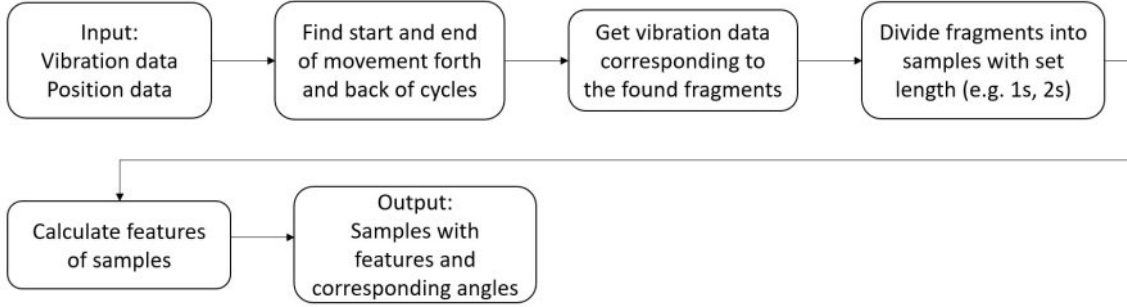
Figure 5.13.: Steps to extract features for the machine learning model

Table 5.1.: Representation of samples after feature extraction

Class	Angle	Forth or back	Statistical feature 1	...	Frequency feature 1	...
$class_1$	-19.9474	forth	statistical feature$_{11}$	...	frequency feature$_{11}$	...
$class_1$	-17.5377	forth	statistical feature$_{21}$	...	frequency feature$_{21}$	...
...	...	...	...	...	...	...

Sample division into angle ranges and folds

The samples are divided into different angle ranges. Appropriate angle ranges are selected after analyzing the spectrograms. The output is the samples with their features and corresponding angle ranges. Table 5.2 shows how the samples look like after the division into angle ranges. After this the samples are divided into subsets that will build the folds dividing the subsets into a training data set and a testing data set as shown in section 4.3.1. The next steps, PCA and SVM, are done for every angle range separately and for every fold of subsets.

Table 5.2.: Representation of samples after sample division into angle ranges

Class	Angle range	Forth or back	Statistical feature 1	...	Frequency feature 1	...
$class_1$	(-20°)-20°	forth	statistical feature$_{11}$	...	frequency feature$_{11}$	...
$class_1$	(-20°)-20°	forth	statistical feature$_{21}$	...	frequency feature$_{21}$	...
...	...	...	...	...	...	...
$class_1$	20°-60°	forth	statistical feature$_{21}$	...	frequency feature$_{21}$	...
...	...	...	...	...	...	...

Principal Component Analysis (PCA)

Once the samples have been prepared, PCA can be implemented. Figure 5.14 shows the steps to get the results from the PCA.
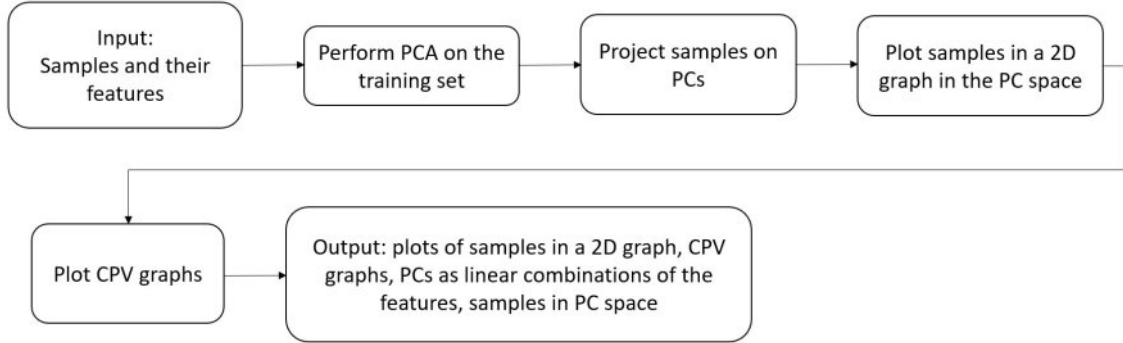
Figure 5.14.: Steps to perform PCA

Only the training set is used to calculate the principal components. Afterwards the samples from the training and the testing set are projected onto the principal components. The samples are plotted in a 2D graph using the first two principal components to visualize the results. In some cases, clustering can be already seen in these graphs. Figure 5.15 shows an example of such a graph, in which the training and testing sets are represented using different shapes. In this case, samples were used with 18 features.
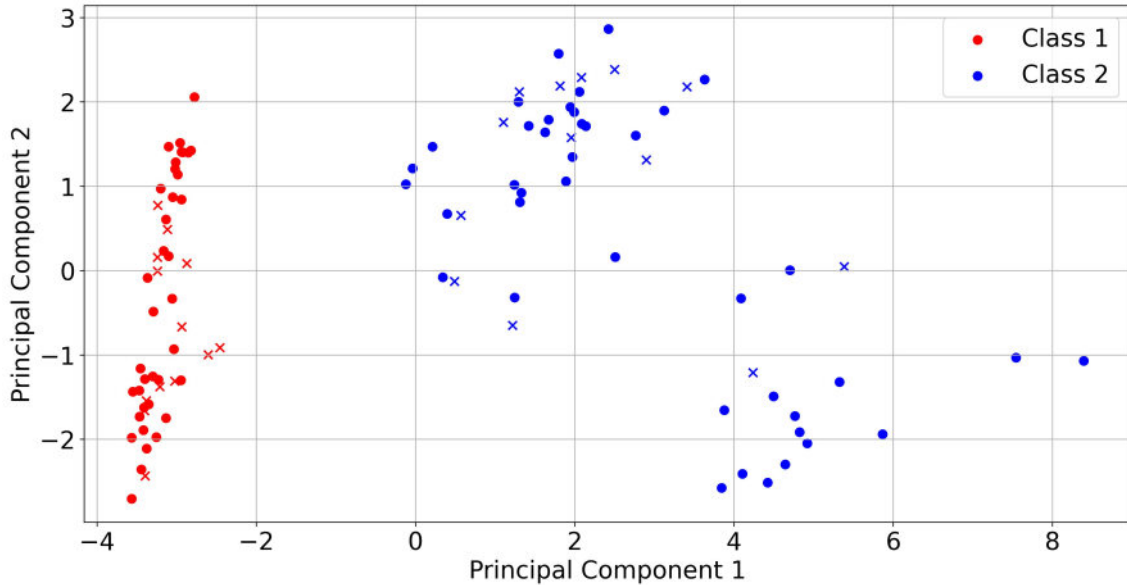
Figure 5.15.: Example of a 2D Graph using two principal components. Training set is represented with circles and the testing set is represented with crosses.

Cumulative percent variance (CPV) graphs are also plotted to check how many principal components should be used for the SVM algorithm. An example of a CPV graph is given in figure 5.16, corresponding to the same example given in figure 5.15. Looking at this

graph, one might decide to use 4-6 principal components for the SVM depending on how much variance is desired to be included in the data used for the SVM. For example, using 4 principal components would include more than 92 % of variance.
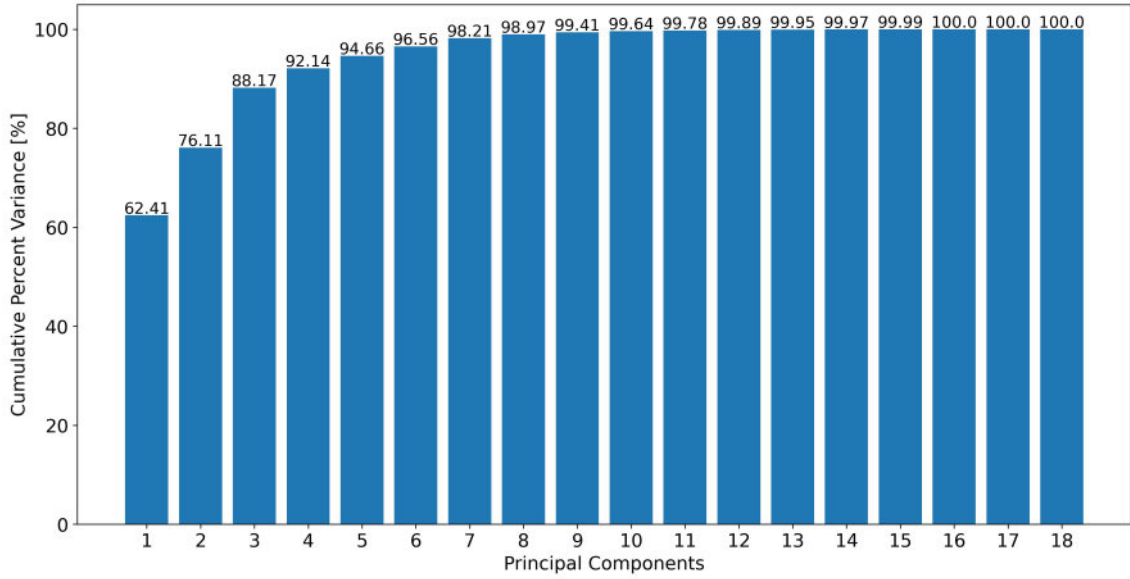
Figure 5.16.: Example of a graph showing the cumulative percent variance (CPV) depending on the number of principal components (PCs)

The principal components are saved as linear combinations of the features to see which features vary the most.

Support Vector Machine (SVM)

SVM is finally used as a soft margin classifier to separate the extracted samples. The steps involved are shown in figure 5.17.
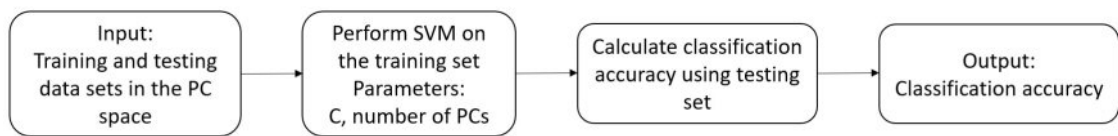
Figure 5.17.: Steps to perform SVM

The SVM algorithm is performed on the training set projected onto the principal components calculated by the PCA. The number of principal components to be used is decided after evaluating the CPV graph. Another parameter that needs to be set is the parameter C that controls the soft margin, as shown in section 4.3.2. In this case, multiple values have to be tried out to find an optimal value. After the hyperplane, separating the samples of different classes, was found, the testing set is used to calculate a classification accuracy. It is used to determine how the parameters, which can be set in the machine learning model, affect the classification performance.

6. Results

6.1. Classification of cycles at different pressures

Cycles at different pressures were performed to better understanding the behavior of the swivel joint and its vibrations, and test the pertinent methods found during the literature research. Two cycles were performed at 0 bar, 10 bar, 20 bar, 30 bar and 35 bar, at ambient temperature. The starting position was set to -20° and the end position was set to 180°. To reduce external variables, translation movement was not considered during the cycles. Sensors KS95B.100 and their associated setup were used. The positions of the accelerometers can be seen in figure 3.13. In this section the sensors are referred to as followed:

- Sensor 1: accelerometer that was screwed to the east swivel joint perpendicular to the REPA

- Sensor 2: accelerometer that was screwed to the west swivel joint perpendicular to the REPA

- Sensor 3: accelerometer that was screwed to the west swivel joint in the opposite direction of the REPA

The following figures (6.1, 6.2, 6.3, 6.4, 6.5) show, for each pressure, the frequencies and their amplitudes of the swivel joint's vibration over the traverse angle. The results were calculated using the measurements of sensor 3. For better visualization, the spectrograms frequency range is set to 500 Hz.
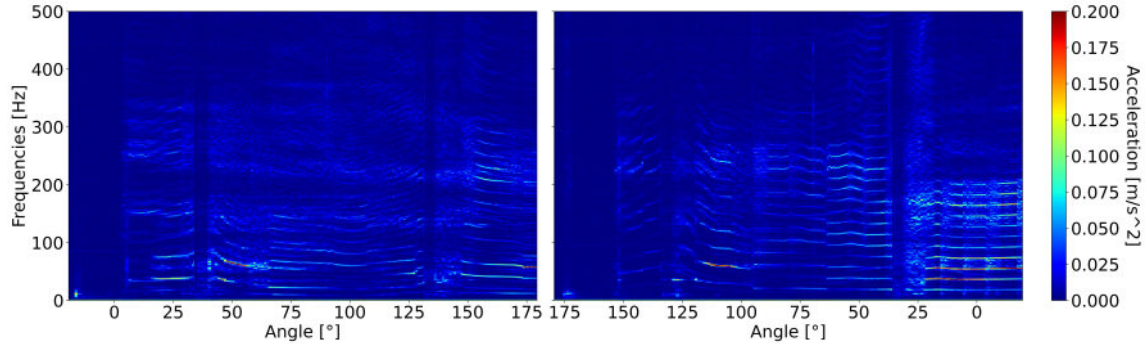
Figure 6.1.: Spectrogram for a cycle at 0 bar showing the frequencies and their amplitudes over the traverse angle.

The vibration behavior changes for higher pressures. For 0 bar, multiple peak acceleration frequencies can be observed, but this changes the higher the pressure is set. For 35 bar, no clear main frequencies can be distinguished. Increasing the pressure, peak energy changes from well-defined and segregated on certain frequencies to blurrier and scattered to other frequencies.

The comparison of different cycle's spectrograms is complex even if differences can be seen. To simplify the comparison the power of vibration is looked at. Figures 6.6, 6.7 and 6.8
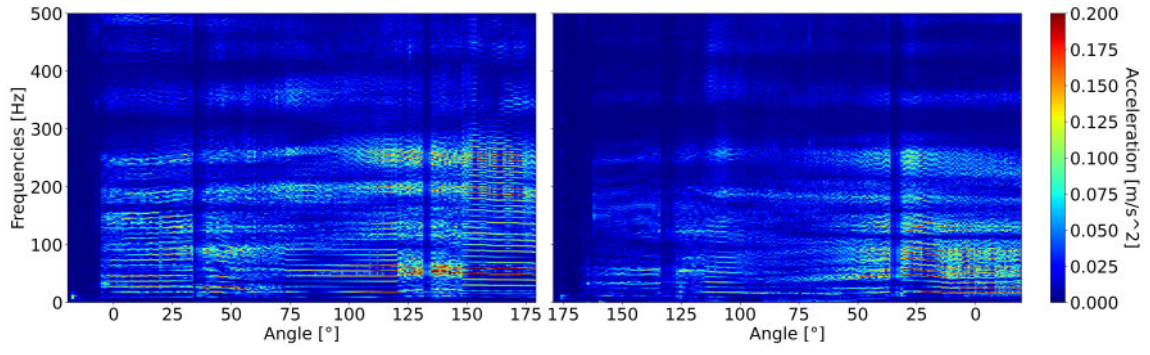
Figure 6.2.: Spectrogram for a cycle at 10 bar showing the frequencies and their amplitudes over the traverse angle.
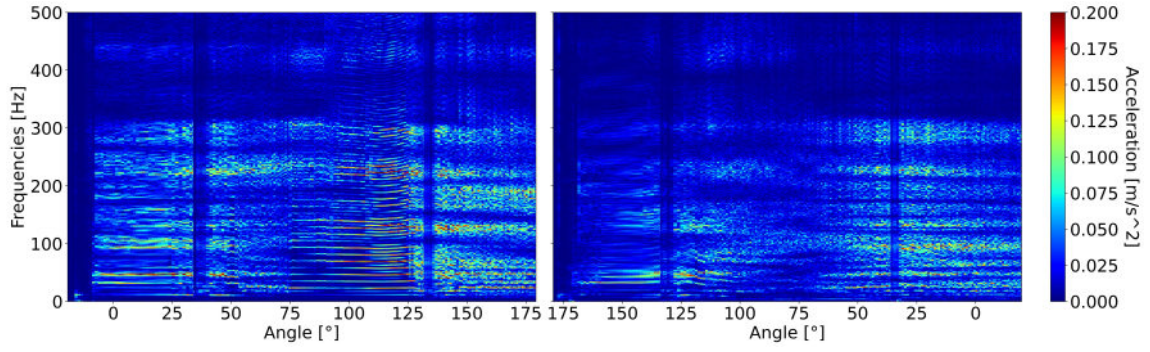
Figure 6.3.: Spectrogram for a cycle at 20 bar showing the frequencies and their amplitudes over the traverse angle.
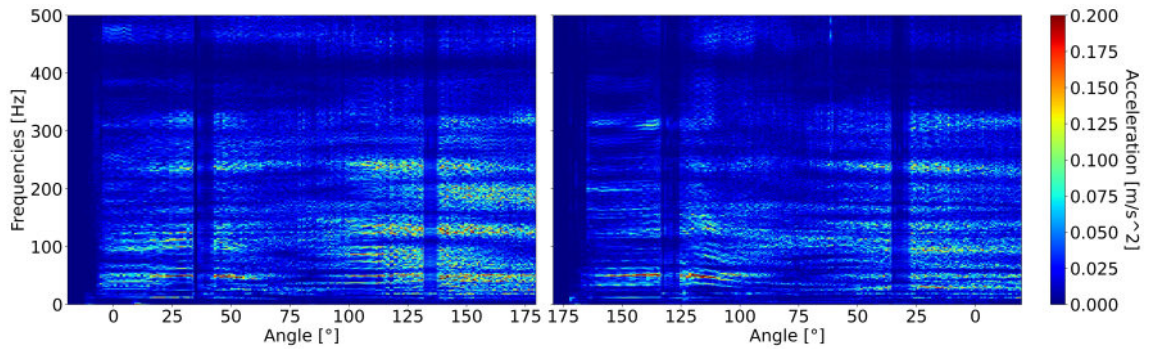
Figure 6.4.: Spectrogram for a cycle at 30 bar showing the frequencies and their amplitudes over the traverse angle.
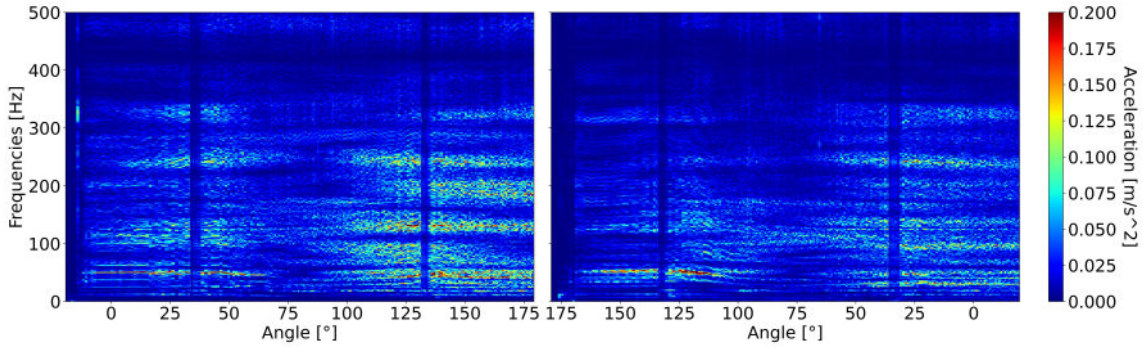
Figure 6.5.: Spectrogram for a cycle at 35 bar showing the frequencies and their amplitudes over the traverse angle.

show the mean power of the vibration of the whole cycle and the power of the vibration for specific angles for the three sensors. Even though sensor 1 and sensor 2 are on the same position of the different swivel joints, the power of the measured vibrations of sensor 1 is more than ten times higher than that of sensor 2. One reason to explain this is that there might have been still some crystallized HTF left in the east swivel joint. For the sensors 1 and 2, the mean power over the whole cycle is the highest at 20 bar and gets lower for higher pressures. For sensor 3, the mean power over the whole cycle is the highest at 10 bar and gets lower for higher pressures. As the vibration behavior does not remain the same over the traverse cycle, the vibration power at certain angles (20°, 90° and 160°) is looked at. However, for these angles there is no clear trend for the power. The power at different angles does not behave like the mean power. For example, for sensor 3 the mean power at 10 bar is slightly higher than at 20 bar but the power at 20° is lower at 10 bar than at 20 bar. A clear correlation between the HTF pressure and the vibration power was not found. Therefore, more cycles at different HTF pressures would be needed to make clearer statements.

In the following, the machine learning model described in subsection 5.2.3 is used to classify the cycles according to pressure and to try out different values for parameters that can be chosen. The features used in the model include statistical features, as well as features that can be calculated using frequency analysis. The statistical features include signal range, mean value, variance, standard deviation, skewness, kurtosis and crest factor. To calculate features using frequency analysis, the frequency domain is divided into 10 equally wide frequency bins from 0 Hz to 2000 Hz. The features calculated using frequency analysis include the spectral energy and the ratios of spectral energy of each bin to the sum of spectral energy of the frequency bins. In total, 18 features are extracted per sample. The vibration signal of the cycles is divided into samples with the length of one second and two seconds to test which length is going to lead to better classification accuracy. The samples are divided into the following angle ranges:

- Movement from the starting position to the end position: 0°-31°, 36°-62°, 62°-100°, 100°-128°, 135°-155°, 155°-178°

- Movement from the end position to the starting position: 160°-137°, 132°-110, 100°-
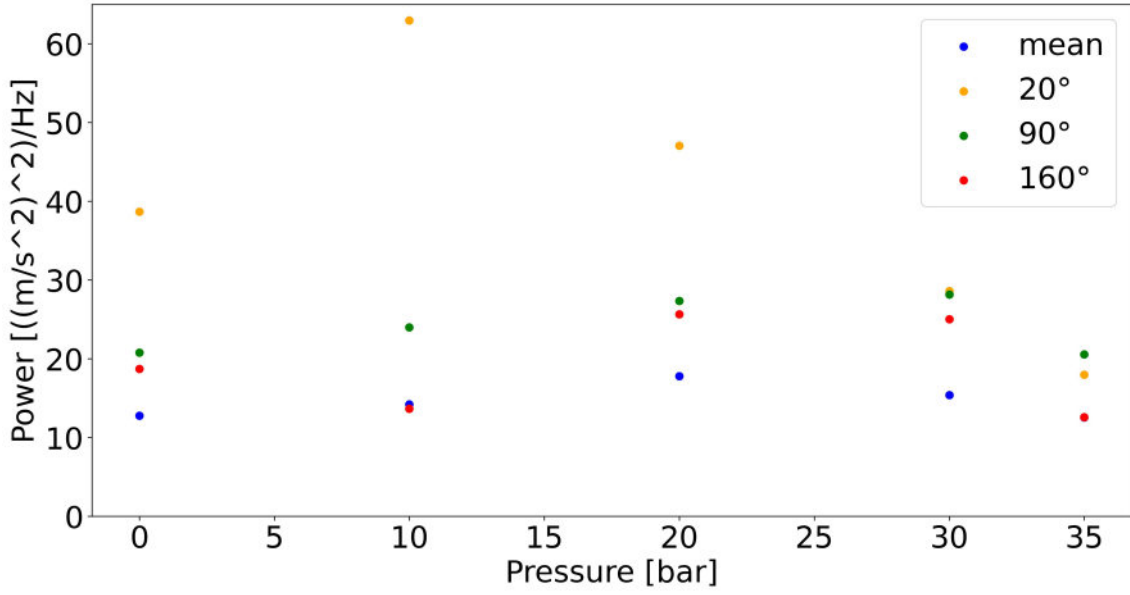
Figure 6.6.: Mean power and power of vibration for the angles 20°, 90°, 160° of the vibration measured by sensor 1 for different pressures
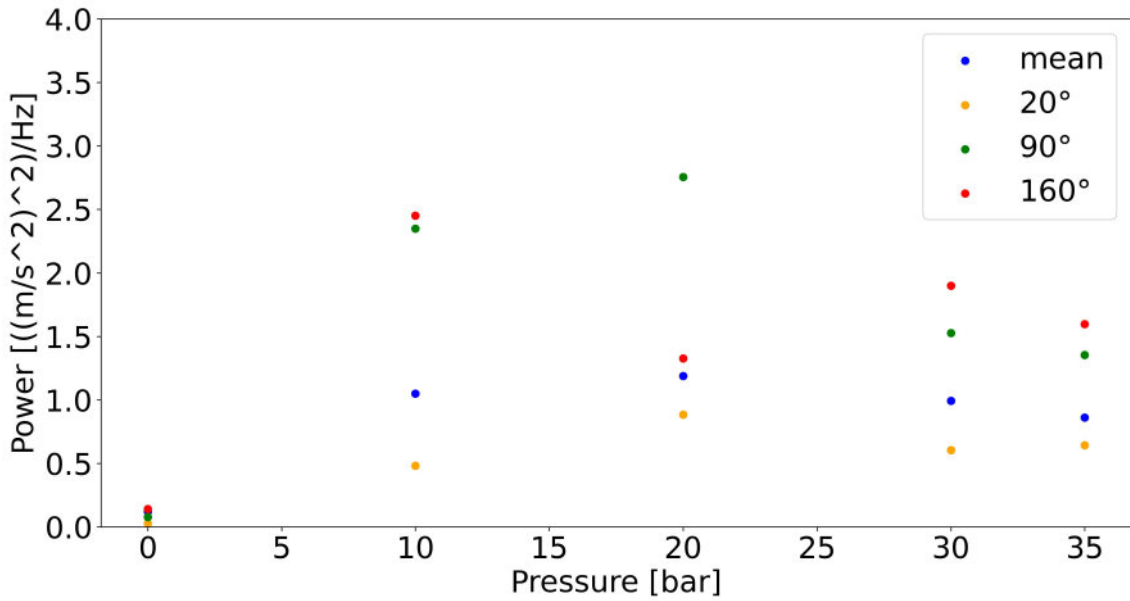
Figure 6.7.: Mean power and power of vibration for the angles 20°, 90°, 160° of the vibration measured by sensor 2 for different pressures
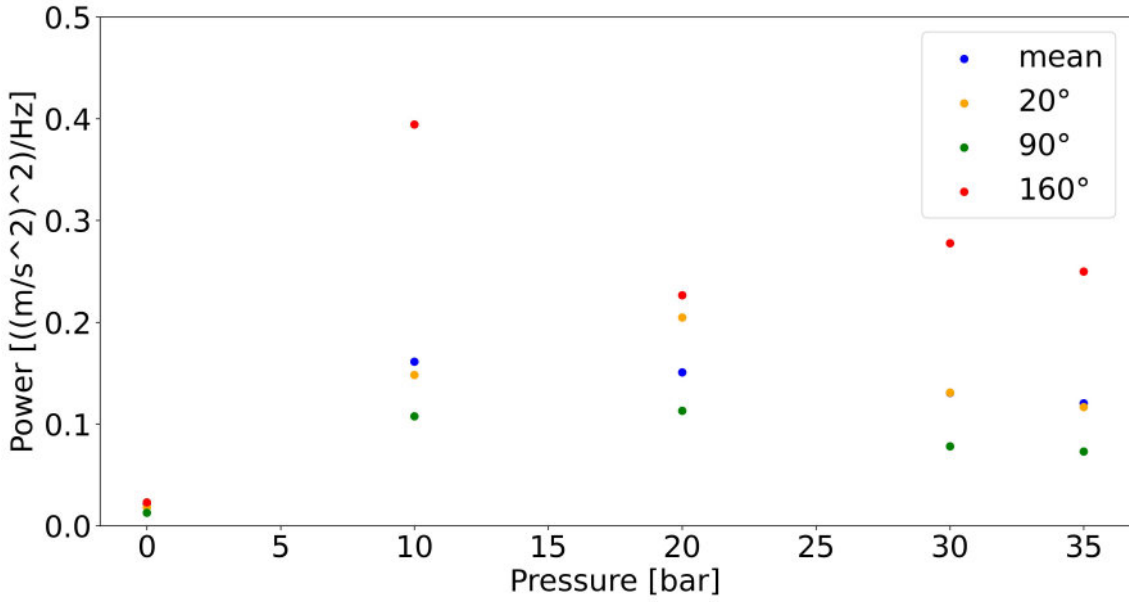
Figure 6.8.: Mean power and power of vibration for the angles 20°, 90°, 160° of the vibration measured by sensor 3 for different pressures

40°, 25°-(-15)°

These angle ranges were selected after analyzing the spectrograms, because it was found that the vibration behavior in these angle ranges is continuous and homogeneous.

The samples are divided into four equally large subsets. The model is trained four times, in which every time another fold is used as shown in section 4.3. PCA is performed after the samples are prepared. At first results are shown for samples of the vibrations measured with sensor 3 with the length of one second. Figures 6.9 and 6.10 show the samples projected onto the principal components. Already with only two principal components, some sample clustering is observed, e.g. 0 bar samples can linearly be separated from the other samples.

The CPV graphs reveal that 8 PCs include from 94 % - 98 % of variance depending on the sensor and the angle range. Figure 6.11 shows a CPV graph for the PCs calculated for sensor 3 in the angle range of 0° to 31° (forth).

SVM is applied after the samples are projected onto the PCs. To decide which value to set for parameter C, SVM is performed using different values for C. The calculations are done using 8 PCs and for the sample length of one second. The results are shown in the appendix in table B.1. In 16 cases, $C = 10$ gives the best result, in 18 cases, $C = 100$ gives the best result and in 15 cases, $C = 1000$ gives the best result. Therefore, there is no obvious choice for the parameter C. However, for the following calculations the parameter $C = 100$ is chosen.

SVM was performed on the samples trying out different numbers of PCs. The accuracies are shown in table B.2 in the appendix. In 5 cases, an accuracy above 95 % is reached. An optimal number of PCs is not obvious, as in some cases overfitting is happening when

Figure 6.9.: Samples from the vibration measured with sensor 3 for the angle range from 0° to 31° (forth) projected onto the first two principal components
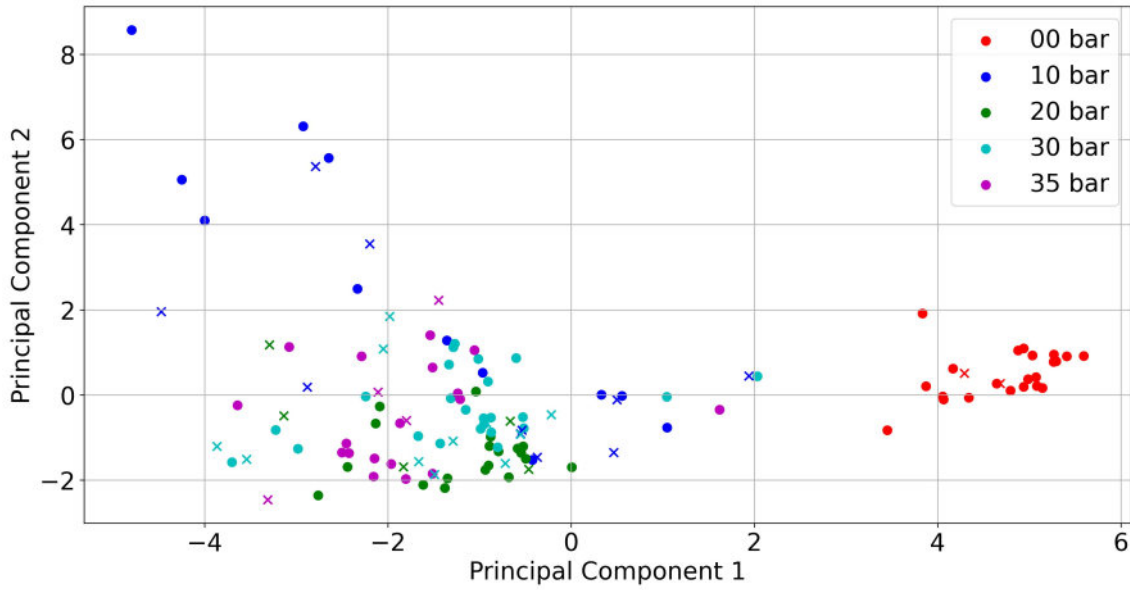
Figure 6.10.: Samples from the vibration measured with sensor 3 for the angle range from 36° to 62° (forth) projected onto the first two principal components
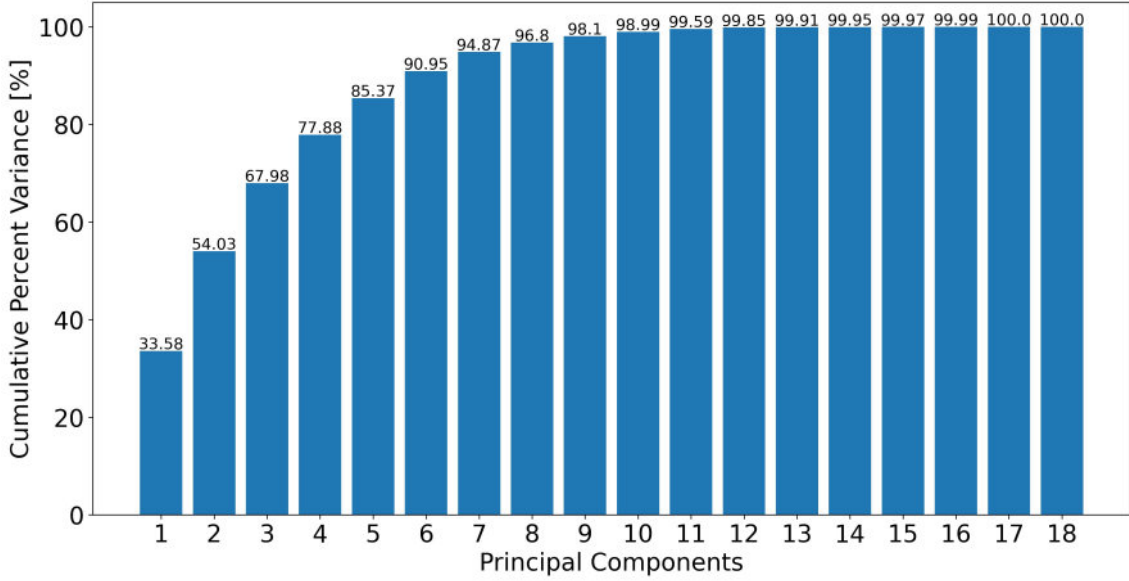
Figure 6.11.: CPV graph for the PCs calculated for sensor 3 in the angle range of 0° to 31° (forth)

too many PCs are used, e.g. for sensor 2, in the angle range from 100° to 128° (forth), the highest accuracy is achieved when 16 PCs are used instead of 18.

The same calculations were done for samples with the length of two seconds. The results are shown in table B.2 (appendix). In 3 cases, an accuracy above 95 % is achieved. Overfitting is also happening in some cases here. In general, using samples with the length of two seconds decreases the classification accuracy, however there are exceptions.

The results show that there is no optimal set of parameters that can be selected. Depending on the location of the sensor and the angle range, multiple values for the sample length, number of PCs and parameter C must be tried out. However, it is shown that the machine learning model presented is a promising approach to determine the swivel joint's condition.

6.2. Classification of cycles over aging process

10,000 cycles were performed with HTF at 393°C and 35 bar for the aging test of the REPAs. The starting position was set to -23.5° and the end position was set to 187°. Translation movement was also included and went from -4.74° to 14.24° and back during the cycle movement. At first, the sensors KS95B.100 were used until the 3900th cycle, and then they were exchanged for the sensors 320C52. In this section, only the data measured by the sensors 320C52 is considered, because the sensors KS95B.100 were found to be unsuitable for the temperatures reached during the test at the measurement area (see section 3.3.4). The positions of the accelerometers can be seen in figure 3.17. In this section, the sensors are referred to as followed:

- Sensor 1: accelerometer that was screwed to the east swivel joint perpendicular to the REPA

- Sensor 2: acclerometer that was screwed to the east swivel joint in the opposite direction of the REPA

- Sensor 3: accelerometer that was screwed to the west swivel joint perpendicular to the REPA

- Sensor 4: accelerometer that was screwed to the west swivel joint in the opposite direction of the REPA

The same procedure as in the previous section 6.1 is applied to compare the vibration behavior of the 4000th cycle, 7000th cycle and 10,000th cycle. The following figures (6.12, 6.13, 6.14, 6.15, 6.16, 6.17) show the spectrograms of the cycles (forth and back) measured by sensor 1 and sensor 2, i.e. the sensors on the east swivel joint. The spectrograms show the frequencies and their amplitudes of the vibration up to 2000 Hz.
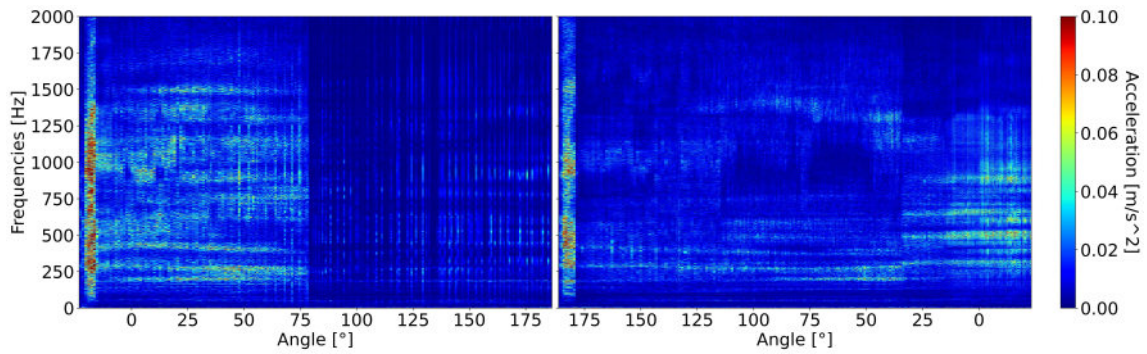
Figure 6.12.: Spectrogram of the 4000th cycle showing the frequencies and their amplitudes of the vibrations that were measured with sensor 1 (perpendicular to the REPA) over the traverse angle.
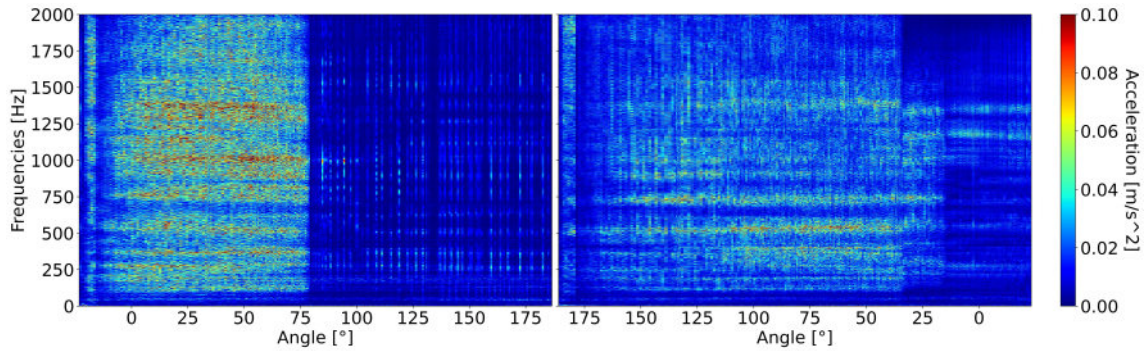
Figure 6.13.: Spectrogram of the 4000th cycle showing the frequencies and their amplitudes of the vibrations that were measured with sensor 2 (in opposite direction of the REPA) over the traverse angle.

The vibration behaviors for the different cycles have many similarities, although clear differences can be seen. A short overview of the vibration behavior of the 4000th cycle is given, and then the vibration behaviors of the 7000th and 10,000th cycles are compared with it.
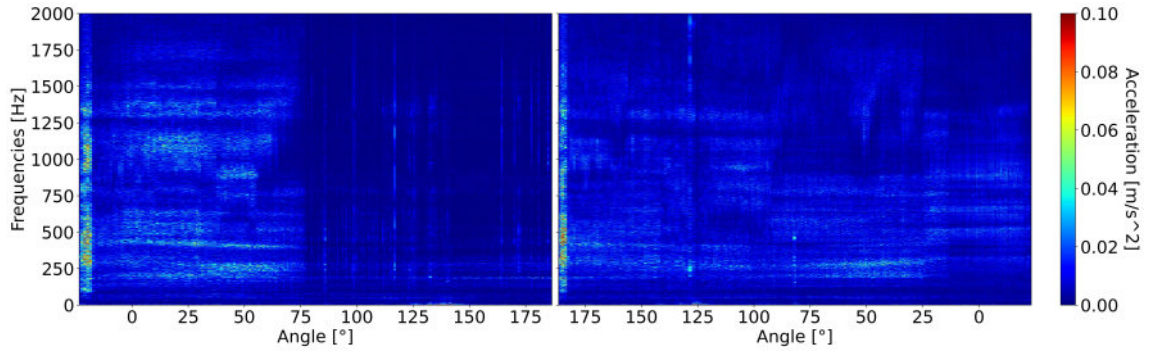
Figure 6.14.: Spectrogram of the 7000th cycle showing the frequencies and their amplitudes of the vibrations that were measured with sensor 1 over the traverse angle.
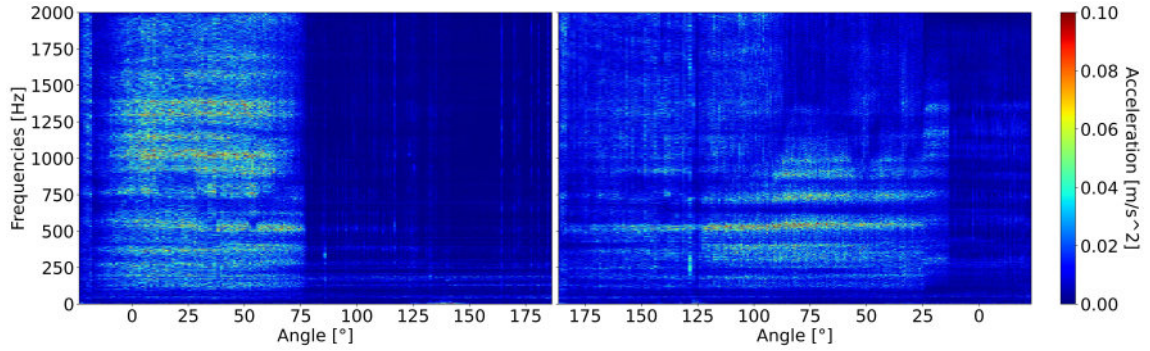
Figure 6.15.: Spectrogram of the 7000th cycle showing the frequencies and their amplitudes of the vibrations that were measured with sensor 2 over the traverse angle.
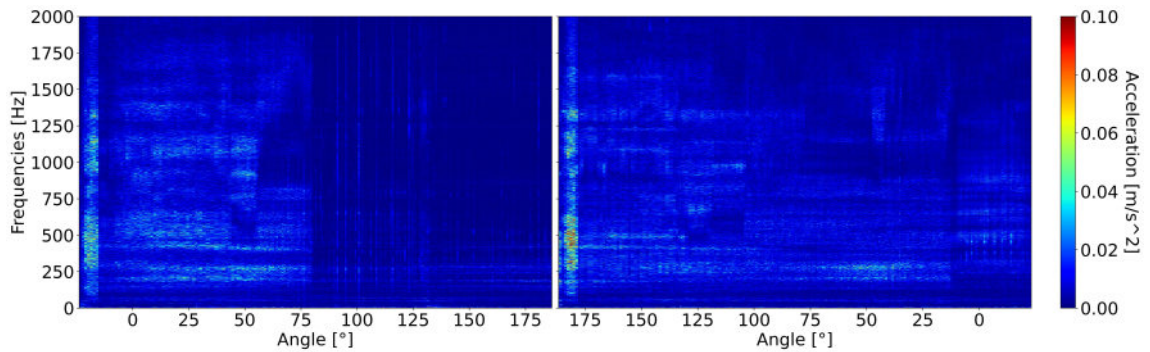
Figure 6.16.: Spectrogram of the 10,000th cycle showing the frequencies and their amplitudes of the vibrations that were measured with sensor 1 over the traverse angle.
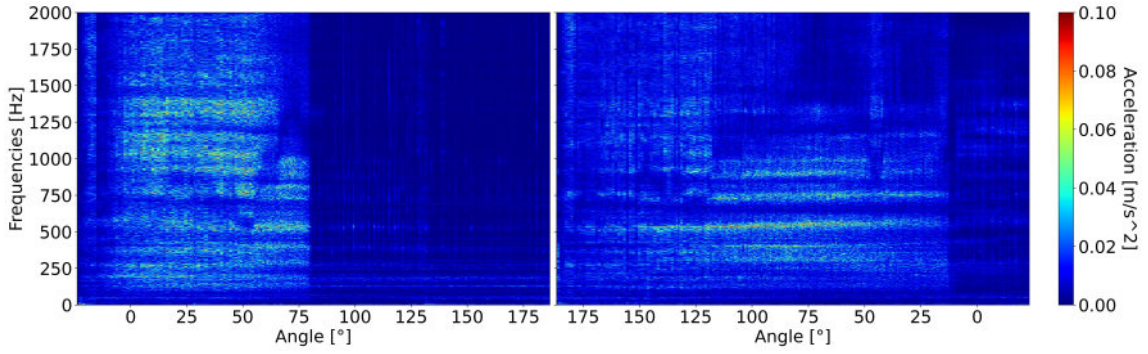
Figure 6.17.: Spectrogram of the 10,000th cycle showing the frequencies and their amplitudes of the vibrations that were measured with sensor 2 over the traverse angle.

When the traverse starts moving either from the starting position or from the end position, the vibration includes the highest power. Until 78° (forth) the vibration includes multiple frequency bins with higher power, while the vibration in REPA direction is more continuous and homogeneous than the vibration perpendicular to the REPA. From 78° (forth) to the end position, the power of the vibration gets reduced drastically and every few angles high energy appears over the frequency bin from 0 Hz to 2000 Hz. On the rotation back to the starting position similar frequency bins are included in the vibration.

Along the 7000th cycle, the vibrations have significantly less power than the vibrations in the 4000th cycle. For some angle ranges, some frequencies disappear in the 7000th cycle, e.g. in the angle range from 56° to 78° (forth) the frequencies from 800 Hz to 1300 Hz disappear in the vibration perpendicular to the REPA. Also, in the angle range from 78° (forth) to the end position the number of angles in which high energy appears gets reduced.

Along the 10,000th cycle the vibrations have slightly less power than along the 7000th cycle. In fact, in a few angle ranges some frequencies disappear, e.g. in the angle range from 61° to 78° (forth) the frequencies from 1000 Hz to 1100 Hz disappear earlier in the vibration in the REPA direction.

Similar changes of the vibration behavior can be seen for the data measured by the other two sensors on the west swivel joint. The corresponding spectrograms are included in the appendix in figures A.1, A.2, A.3, A.4, A.5 and A.6. Consequently, the vibration is a suitable parameter to distinguish cycles at different stages of the aging process, corroborated by the clear differences in their vibration behavior.

In the following figures (6.18, 6.19, 6.20 and 6.21), the mean power of vibration over kinematic unit cycle number is shown. The power for specific traverse angles is also given. The mean power is the highest at the 4000th cycle, decreases at the 5000th cycle, increases at the 6000th cycle and then decreases again and settles around a certain value for the other given cycles until the 10,000th cycle. Unlike the mean power, the power at some traverse angles does not follow the same pattern. Since a clear trend can not be seen, a first approach with machine learning is tried as follows.
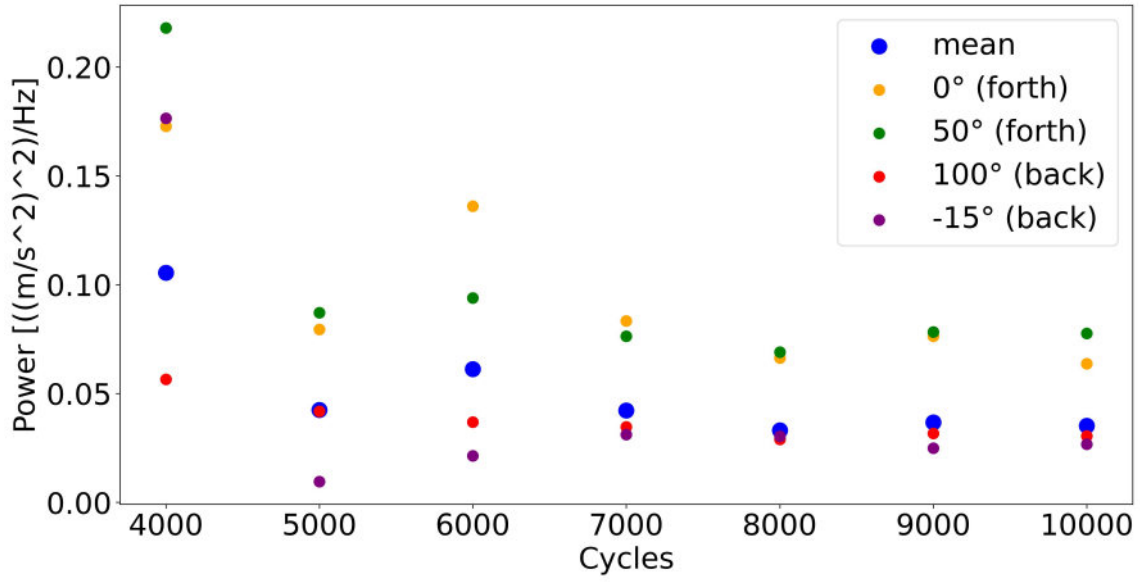
Figure 6.18.: Power of vibration measured by sensor 1 over kinematic unit cycle number for specific traverse angles, and the mean value for the specified cycle.
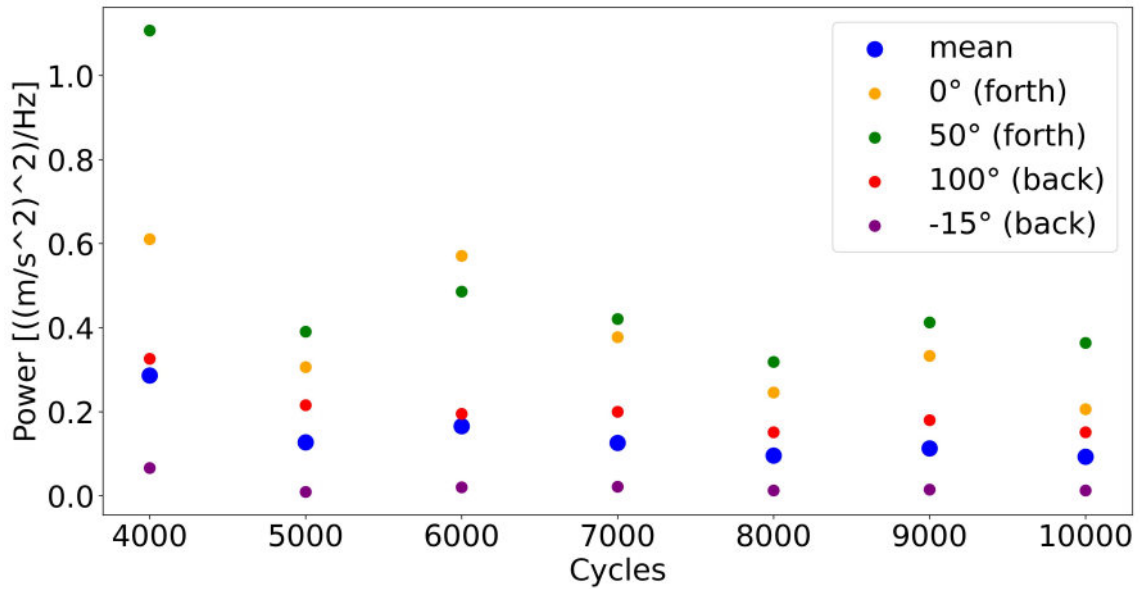
Figure 6.19.: Power of vibration measured by sensor 2 over kinematic unit cycle number for specific traverse angles, and the mean value for the specified cycle.
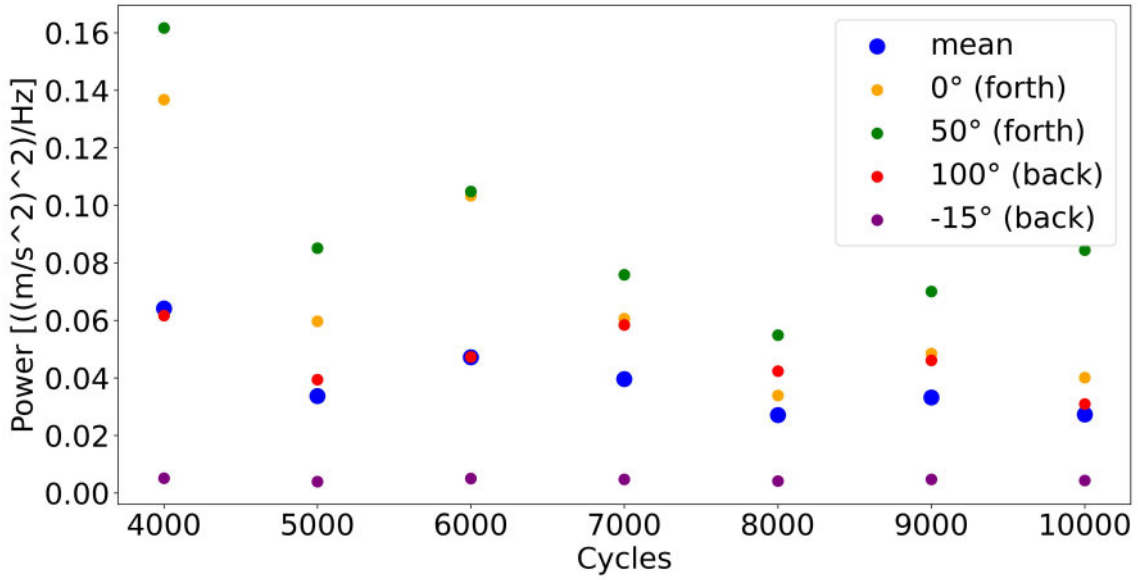
Figure 6.20.: Power of vibration measured by sensor 3 over kinematic unit cycle number for specific traverse angles, and the mean value for the specified cycle.
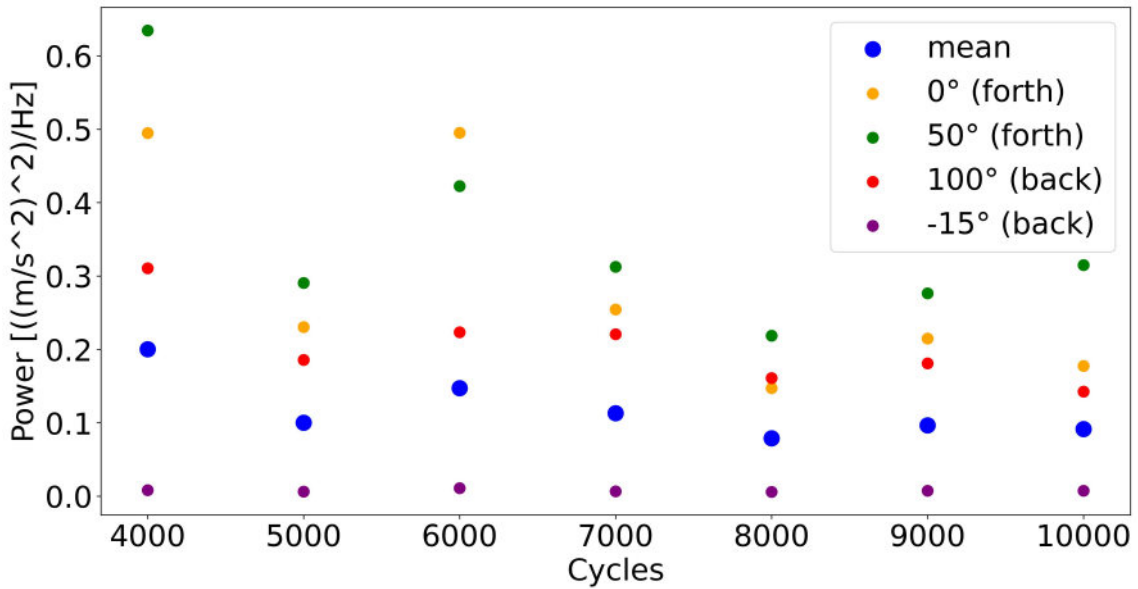
Figure 6.21.: Power of vibration measured by sensor 4 over kinematic unit cycle number for specific traverse angles, and the mean value for the specified cycle.

The machine learning model described in subsection 5.2.3 is used to classify the vibration behavior for the following categories:

- Once 4000 cycles were performed

- Once 7000 cycles were performed

- Once 10,000 cycle were performed

To increase the number of samples, 20 cycles are used for every category. This is a viable approach, as the vibration behavior remains similar in the span of 20 cycles. In figure 6.22, spectrograms for the 4000th cycle and for the 4020th cycle are shown, in which the same frequency bins are included in the vibration. Therefore, the samples are extracted from the 4000th to 4020th cycles, from the 7000th to 7020th cycles and from the 9980th to 10,000th cycle.
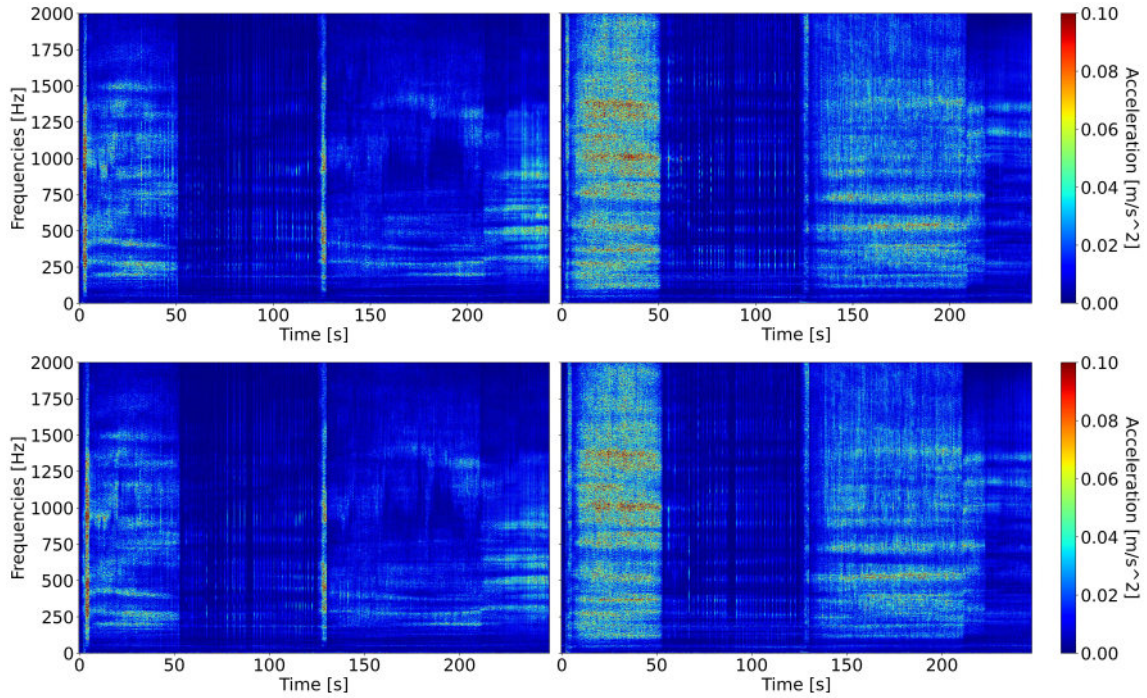
Figure 6.22.: Spectrograms of the 4000th cycle (top, sensor 1 left, sensor 2 right) and spectrograms of the 4020th cycle (bottom, sensor 1 left, sensor 2 right)

The same process is being followed as in the previous section 6.1. The vibration signal of the cycles is divided into samples with the length of one second and two seconds. The samples are then divided into the following selected angle ranges:

- Movement from the starting position to the end position: $(-21)°-(-14)°$, $(-14)°-(-3)°$, $(-1)°-11°$, $11°-20°$, $20°-32°$, $35°-79°$, $79°-131°$, $133°-187°$

- Movement from the end position to the starting position: $185°-179°$, $170°-155°$, $155°-135°$, $135°-115°$, $115°-105°$, $105°-79°$, $76°-47°$, $47°-36°$, $34°-14°$, $14°-0°$, $0°-(-23.5)°$

At first, PCA is used. In some cases, depending on the sensor position and angle range, two PCs are already enough to see sample clustering. Figure 6.23 shows the samples in the

angle range from 115° to 105° (back) that were measured with sensor 3, in which clustering can be clearly observed.
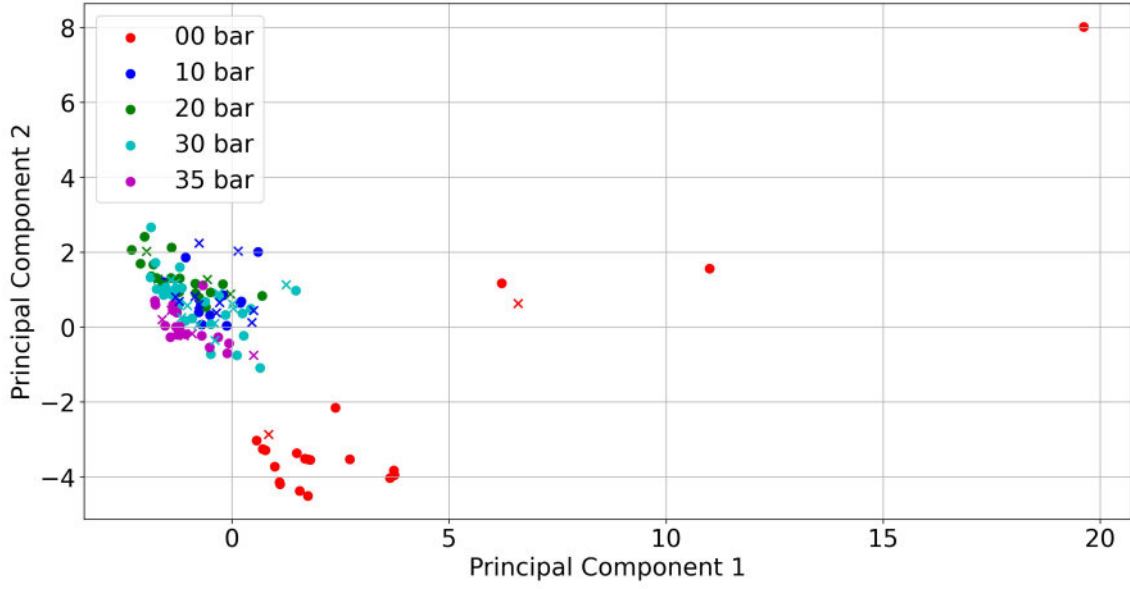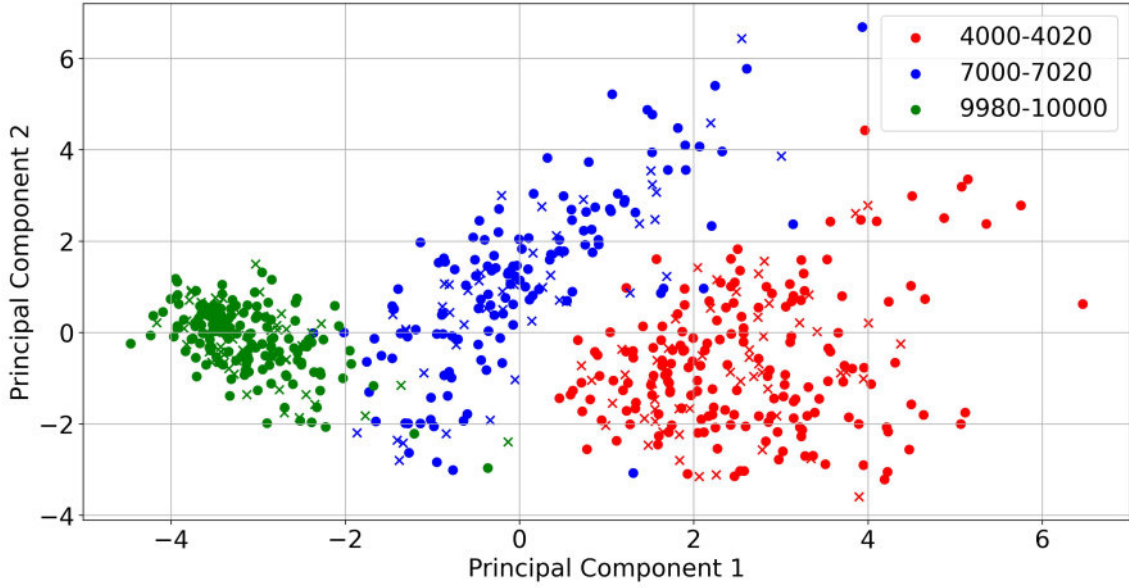

Figure 6.23.: Samples from the vibration measured with sensor 3 for the angle range from 115° to 105° (back) projected onto the first two principal components

Using $C = 100$, SVM was performed on the samples trying out different numbers of PCs. The accuracies for every case are calculated by averaging the accuracies of the four models that were trained using different folds as shown in 4.3.1.

Figure 6.24 explains the whole machine learning process. It is executed two times, i.e. once with the sample length of one second and once with the sample length of two seconds, in order to study the influence of the sample length.

The accuracies for the models that use samples with the length of one second are given in the tables 6.1 and 6.2. Out of 76 calculated cases (4 sensors times 19 angle ranges), in 44 cases the model achieves an accuracy above 95 % and in one case it even achieves an accuracy of 100 %. The worst performing angle ranges are the ones from 79° to 131° (forth) and 133° to 187° (forth). These are the angle ranges with low power vibrations and short surges of energy over all the frequencies. The best accuracy is achieved for sensor 3 and the angle range from -14° to -3° (back). Models that use vibrations measured by sensors 1, 2 and 3 perform well in the angle ranges between -14° and 32° (forth) as well as 115° and 36° (back). Models that use vibrations measured by sensor 4 do not perform well in the angle ranges between -14° and 32° (forth), but perform well in angle ranges between 115° and 36° (back). Models that use vibrations measured by sensors 3 and 4 also perform well in angle ranges between 170° and 115° (back). In short, this means that there are suitable and unsuitable angle ranges to detect changes in the vibration due to aging of the swivel joint.

The model accuracies that use two-second-long samples are given in the appendix in the tables C.4 and C.5. Out of 76 calculated cases, in 55 cases the model achieves an accuracy

Table 6.1.: Accuracies of classification of cycles in different stages of aging: after 4000 cycles, after 7000 cycles, after 10,000 cycles. Sample length is one second. Vibrations taken from the sensors on the swivel joint on the east side.

Sensor	Angle Range	6 PCs	8 PCs	10 PCs	12 PCs	14 PCs	16 PCs	18 PCs
1	(-21°)-(-14°)	87.0	93.8	91.0	93.2	93.8	94.4	94.9
1	(-14°)-(-3°)	94.7	95.1	95.8	94.7	93.3	94.0	95.8
1	(-1°)-11°	97.3	97.6	98.0	99.7	99.7	99.7	99.7
1	11°-20°	96.8	95.8	95.8	96.3	97.7	97.7	97.7
1	20°-32°	95.7	95.7	96.3	95.5	94.4	96.8	96.8
1	35°-79°	83.9	89.5	90.0	89.7	90.6	91.6	91.9
1	79°-131°	58.3	59.0	61.8	63.8	65.8	65.8	65.6
1	133°-187°	75.3	80.8	81.2	85.8	85.6	85.5	85.9
1	185°-179°	91.5	88.3	92.2	92.2	95.5	94.8	94.8
1	170°-155°	91.3	90.4	91.5	94.3	94.3	93.7	93.7
1	155°-135°	82.7	82.4	80.4	84.2	85.6	85.4	85.8
1	135°-115°	84.9	88.4	90.2	91.5	92.6	92.5	93.0
1	115°-105°	92.4	95.1	96.3	93.9	96.4	96.4	96.4
1	105°-79°	89.6	92.1	93.5	95.1	94.9	95.1	95.3
1	76°-47°	90.9	93.3	93.5	94.3	95.8	98.3	98.3
1	47°-36°	93.2	92.9	92.9	94.0	95.8	99.0	98.7
1	34°-14°	91.1	94.1	94.7	94.4	95.0	97.3	97.1
1	14°-0°	97.1	96.3	96.2	96.0	96.9	97.1	97.1
1	0°-(-23.5°)	90.7	92.2	94.4	95.0	95.0	94.8	94.8
2	(-21°)-(-14°)	89.2	93.2	92.1	94.3	94.3	94.9	94.3
2	(-14°)-(-3°)	89.0	90.1	91.9	95.0	93.3	94.3	93.6
2	(-1°)-11°	93.9	96.3	96.3	99.0	98.6	98.6	98.6
2	11°-20°	84.7	91.2	92.1	96.8	98.6	98.6	98.6
2	20°-32°	83.2	88.2	89.1	96.0	95.5	95.7	95.7
2	35°-79°	91.8	93.1	94.1	94.0	94.4	95.6	97.4
2	79°-131°	66.0	69.1	68.9	71.2	74.2	76.7	76.7
2	133°-187°	68.4	70.9	75.7	79.1	79.7	81.2	81.1
2	185°-179°	96.1	95.5	96.1	94.8	96.1	96.7	96.7
2	170°-155°	76.2	79.0	82.0	80.0	86.6	87.7	88.0
2	155°-135°	88.4	88.1	87.4	90.4	90.6	90.9	91.1
2	135°-115°	85.7	85.6	87.2	87.5	87.4	88.4	88.7
2	115°-105°	91.8	93.6	96.4	96.7	95.8	95.5	95.5
2	105°-79°	89.3	95.1	97.2	97.5	97.9	98.8	98.8
2	76°-47°	91.6	96.6	97.7	97.5	98.6	98.8	98.9
2	47°-36°	93.5	94.0	98.2	98.4	98.4	99.0	99.0
2	34°-14°	91.1	93.1	94.7	95.3	95.4	96.7	96.5
2	14°-0°	91.0	93.5	94.2	94.2	95.0	94.2	93.3
2	0°-(-23.5°)	89.5	91.9	95.1	95.2	96.4	96.1	96.1

Table 6.2.: Accuracies of classification of cycles in different stages of aging: after 4000 cycles, after 7000 cycles, after 10,000 cycles. Sample length is one second. Vibrations taken from the sensors on the swivel joint on the west side.

Sensor	Angle Range	6 PCs	8 PCs	10 PCs	12 PCs	14 PCs	16 PCs	18 PCs
3	(-21°)-(-14°)	89.3	91.0	89.8	89.8	91.0	89.3	91.5
3	(-14°)-(-3°)	99.3	100.0	100.0	100.0	100.0	100.0	100.0
3	(-1°)-11°	92.6	95.6	97.0	98.0	98.0	98.7	98.7
3	11°-20°	93.1	94.0	93.5	92.6	94.0	94.0	94.0
3	20°-32°	89.8	90.9	93.6	94.1	94.1	95.2	96.0
3	35°-79°	85.5	94.2	95.0	96.2	96.5	97.7	97.9
3	79°-131°	61.3	66.4	70.2	76.5	80.8	81.7	81.7
3	133°-187°	78.0	84.5	85.8	87.4	87.6	89.2	89.4
3	185°-179°	91.6	90.9	92.2	93.5	94.2	94.8	94.8
3	170°-155°	94.3	94.5	94.8	94.8	96.5	97.8	97.8
3	155°-135°	97.0	96.8	95.2	95.9	95.9	96.1	96.1
3	135°-115°	99.5	98.7	98.9	98.9	99.2	99.2	99.2
3	115°-105°	99.1	99.1	99.1	98.8	98.8	98.8	98.8
3	105°-79°	92.7	93.0	92.9	93.8	93.9	93.4	94.5
3	76°-47°	90.0	91.1	90.9	91.2	93.5	92.8	93.0
3	47°-36°	97.1	96.9	95.8	96.6	96.3	97.6	97.4
3	34°-14°	95.7	94.7	94.5	96.0	95.5	95.7	95.8
3	14°-0°	72.9	79.2	79.2	82.3	87.7	85.8	84.8
3	0°-(-23.5°)	64.7	71.9	75.7	75.0	84.2	85.0	85.6
4	(-21°)-(-14°)	83.6	85.8	88.1	89.8	92.1	90.4	89.8
4	(-14°)-(-3°)	94.0	93.3	92.9	93.6	94.7	95.4	94.7
4	(-1°)-11°	88.9	92.3	91.6	91.6	92.3	92.6	92.6
4	11°-20°	85.2	83.3	83.8	85.2	87.0	84.3	84.3
4	20°-32°	82.4	83.4	83.4	86.6	91.7	89.8	89.8
4	35°-79°	80.7	86.4	90.3	91.4	94.5	95.0	94.7
4	79°-131°	59.7	61.4	63.1	69.1	69.4	71.3	71.8
4	133°-187°	70.6	73.7	75.9	76.4	80.0	80.4	81.2
4	185°-179°	84.4	83.8	88.3	90.3	92.2	91.6	91.6
4	170°-155°	96.7	97.0	97.0	97.5	96.7	96.7	96.7
4	155°-135°	94.5	95.7	94.3	93.2	95.0	95.0	95.0
4	135°-115°	94.3	94.1	96.1	96.2	96.2	97.1	97.1
4	115°-105°	98.8	97.9	98.8	98.8	98.5	98.2	98.2
4	105°-79°	99.0	98.9	98.9	99.4	99.2	99.3	99.3
4	76°-47°	92.8	93.5	93.3	93.8	94.1	95.4	95.5
4	47°-36°	98.2	99.2	99.5	99.7	99.7	99.7	99.7
4	34°-14°	90.1	92.1	92.4	92.1	92.7	92.2	92.5
4	14°-0°	81.7	82.9	83.8	84.2	83.8	83.5	84.2
4	0°-(-23.5°)	68.5	67.3	69.9	71.2	71.1	70.9	70.6
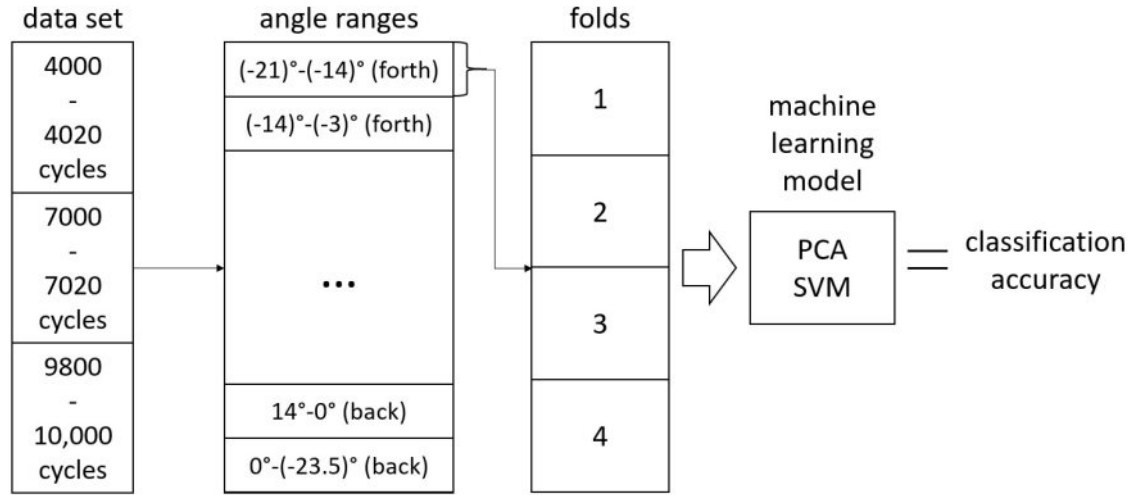
Figure 6.24.: Preparation process of the data set for the machine learning model. The data set includes samples with the extracted features. These are divided into angle ranges and folds. The machine learning model, consisting of PCA and SVM, is trained and a classification accuracy is calculated.

above 95 %, and in 13 cases it even achieves an accuracy of 100 %. In this case the worst performing angle ranges are also from 79° to 131° (forth) and 133° to 187° (forth). The best performing angle ranges are the same when a sample length of one second is used, however in most cases classification accuracy is increased. This shows that a sample length of two seconds leads to a better classification performance.

The high accuracies achieved indicate that the proposed machine learning model is a promising approach for vibration analysis of the swivel joints.

7. Summary and Outlook

Rotation and Expansion Performing Assemblies (REPAs), are among the most critical components in Parabolic Trough Collectors (PTCs). They have to withstand forces and torques due to the rotation and thermal expansion/contraction of the receiver tube. REPAs perform around 10,000 sun tracking cycles in their lifetime.

Within the scope of this work, vibration sensors were implemented for condition monitoring based maintenance of the REPAs. First, a vibration analysis and predictive maintenance literature research was presented. Some of the most implemented algorithms in this area, Short Time Fourier Transform (STFT), principal component analysis (PCA) and support vector machine (SVM), were described and later used to analyze the measured vibration.

Both pressure and aging tests were carried out for two swivel joints and rotation flex hose assemblies (RFHAs). Vibrations were recorded online and spectrograms through the use of STFT were produced. Studying those, it was shown that both pressure and cycling have an affect on the vibration measurement. Therefore, vibration analysis was demonstrated to be a suitable tool for condition monitoring swivel joints and RFHAs.

A machine learning model was proposed to classify samples of the vibration signal depending on the swivel joint's condition. The classification accuracy was found depending on several variables, namely traverse angle ranges, sample lengths, number of principal components (PCs) and the parameter C while executing Support Vector Machine (SVM). For these variables, multiple values and ranges were tried out. The machine learning model achieved a high accuracy classifying samples at different stages of the aging process.

Despite the relevant contributions achieved in this master thesis, there are some aspects that could be further developed. For instance, along the 10,000 cycles no swivel joint malfunction occurred. Therefore, the vibration behavior at a failure was not investigated.

Given that the swivel joint's vibration behavior depends on many parameters such as pressure, temperature, piston change angles, geometry of the PTC and more, the vibrations recorded at the REPA test rig can not be compared to vibrations in other PTC facilities. However, the methods presented in this work are valid and can be applied.

More data need to be gathered to further analyze vibrations. Especially the ones of REPA failures to investigate how the vibration behavior evolves before malfunction. Without such data, predictive maintenance is not possible. A way of doing this is installing sensors on multiple swivel joints in a real PTC power plant, in which the swivel joints are operated under the same conditions. This can be achieved by using a setup with Raspberry Pi devices to log the data, for example. This way, it would be easier to track the changes of vibration behavior online.

Bibliography

[1] Cajetan M. Akujuobi. *Wavelets and Wavelet Transform Systems and Their Applications : A Digital Signal Processing Approach*. Cham, 2022.

[2] N. Bachschmid and Steven Chatterton. 'Dynamical Behavior of Rotating Machinery in Non-Stationary Conditions: Simulation and Experimental Results'. In: Oct. 2014, pp. 3–21. ISBN: 978-3-642-39347-1. DOI: 10.1007/978-3-642-39348-8_1.

[3] Kirk Baker. 'Singular value decomposition tutorial'. In: *The Ohio State University* 24 (2005).

[4] John J. Burkhardt, Garvin A. Heath and Craig S. Turchi. 'Life Cycle Assessment of a Parabolic Trough Concentrating Solar Power Plant and the Impacts of Key Design Alternatives'. In: *Environmental Science & Technology* 45.6 (2011), pp. 2457–2464. DOI: 10.1021/es1033266.

[5] Huseyin Murat Cekirge and Ammar Elhassan. 'A comparison of solar power systems (CSP): solar tower (ST) systems versus parabolic trough (PT) systems'. In: *American Journal of Energy Engineering* 3.3 (2015), pp. 29–36.

[6] Patrick Flandrin, Paulo Gonçalvès and Gabriel Rilling. 'Detrending and denoising with empirical mode decompositions'. In: *2004 12th European Signal Processing Conference*. 2004, pp. 1581–1584.

[7] Tristan Fletcher. 'Support vector machines explained'. In: *Tutorial paper* (2009), pp. 1–19.

[8] Hüseyin Gökçekuş and Youssef Kassem, eds. *Climate Change, Natural Resources and Sustainable Environmental Management*. Cham, 2022.

[9] Trevor Hastie et al. 'The entire regularization path for the support vector machine'. In: *Journal of Machine Learning Research* 5.Oct (2004), pp. 1391–1415.

[10] Michael Hegemann. *Ein Entscheidungsunterstützungssystem zur Priorisierung ungeplanter Stillstände für eine ausbringungsoptimierte Durchführung reaktiver sowie proaktiver Instandhaltungsmaßnahmen*. Karlsruhe, 2021. URL: http://dx.doi.org/10.5445/IR/1000130039.

[11] Tobias Hilbel. 'Design of the Motion control for a test rig analyizing Rotation and Expansion performing assemblies in parabolic trough collector power plant applications'. Bachelor's Thesis. Hochschule Mannheim, 2017.

[12] Andreas Holtschulte. *Praxisleitfaden IoT und Industrie 4.0 : Methoden, Tools und Use Cases für Logistik und Produktion*. München, 2021.

[13] Norden Huang and Zhaohua Wu. 'A Review on Hilbert-Hung Transform Method and Its Applications to Geophysical Studies'. In: *Reviews of Geophysics* 46 (June 2008), RG2006. DOI: 10.1029/2007RG000228.

[14] *ICP®ACCELEROMETER*. 352C03. PCB Piezotronics. Sept. 2006.

[15] *ICP®ACCELEROMETER*. 320C52. PCB Piezotronics. June 2012.

[16] *InnoBeamer: USB Datenerfassungsgerät für VibroMatrix*. InnoBeamer L2. IDS Innomic Schwingungsmesstechnik GmbH. Feb. 2010.

[17] Vikramaditya Jakkula. 'Tutorial on support vector machine (svm)'. In: *School of EECS, Washington State University* 37.2.5 (2006), p. 3.

[18] Ian T Jolliffe. 'Principal component analysis: a beginner's guide—I. Introduction and application'. In: *Weather* 45.10 (1990), pp. 375–382.

[19] C. Jonscher et al. 'Very low frequency IEPE accelerometer calibration and application to a wind energy structure'. In: *Wind Energy Science* 7.3 (2022), pp. 1053–1067. DOI: 10.5194/wes-7-1053-2022. URL: https://wes.copernicus.org/articles/7/1053/2022/.

[20] Alexander Jung. *Machine Learning : The Basics*. Singapore, 2022.

[21] Pavan Kumar Kankar, Satish C. Sharma and Suraj Prakash Harsha. 'Fault diagnosis of ball bearings using machine learning methods'. In: *Expert Systems with applications* 38.3 (2011), pp. 1876–1886.

[22] Adarsh Kumar et al. 'Detection and classification for faults in drilling process using vibration analysis'. In: *2014 International Conference on Prognostics and Health Management*. 2014, pp. 1–6. DOI: 10.1109/ICPHM.2014.7036393.

[23] Edward W. Law et al. 'Direct normal irradiance forecasting and its application to concentrated solar thermal output forecasting – A review'. In: *Solar Energy* 108 (2014), pp. 287–307. ISSN: 0038-092X. DOI: https://doi.org/10.1016/j.solener.2014.07.008. URL: https://www.sciencedirect.com/science/article/pii/S0038092X14003466.

[24] Jonguk Lee et al. 'Fault detection and diagnosis of railway point machines by sound analysis'. In: *Sensors* 16.4 (2016), p. 549.

[25] A.M. Martinez and A.C. Kak. 'PCA versus LDA'. In: *IEEE Transactions on Pattern Analysis and Machine Intelligence* 23.2 (2001), pp. 228–233. DOI: 10.1109/34.908974.

[26] Martin Meyer. *Signalverarbeitung : analoge und digitale Signale, Systeme und Filter*. Wiesbaden, 2021.

[27] *Miniature Accelerometers*. KS94B10, KS94B100, KS94L, KS95B10, KS95B100. AVIBIA GmbH. Jan. 2018.

[28] Ibrahim Moukhtar. *Solar Energy : Technologies, Design, Modeling, and Economics*. Ed. by Adel Z. El Dein, Adel A. Elbaset and Yasunori Mitani. Cham, 2021.

[29] David E. Newland. 'Wavelet Analysis of Vibration Signals'. In: *Handbook of Noise and Vibration Control.* John Wiley & Sons, Ltd, 2007. Chap. 49, pp. 585–597. ISBN: 9780470209707. DOI: `https://doi.org/10.1002/9780470209707.ch49`. URL: `https://onlinelibrary.wiley.com/doi/abs/10.1002/9780470209707.ch49`.

[30] Rui Nie et al. 'A general Fourier formulation for in-plane and out-of-plane vibration analysis of curved beams'. In: *Shock and Vibration* 2021 (2021).

[31] William S. Noble. 'What is a support vector machine?' In: *Nature biotechnology* 24.12 (2006), pp. 1565–1567.

[32] Andreas Plumpe. 'Design of a Test Rig and its Testing Methods for Rotation and Expansion Performing Assemblies in Parabolic Trough Collector Power Plants'. MA thesis. Apr. 2016.

[33] Hank Price et al. 'Advances in Parabolic Trough Solar Power Technology'. In: *Journal of Solar Energy Engineering-transactions of The Asme - J SOL ENERGY ENG* 124 (May 2002). DOI: `10.1115/1.1467922`.

[34] Robert Bond Randall. *Vibration-based condition monitoring : industrial, aerospace, and automotive applications.* Chichester, West Sussex, U.K, 2011. URL: `https://swbplus.bsz-bw.de/bsz336198086cov.jpghttp://lib.myilibrary.com/detail.asp?id=310092%20;%20https://ebookcentral.proquest.com/lib/kxp/detail.action?docID=645002`.

[35] Markus Ringnér. 'What is principal component analysis?' In: *Nature biotechnology* 26.3 (Mar. 2008), pp. 303–304. ISSN: 1087-0156. DOI: `10.1038/nbt0308-303`. URL: `https://doi.org/10.1038/nbt0308-303`.

[36] Kaveh Samiee, Péter Kovács and Moncef Gabbouj. 'Epileptic Seizure Classification of EEG Time-Series Using Rational Discrete Short-Time Fourier Transform'. In: *IEEE Transactions on Biomedical Engineering* 62.2 (2015), pp. 541–552. DOI: `10.1109/TBME.2014.2360101`.

[37] Falko Schneider. 'Commissioning and optimization of a test bench for life cycle Analysis of Rotation and Expansion performing assemblies (REPAs) in parabolic trough collector power plants'. MA thesis. May 2019.

[38] Ryan Shininger et al. 'Flexible hose interconnect testing for parabolic troughs with nitrate salt'. In: *AIP Conference Proceedings* 2303.1 (2020), p. 150014. DOI: `10.1063/5.0029000`.

[39] Sri Niwas Singh, Prabhakar Tiwari and Sumit Tiwari, eds. *Fundamentals and Innovations in Solar Energy.* Singapore, 2021.

[40] *Solar resource maps and GIS data for 200+ countries.* Solargis. 2022. URL: `https://solargis.com/maps-and-gis-data/download/world` (visited on 26/08/2022).

[41] Fengxi Song, Zhongwei Guo and Dayong Mei. 'Feature Selection Using Principal Component Analysis'. In: *2010 International Conference on System Science, Engineering Design and Manufacturing Informatization.* Vol. 1. 2010, pp. 27–30. DOI: `10.1109/ICSEM.2010.14`.

[42] Shan Suthaharan. 'Support vector machine'. In: *Machine learning models and algorithms for big data classification*. Springer, 2016, pp. 207–235.

[43] Monica Tiboni et al. 'A Review on Vibration-Based Condition Monitoring of Rotating Machinery'. In: *Applied Sciences* 12.3 (2022). ISSN: 2076-3417. DOI: `10.3390/app12030972`. URL: `https://www.mdpi.com/2076-3417/12/3/972`.

[44] Thanh Tran and Jan Lundgren. 'Drill Fault Diagnosis Based on the Scalogram and Mel Spectrogram of Sound Signals Using Artificial Intelligence'. In: *IEEE Access* 8 (2020), pp. 203655–203666. DOI: `10.1109/ACCESS.2020.3036769`.

[45] Sergio Valle, Weihua Li and S Joe Qin. 'Selection of the number of principal components: the variance of the reconstruction error criterion with a comparison to other methods'. In: *Industrial & Engineering Chemistry Research* 38.11 (1999), pp. 4389–4401.

[46] Johannes Wagner and Jan Burgemeister. *Piezoelectric Accelerometers: Theory and Application*. 6th July 2022. URL: `https://www.mmf.de/manual/aufnehmerman.pdf`.

[47] Hongjun Wang and Yongjian Ji. 'A Revised Hilbert–Huang Transform and Its Application to Fault Diagnosis in a Rotor System'. In: *Sensors* 18.12 (2018). ISSN: 1424-8220. URL: `https://www.mdpi.com/1424-8220/18/12/4329`.

[48] Feng Xiao et al. 'Condition monitoring and vibration analysis of wind turbine'. In: *Advances in Mechanical Engineering* 12.3 (2020). DOI: `10.1177/1687814020913782`. URL: `https://doi.org/10.1177/1687814020913782`.

[49] Minglan Xiong et al. 'Digital twin–driven aero-engine intelligent predictive maintenance'. In: *The International Journal of Advanced Manufacturing Technology* 114 (June 2021), pp. 1–11. DOI: `10.1007/s00170-021-06976-w`.

[50] Grzegorz Żak et al. 'Application of ARMA modelling and alpha-stable distribution for local damage detection in bearings'. In: 2014.

[51] Angela Zeiler et al. 'Empirical Mode Decomposition - An Introduction'. In: July 2010, pp. 1–8. DOI: `10.1109/IJCNN.2010.5596829`.

Appendix

A. Spectrograms of the west swivel joint during the aging test
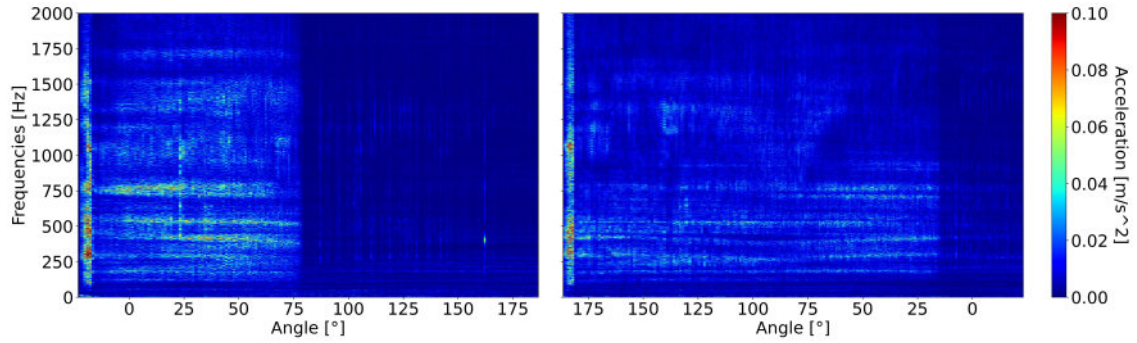
Figure A.1.: Spectrogram of the 4000th cycle showing the frequencies and their amplitudes of the vibrations that were measured with sensor 3 (perpendicular to the REPA) over the traverse angle.
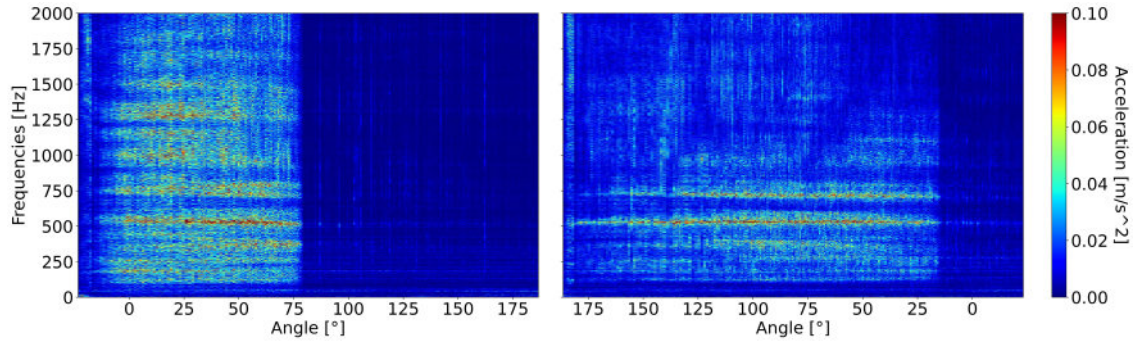
Figure A.2.: Spectrogram of the 4000th cycle showing the frequencies and their amplitudes of the vibrations that were measured with sensor 4 (in opposite direction of the REPA) over the traverse angle.
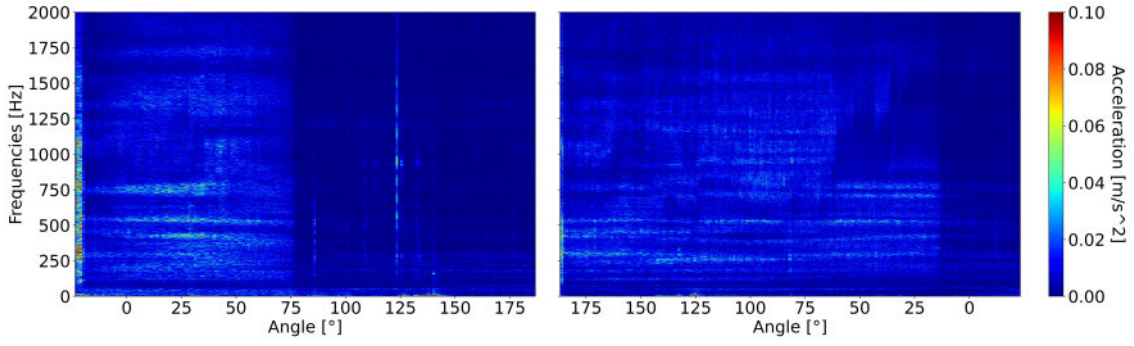
Figure A.3.: Spectrogram of the 7000th cycle showing the frequencies and their amplitudes of the vibrations that were measured with sensor 1 over the traverse angle.
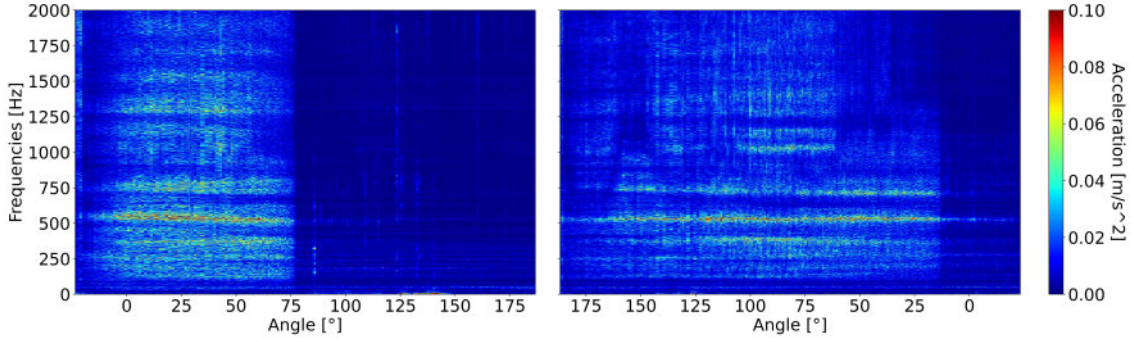
Figure A.4.: Spectrogram of the 7000th cycle showing the frequencies and their amplitudes of the vibrations that were measured with sensor 2 over the traverse angle.
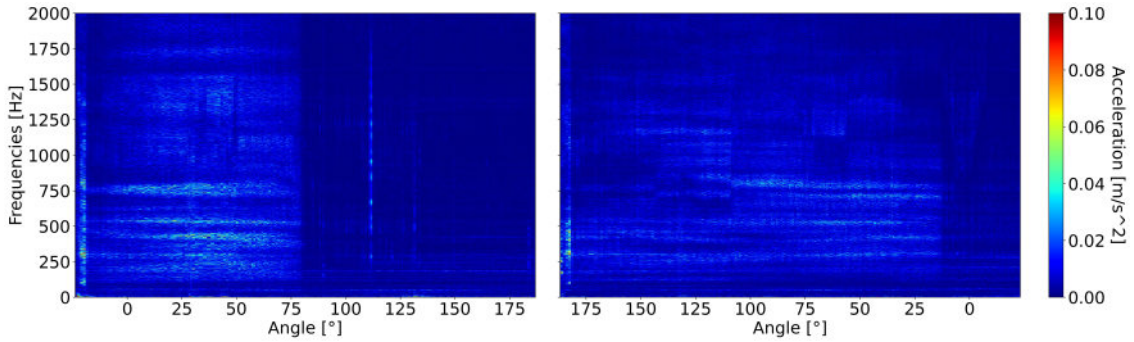
Figure A.5.: Spectrogram of the 10,000th cycle showing the frequencies and their amplitudes of the vibrations that were measured with sensor 3 over the traverse angle.
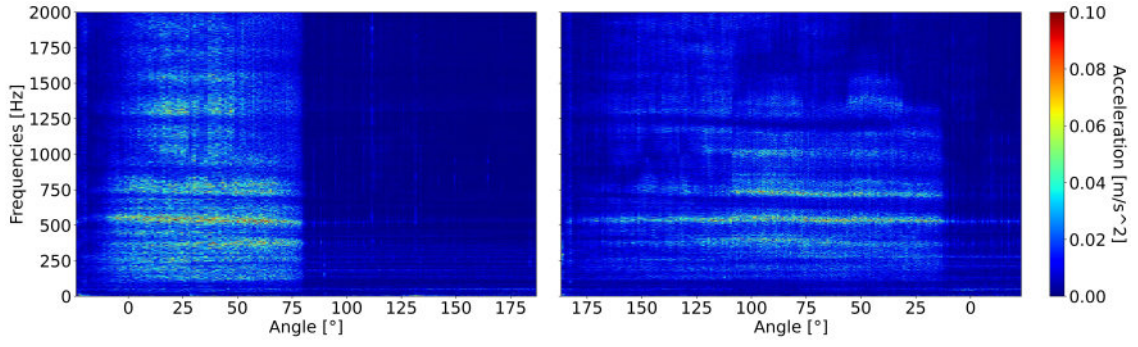
Figure A.6.: Spectrogram of the 10,000th cycle showing the frequencies and their amplitudes of the vibrations that were measured with sensor 4 over the traverse angle.

B. Classification accuracies of cycles at different pressures

Table B.1.: Classification of cycles at different pressures for different parameters C. Sample length is one second and 8 PCs are used.

Sensor	Angle range	C=10	C=100	C=1000
1	0°-31°	0.968	0.968	0.968
1	36°-62°	0.858	0.858	0.858
1	62°-100°	0.906	0.877	0.87
1	100°-128°	0.886	0.896	0.896
1	135°-155°	0.932	0.932	0.932
1	155°-178°	0.956	0.956	0.956
1	160°-137°	0.879	0.857	0.89
1	132°-110°	0.569	0.55	0.55
1	100°-40°	0.829	0.819	0.819
1	25°-(-15°)	0.813	0.813	0.813
2	0°-31°	0.732	0.748	0.748
2	36°-62°	0.653	0.638	0.653
2	62°-100°	0.659	0.649	0.645
2	100°-128°	0.847	0.836	0.83
2	135°-155°	0.684	0.693	0.693
2	155°-178°	0.658	0.671	0.671
2	160°-137°	0.857	0.802	0.813
2	132°-110°	0.766	0.776	0.785
2	100°-40°	0.691	0.691	0.689
2	25°-(-15°)	0.644	0.648	0.64
3	0°-31°	0.938	0.929	0.929
3	36°-62°	0.882	0.89	0.89
3	62°-100°	0.797	0.804	0.801
3	100°-128°	0.847	0.853	0.853
3	135°-155°	0.838	0.803	0.795
3	155°-178°	0.937	0.943	0.937
3	160°-137°	0.823	0.845	0.844
3	132°-110°	0.618	0.589	0.599
3	100°-40°	0.706	0.708	0.708
3	25°-(-15°)	0.764	0.779	0.775

Table B.2.: Accuracies of classification of cycles at different pressures: 0 bar, 10 bar, 20 bar, 30 bar and 35 bar. Sample length is one second.

Sensor	Zone	6 PCs	8 PCs	10 PCs	12 PCs	14 PCs	16 PCs	18 PCs
1	0°-31°	94.4	96.8	97.6	96.8	96.8	96.8	96.8
1	36°-62°	85.8	85.8	83.5	86.6	88.2	88.2	88.2
1	62°-100°	89.5	87.7	90.2	92.8	93.1	94.9	94.9
1	100°-128°	79.2	89.6	94.5	95.6	96.2	96.7	96.7
1	135°-155°	89.7	93.2	94.0	94.0	95.7	95.7	95.7
1	155°-178°	93.1	95.6	95.0	96.9	96.2	96.2	96.2
1	160°-137°	79.1	85.7	86.9	89.1	89.1	89.1	90.2
1	132°-110°	52.9	55.0	65.7	64.7	70.5	69.5	69.5
1	100°-40°	76.3	81.9	81.7	79.6	80.5	81.9	82.2
1	25°-(-15°)	77.5	81.3	80.5	79.0	82.0	81.6	80.9
2	0°-31°	73.3	74.8	74.1	82.0	82.7	82.7	81.9
2	36°-62°	60.6	63.8	64.6	63.8	63.0	62.2	61.4
2	62°-100°	59.8	64.9	65.2	69.6	68.1	69.2	71.4
2	100°-128°	80.3	83.6	84.1	84.7	82.5	84.1	83.0
2	135°-155°	66.7	69.3	65.9	64.1	68.4	72.6	73.5
2	155°-178°	66.4	67.1	71.5	73.4	79.7	83.6	83.6
2	160°-137°	76.9	80.2	83.4	82.3	81.2	81.2	81.2
2	132°-110°	67.7	77.6	80.5	82.4	77.5	77.6	76.6
2	100°-40°	68.2	69.1	71.5	74.1	73.9	75.1	74.6
2	25°-(-15°)	57.3	64.8	69.7	70.0	71.9	73.4	73.4
3	0°-31°	89.8	92.9	96.1	96.1	96.1	96.9	96.9
3	36°-62°	85.9	89.0	85.9	84.2	82.6	81.0	81.0
3	62°-100°	76.8	80.4	83.0	82.2	81.9	80.8	80.8
3	100°-128°	82.5	85.3	84.7	83.6	82.5	84.2	85.3
3	135°-155°	71.0	80.3	86.3	86.3	88.9	88.1	88.1
3	155°-178°	87.4	94.3	89.9	92.4	91.8	93.7	93.7
3	160°-137°	88.9	84.5	84.5	86.7	86.8	87.8	87.8
3	132°-110°	65.8	58.9	65.7	69.7	67.7	66.7	65.7
3	100°-40°	67.7	70.8	77.4	77.7	75.5	80.0	80.3
3	25°-(-15°)	73.4	77.9	81.3	83.1	82.8	83.9	83.2

Table B.3.: Accuracies of classification of cycles at different pressures: 0 bar, 10 bar, 20 bar, 30 bar and 35 bar. Sample length is two seconds.

Sensor	Zone	6 PCs	8 PCs	10 PCs	12 PCs	14 PCs	16 PCs	18 PCs
1	0°-31°	86.2	93.8	90.7	90.7	90.8	90.8	90.8
1	36°-62°	89.4	84.8	89.4	89.4	89.4	89.4	89.4
1	62°-100°	89.1	91.3	91.3	92.0	92.7	92.0	92.0
1	100°-128°	82.6	89.1	90.2	90.2	92.4	95.7	95.7
1	135°-155°	96.7	95.0	95.0	96.7	95.0	95.0	95.0
1	155°-178°	94.7	88.1	90.7	92.0	92.0	92.0	92.0
1	160°-137°	60.6	58.3	64.8	60.4	66.7	66.7	66.7
1	132°-110°	55.6	71.8	71.8	73.9	79.8	79.8	79.8
1	100°-40°	81.1	83.4	84.9	88.7	85.3	85.8	86.7
1	25°-(-15°)	83.7	82.2	83.7	85.2	81.5	80.7	80.7
2	0°-31°	75.8	84.7	80.4	78.8	78.9	80.3	81.8
2	36°-62°	63.3	55.6	57.2	58.8	63.4	63.4	64.9
2	62°-100°	65.2	65.9	65.9	73.2	65.2	68.8	69.5
2	100°-128°	78.3	82.6	85.9	89.1	91.3	90.2	90.2
2	135°-155°	68.3	65.0	66.7	71.7	70.0	71.7	71.7
2	155°-178°	70.7	70.7	67.8	79.9	82.7	86.7	86.7
2	160°-137°	75.4	79.7	73.3	75.4	77.7	77.7	77.7
2	132°-110°	67.9	82.1	82.1	82.1	80.1	80.1	80.1
2	100°-40°	72.5	73.9	75.8	74.4	73.4	73.4	73.9
2	25°-(-15°)	59.2	67.4	67.4	71.1	74.1	73.3	71.1
3	0°-31°	86.2	93.9	95.4	95.4	95.4	95.4	95.4
3	36°-62°	91.0	89.4	84.7	84.7	83.2	83.2	83.2
3	62°-100°	76.8	75.4	81.9	80.5	78.3	79.7	79.0
3	100°-128°	78.3	87.0	83.7	87.0	85.9	83.7	82.6
3	135°-155°	75.0	85.0	91.7	91.7	88.3	88.3	88.3
3	155°-178°	85.3	90.8	89.3	86.7	89.4	88.1	89.4
3	160°-137°	79.9	82.2	75.6	75.4	73.3	73.3	73.3
3	132°-110°	68.1	70.4	74.0	76.3	76.3	76.3	74.4
3	100°-40°	67.8	69.6	72.5	72.0	76.3	79.6	78.2
3	25°-(-15°)	74.1	73.4	80.0	79.3	80.8	79.3	80.1

C. Classification accuracies of cycles over aging process

Table C.4.: Accuracies of classification of cycles in different stages of aging: after 4000 cycles, after 7000 cycles, after 10,000 cycles. Sample length is two seconds. Vibrations taken from the sensors on the swivel joint on the east side.

Sensor	Angle Range	6 PCs	8 PCs	10 PCs	12 PCs	14 PCs	16 PCs	18 PCs
1	(-21°)-(-14°)	94.3	94.3	98.9	97.7	97.7	97.7	97.7
1	(-14°)-(-3°)	99.2	98.5	99.2	99.2	99.2	99.2	99.2
1	(-1°)-11°	99.3	98.0	95.3	99.3	99.3	99.3	99.3
1	11°-20°	99.1	98.1	100.0	100.0	100.0	100.0	100.0
1	20°-32°	97.8	97.3	97.8	98.4	98.4	98.4	98.4
1	35°-79°	90.1	89.7	93.1	93.5	93.9	94.9	94.5
1	79°-131°	67.2	70.2	72.9	73.6	73.3	74.4	73.9
1	133°-187°	88.7	89.9	90.3	91.3	90.5	90.1	90.5
1	185°-179°	91.7	90.3	88.9	90.3	90.3	90.3	90.3
1	170°-155°	90.4	91.5	91.5	94.1	94.1	93.6	93.6
1	155°-135°	87.0	88.8	86.0	85.6	91.9	90.1	90.1
1	135°-115°	88.5	90.1	94.7	95.7	94.7	96.1	96.1
1	115°-105°	95.7	95.1	95.7	95.1	95.7	95.7	95.7
1	105°-79°	96.5	96.9	97.1	96.9	96.5	95.8	95.8
1	76°-47°	93.6	94.5	94.9	97.2	99.3	99.3	99.3
1	47°-36°	92.5	92.5	93.0	94.5	96.5	98.0	98.0
1	34°-14°	91.2	96.6	98.6	98.3	98.0	99.1	99.1
1	14°-0°	100.0	100.0	100.0	100.0	100.0	100.0	100.0
1	0°-(-23.5°)	93.6	97.7	98.6	97.7	98.4	98.2	98.2
2	(-21°)-(-14°)	92.0	92.0	95.5	92.0	93.2	92.0	92.0
2	(-14°)-(-3°)	91.7	93.9	97.0	94.7	95.5	94.7	94.7
2	(-1°)-11°	93.2	93.9	92.6	95.3	95.9	95.9	95.9
2	11°-20°	89.0	90.0	92.8	94.6	95.5	95.5	95.5
2	20°-32°	82.6	83.2	90.2	89.1	90.2	94.6	94.6
2	35°-79°	92.2	95.9	96.6	96.3	96.3	98.2	97.9
2	79°-131°	79.4	79.2	78.8	80.1	80.9	81.6	81.6
2	133°-187°	81.5	82.7	85.1	87.9	88.2	88.1	87.9
2	185°-179°	97.2	97.2	97.2	97.2	97.2	97.2	97.2
2	170°-155°	87.2	93.6	92.6	94.1	93.1	93.6	93.6
2	155°-135°	91.0	91.9	92.3	90.5	89.6	88.2	88.2
2	135°-115°	90.5	90.5	90.8	93.1	92.8	94.4	94.4
2	115°-105°	93.9	94.5	94.5	95.7	96.3	96.3	96.3
2	105°-79°	91.4	95.4	96.5	96.2	98.1	98.5	98.5
2	76°-47°	95.7	97.9	98.2	98.2	99.8	99.8	99.8
2	47°-36°	99.0	98.5	99.0	99.5	100.0	100.0	100.0
2	34°-14°	92.3	92.6	94.0	95.7	96.3	96.0	96.0
2	14°-0°	93.5	95.4	97.0	98.9	97.7	98.1	98.1
2	0°-(-23.5°)	91.7	97.2	96.8	96.3	95.6	96.3	96.6

Table C.5.: Accuracies of classification of cycles in different stages of aging: after 4000
cycles, after 7000 cycles, after 10,000 cycles. Sample length is two seconds.
Vibrations taken from the sensors on the swivel joint on the west side.

Sensor	Angle Range	6 PCs	8 PCs	10 PCs	12 PCs	14 PCs	16 PCs	18 PCs
3	(-21°)-(-14°)	97.7	98.9	100.0	100.0	100.0	100.0	100.0
3	(-14°)-(-3°)	100.0	100.0	100.0	100.0	100.0	100.0	100.0
3	(-1°)-11°	94.6	95.9	98.6	100.0	100.0	100.0	100.0
3	11°-20°	92.7	98.1	100.0	99.1	99.1	99.1	99.1
3	20°-32°	91.8	94.6	94.6	95.7	96.2	97.8	97.3
3	35°-79°	95.0	95.9	96.5	97.0	98.4	98.7	98.7
3	79°-131°	68.0	71.6	74.6	83.3	88.8	89.3	89.5
3	133°-187°	82.4	88.0	87.7	89.5	89.8	91.6	91.8
3	185°-179°	97.2	98.6	97.2	97.2	98.6	98.6	98.6
3	170°-155°	97.9	98.4	98.4	100.0	100.0	99.5	99.5
3	155°-135°	96.8	98.6	98.2	99.5	99.1	99.1	99.1
3	135°-115°	98.0	99.0	98.7	99.3	99.3	99.7	99.7
3	115°-105°	100.0	100.0	100.0	100.0	100.0	100.0	100.0
3	105°-79°	96.7	96.9	96.3	97.1	96.0	95.6	95.4
3	76°-47°	95.2	93.8	94.5	94.9	95.2	95.9	95.9
3	47°-36°	97.0	96.0	96.5	97.0	98.0	98.0	98.0
3	34°-14°	97.1	97.1	96.9	97.7	98.6	97.7	97.7
3	14°-0°	85.1	87.8	92.4	93.5	96.9	97.0	97.0
3	0°-(-23.5°)	77.7	83.2	86.4	89.0	89.4	88.3	89.2
4	(-21°)-(-14°)	90.9	95.5	95.5	97.7	97.7	97.7	97.7
4	(-14°)-(-3°)	97.0	97.0	99.2	98.5	99.2	99.2	99.2
4	(-1°)-11°	92.6	96.6	95.3	95.3	94.6	95.3	95.3
4	11°-20°	75.3	79.0	85.4	84.4	84.5	82.6	82.6
4	20°-32°	85.3	90.2	91.8	94.0	95.1	95.1	95.1
4	35°-79°	83.1	92.5	95.6	96.7	96.9	97.0	96.9
4	79°-131°	66.4	69.0	72.6	78.7	79.4	81.9	81.7
4	133°-187°	78.7	81.6	84.3	83.9	84.8	86.6	86.7
4	185°-179°	88.9	90.3	90.3	91.7	90.3	90.3	90.3
4	170°-155°	100.0	100.0	100.0	100.0	99.5	99.5	99.5
4	155°-135°	97.8	97.7	98.2	99.1	99.1	99.5	99.5
4	135°-115°	96.4	99.0	98.7	98.4	99.3	99.3	99.3
4	115°-105°	99.4	100.0	99.4	100.0	100.0	99.4	99.4
4	105°-79°	99.8	99.8	99.8	99.8	99.8	99.8	99.8
4	76°-47°	96.3	95.4	96.6	96.1	97.5	97.5	97.5
4	47°-36°	98.5	99.5	100.0	100.0	100.0	100.0	100.0
4	34°-14°	93.7	93.7	94.0	93.5	94.9	96.6	95.7
4	14°-0°	88.2	89.7	88.5	92.4	92.0	94.3	94.3
4	0°-(-23.5°)	81.8	82.5	84.6	85.8	85.1	85.7	84.8